Niels Bohr Institute
UNIVERSITY OF COPENHAGEN

PhD thesis

Søren Frimann

Evolution of Deeply Embedded Protostars
Simulations meet Observations

EVOLUTION OF DEEPLY EMBEDDED PROTOSTARS

SIMULATIONS MEET OBSERVATIONS

SØREN FRIMANN

Dissertation submitted for the degree of

PHILOSOPHIÆ DOCTOR

Centre for Star and Planet Formation
Niels Bohr Institute & Natural History Museum of Denmark
Faculty of Science
University of Copenhagen

This thesis has been submitted to the PhD School of The Faculty of Science, University of Copenhagen

Title	Evolution of Deeply Embedded Protostars, Simulations meet Observations
Author	Søren Frimann
Date of Submission	4 January, 2016
Date of Defence	21 March, 2016
Department	Centre for Star and Planet Formation, Niels Bohr Institute & Natural History Museum of Denmark, Faculty of Science, University of Copenhagen
Academic Advisor	Assoc. Prof. Jes Kristian Jørgensen
Assessment Committee	Assoc. Prof. Marianne Vestergaard (chair)
	Prof. Dr. Cornelis P. Dullemond
	Prof. Dr. Stefanie Walch

Typeset using the Palatino and Euler type faces by Hermann Zapf
Layout and typography by the author with LaTeX 2_ε using the class "`classicthesis`" developed by André Miede
Cover: The Perseus molecular cloud at visible wavelengths. The star forming regions appear as the dark patches in this image. Photography by Lynn Hilborn. Printed with the permission of the photographer.

To my parents

ENGLISH ABSTRACT

Recent advances in both observations and numerical simulations of star-forming regions have opened up the possibility of coupling these two fields together. This thesis presents detailed radiative transfer models created from large-scale simulations of star-forming molecular clouds. The radiative transfer models are used to calculate synthetic observables, which are compared directly to a number of observational studies. The numerical simulations comprise the formation of several hundred protostars, meaning that, for the first time, such a comparison can be done in a statistical meaningful manner. The goal of this comparison is both to benchmark the simulations by testing if observational results can be reproduced, and to use the simulations to aid in the interpretation of the observations.

The research deals with the earliest stages of star formation – the protostellar phase – where the protostars are still embedded within massive dusty envelopes with sizes of order 0.1 pc[1]. We use spectral energy distributions of the protostars in the simulation to calculate evolutionary tracers, and find their distributions to match the observations well, save for some optical depth issues that can be traced back to the resolution of the simulation. We also study the distribution of protostellar luminosities in the simulation, and find that both the median and the dispersion match the observed distribution well. Both of these tests are important benchmarks of the simulation since they show that the overall evolution of the protostars in the simulation matches the observational results. We also study the occurrence of circumstellar disks in the same simulation and find that they are ubiquitous at all stages of the protostellar evolution.

A special emphasis is put on the study of protostellar accretion, which may have important physical consequences for the evolution of protostellar systems. The sublimation of CO-ice from dust grains in the surrounding envelope can be used to trace accretion variability in protostars, because the increased heating during an accretion burst will cause the CO-ice to sublimate into the gas-phase where the excess can be measured by telescopes. We recreate such observations from a numerical simulation, and find that it is indeed possible to trace accretion variability in such a manner, thereby confirming the approach taken by an observational study. The synthetic observations fail to reproduce the full spread of values seen in the real observations, which can be traced back to a lack of accretion variability in the simulation. This particular simulation does not include disk physics, and we attribute this lack of accretion variability to that effect.

1 approximately 3×10^{12} km

We also carry out an observational follow-up study, attempting to link evidence of accretion bursts together with evidence of circumstellar disks. The study targets 20 embedded protostars in the Perseus molecular cloud, and reveals plenty of evidence for variable accretion through observations of $C^{18}O$ (an optically thin isotopologue of CO). The study also reveals that low-luminosity protostars are more likely to have enhanced $C^{18}O$ emission, which is interpreted to mean that the low-luminosity protostars are between accretion bursts, while the high-luminosity objects are those that are currently undergoing accretion bursts.

DANSK RESUMÉ

Nylige fremskridt indenfor både observationer og numeriske simuleringer af stjernedannende områder har gjort det muligt at koble disse to felter sammen. Denne afhandling indeholder detaljerede strålingstransportmodeller beregnet ud fra storskala simuleringer af stjernedannende molekyleskyer. Strålingstransportmodellerne bruges til at beregne syntetiske observationer, som sammenlignes direkte med et antal observationelle studier. I de numeriske simuleringer dannes hundredevis af protostjerner, hvilket betyder at sammenligningerne med de observationelle studier kan foregå på et statistisk signifikant grundlag. Målet med sammenligningerne er både at sikre at simuleringerne er i stand til at reproducere observationelle resultater, og at bruge dem som støtte i fortolkningen af observationelle resultater.

Denne afhandling omhandler de tidligste stadier af stjernedannelsesprocessen – den protostellare fase – hvor protostjernerne stadig er omgivet af en tæt molekylesky med radier af størrelsesordenen $0.1\,\mathrm{pc}$[2]. Vi bruger kontinuumspektre af protostjernerne i simuleringen til at beregne indikatorer for protostjernernes udvikling, og finder at deres fordelinger stemmer overens med observationelle resultater, bortset fra nogle effekter af optisk tykkelse som kan spores tilbage til opløsningen af simuleringen. Vi studerer også protostjernernes luminositetsfordeling, og finder at både medianværdi og spredning af fordelingen stemmer overens med observationelle resultater. Begge disse er vigtige tests af simuleringen fordi de viser at den generelle udvikling af protostjernerne i simuleringen stemmer overens med hvad vi ved fra observationer. We studerer også forekomsten af skiver omkring protostjerner og finder at de forekommer i alle stadier af stjerneudviklingen.

Studiet har specielt fokus på protostjerners massetilvækst, som kan have stor betydning for den fysiske udvikling af protostjernesystemer. Fordampning af kulilteholdige iskapper på støvkorn i den omkringliggende sky kan bruges til at måle variationer i protostjernes massetilvækst idet en pludselig acceleration af massetilvæksten vil forøge opvarmingen af den omkringliggende sky og få kulilten (CO) til at fordampe fra støvkornene. Forøgelsen af CO gas kan måles med teleskoper på jorden og dermed bruges til at detektere variationer i massetilvæksten. Vi bruger en numerisk simulering til at beregne syntetiske observationer af CO og finder at det er muligt at måle udstrækningen af CO omkring sådanne protostjerner, og vi underbygger dermed de observationelle resultater. Vi finder imidlertid også, at de syntetiske observationer ikke er i stand til at reproducere den

2 omtrendt $3 \times 10^{12}\,\mathrm{km}$

fulde spredning af udstrækninger som ses i de rigtige observationer. Dette skyldes en mangel på variationer i massetilvæksten i simuleringen. Den numeriske simulering som bruges i studiet indholder ikke nogen protoplanetariske skiver, og manglen på variationer i massetilvæksten skyldes antageligt denne effekt.

Vi udfører også et observationelt opfølgningsprojekt, med formål at undersøge sammenhængen mellem variationer i massetilvæksten og forekomsten af protoplanetariske skiver. Studiet undersøger 20 protostjerner i molekyleskyen Perseus, og vi finder klar evidens for variationer i massetilvæksten ved hjælp af observationer af $C^{18}O$ (en optisk tynd isotopolog af CO). Studiet viser også at protostjerner med lav luminositet har større sandsynlighed for at have $C^{18}O$ fordelt over større udstrækning relativt til deres nuværende luminositet, end protostjerner med høj luminositet. Vores teori omkring dette resultat er at protostjerner med lav luminositet er objekter som befinder sig i en tilstand med lav massetilvækst, mens objekterne med høj luminositet har en forøget massetilvækst.

Appreciation is a wonderful thing.
It makes what is excellent in others belong to us as well.

— Voltaire

ACKNOWLEDGMENTS

I would like to express my gratitude towards my supervisor, Jes Jørgensen, for his guidance and, not least, his encouragement throughout my time as a PhD student. I am also grateful to Troels Haugbølle for granting me access the simulations of the computational astrophysics group and for teaching me how to work with them. My special thanks goes to Paolo Padoan, Mike Dunham, and Doug Johnstone for hosting me in Barcelona, in Cambridge, and in Victoria, and for the stimulating discussions I have shared with all three of them.

Centre for Star and Planet formation is a great place to work, and is full of good people. I am indebted to all the friends I have made there, particularly to my office mates and good friends, "the lovely ladies": Julie Maria Lykke, Bettina Livermore, Elishevah Van Kooten, Nikitha Susan, and Natassia Jensen; to the other members of the submm group: Johan Lindberg, Magnus Persson, Susanne Wampfler, Suzanne Bisschop, Christian Brinch, Audrey Coutens, Steffen Kjær Jacobsen, Per Bjerkeli, and Matthijs van der Wiel; to administrators Marianne Bentsen and Lene Bentzen; and to all the other members of Starplan.

I am grateful to my entire family for their love and unwavering support: Mum & Dad, Moster & Kurt, Mogens, Casper & Janne, Fie & Michael, Lise, Helene, Martin, Christian, and Alexander.

CONTENTS

LIST OF FIGURES

LIST OF TABLES

ACRONYMS

ALMA Atacama Large Millimeter Array

AMR Adaptive Mesh Refinement

c2d Cores to Disks

CTTS Classical T Tauri Star

FWHM Full Width at Half Maximum

GB Gould Belt survey

HOPS Herschel Orion Protostar Survey

IMF Initial Mass Function

IRAS Infrared Astronomical Satellite

ISM Interstellar medium

ISRF Interstellar Radiation Field

LLF Local Lax Friedrich

LTE Local Thermodynamic Equilibrium

MHD magnetohydrodynamics

MRI Magnetorotational Instability

PLF Protostellar Luminosity Function

PMS pre-main-sequence

SCUBA Submillimetre Common-User Bolometer Array

SED Spectral Energy Distribution

SMA Submillimeter Array

YSO Young Stellar Object

Part I

INTRODUCTION

1 SCIENTIFIC BACKGROUND

1.1 LOW-MASS STAR FORMATION

1.1.1 *From molecular clouds to star-forming cores*

Stars form predominantly in large molecular clouds in the Interstellar medium (ISM), consisting mostly of molecular hydrogen, H_2. Such clouds are characterised by their high densities, $\langle n_{\text{gas}} \rangle \gtrsim 10^2\,\text{cm}^{-3}$; low temperatures, $T \sim 10\,\text{K} - 20\,\text{K}$; and supersonic turbulent motions (Larson, 1981). Observations from the Herschel Space Observatory reveal that the spatial structures of molecular clouds are characterised by being highly filamentary (e.g. André et al. 2010; see André et al. 2014 for a recent review). Although it is still under debate exactly how such filaments form, evidence from numerical simulations reveal that turbulence induced converging flows are capable of naturally producing sheets and filaments similar to those seen in observations (e.g. Padoan et al. 2001).

The molecular cloud filaments are believed to fragment further into dense cores (Men'shchikov et al., 2010), which are the smallest components of the hierarchical structure that makes up molecular clouds. Such cores can be defined as gravitationally bound over-dense regions of the molecular cloud, and it is these cores that may, at some point, become gravitationally unstable and form a star. One typically distinguishes between pre- and protostellar cores depending on whether or not they have begun the process of collapsing to form a protostar. Surveys of dense cores in the nearby molecular clouds (e.g. Enoch et al. 2008; Jørgensen et al. 2008) reveal that the number of pre- and protostellar cores are roughly equal, indicating that the expected lifetime of prestellar cores is similar to the duration of the core-collapse phase of star formation.

1.1.2 *Protostellar collapse*

Dense cores become unstable and collapse if gravity is large enough to overcome the internal pressure of the core. One way to estimate if a dense core is going to collapse is to measure if its mass exceeds the "Jeans mass":

$$M_J = \left(\frac{\pi c_s^2}{G}\right)^{3/2} \rho^{-1/2},$$

where c_s is the sound speed, G the gravitational constant, and ρ the density of the cloud. The Jeans mass should only be taken as a rough estimate of the mass needed for core-collapse to proceed, since the analysis leading up to the result assumes an isothermal, initially uniform gas in equilibrium, which is not realisable in nature. Also the Jeans mass only includes thermal pressure to counteract gravity, ignoring both magnetic and turbulent pressures.

Following Shu (1977), who solved the self-similar collapse of a singular isothermal sphere in hydrostatic equilibrium, the core-collapse is expected to proceed in an inside-out fashion, with $\rho \propto r^{-3/2}$ in the collapsing inner region and $\rho \propto r^{-2}$ in the region that has not yet begun collapsing. The collapse is initially expected to be isothermal, however, as the density increases in the inner parts, the core becomes optically thick and the collapse becomes adiabatic. At some point the internal pressure, following the increase in temperature, becomes high enough to halt the collapse forming the "first hydrostatic core" (Larson, 1969). The temperature of the core rises steadily as mass continues to be added until, at temperatures of ~2000 K, H_2 dissociates and the first core becomes gravitationally unstable and resumes its collapse. Eventually a second dore, the protostar, is formed marking the transition between the pre- an protostellar evolutionary phases.

1.1.3 *Stages of star formation*

In the earliest stages of star formation, after the formation of the second core, the protostar is still deeply embedded within a dense collapsing envelope. Assuming a sound speed of $0.2\,\mathrm{km\,s^{-1}}$, appropriate for cold dense cores, the collapse model of Shu (1977) predicts a constant infall rate of material of $c_s^3/G \sim 2 \times 10^{-6}\,M_\odot\,\mathrm{yr}^{-1}$. Because of conservation of angular momentum, most of the envelope material will not initially end up on the protostar, instead accreting onto a circumstellar disk (Terebey et al. 1984; see Sect. 1.1.4 below for a discussion about circumstellar disks). For material to make its way through the disk and onto the protostar angular momentum has to be lost, which is thought to happen through the launching of ionised jets and molecular outflows. The exact mechanisms involved in launching these jets and outflows are still under debate, but it seems clear that they are intimately connected to the morphology of magnetic fields around young stars (Shu et al. 1994; see Frank et al. 2014 for a recent review).

As the protostellar envelope gets dispersed by jets and outflows, or accreted onto the disk/protostar, a Classical T Tauri Star (CTTS) is revealed, signalling the end of the protostellar stage. CTTSs retain a massive disk and are characterised by their bright Hα emission (Herbig, 1962) caused by accretion from the disk and onto the central object. The CTTS stage also hosts the so-called FU Orionis and EX Lupi

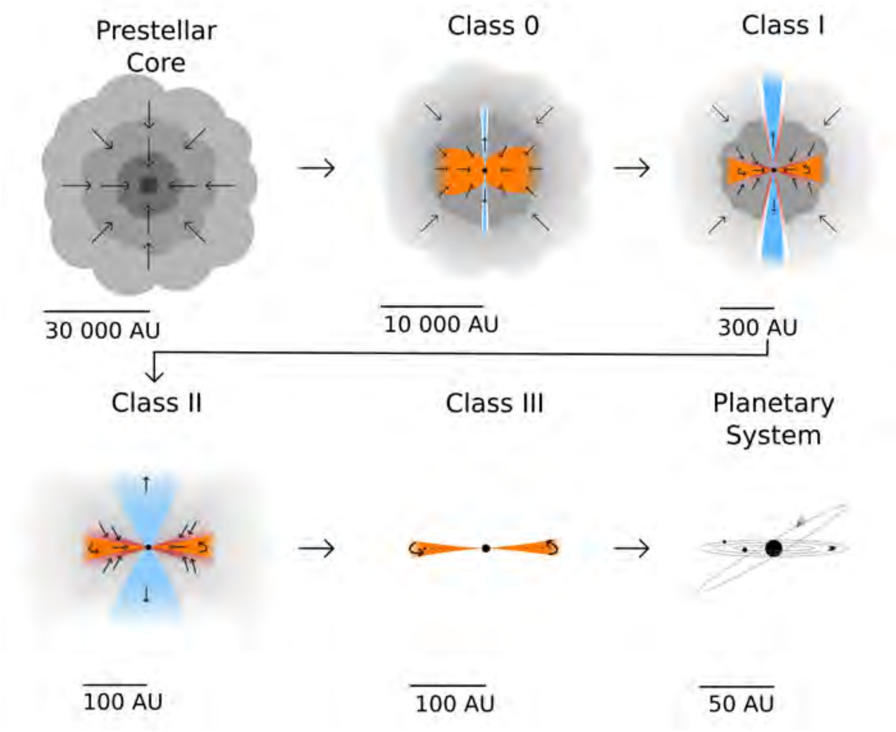

Figure 1.1: Stages of star formation and their relation to the observationally defined classes. From Persson (2013).

objects (also known as FUors and EXors) (Herbig, 1977, 1989), which are young stars showing large luminosity bursts, thought to be linked to episodic accretion events (see Sect. 1.2 for more discussion about accretion in young stars). The final stage of star formation, before the star starts fusing hydrogen in the core and settles on the main sequence, is the weak-line T Tauri stage. At this stage, accretion onto the central object is either very slow of has terminated completely as the disk is dispersing. The classical and weak-line T Tauri stars are also commonly referred to as pre-main-sequence (PMS) stars.

1.1.3.1 *Classification of young stars*

Lada & Wilking (1984) realised that Young Stellar Objects (YSOs) can be sorted into three observationally defined classes: I, II, and III based on the shape of their Spectral Energy Distribution (SED), with a fourth Class 0 being added by André et al. (1993). By linking to the physical stages of star formation discussed above, the observationally defined classes can be interpreted as an evolutionary sequence (Adams et al., 1987), where Class 0 and I objects correspond to the deeply embedded protostars, still surrounded by a massive infalling envelope, with Class 0 protostars being those objects where more than half the mass of the system still resides in the envelope (André et al., 1993). Class II systems correspond roughly to the CTTS stage, where the envelope has mostly dissipated leaving behind a PMS star encircled by

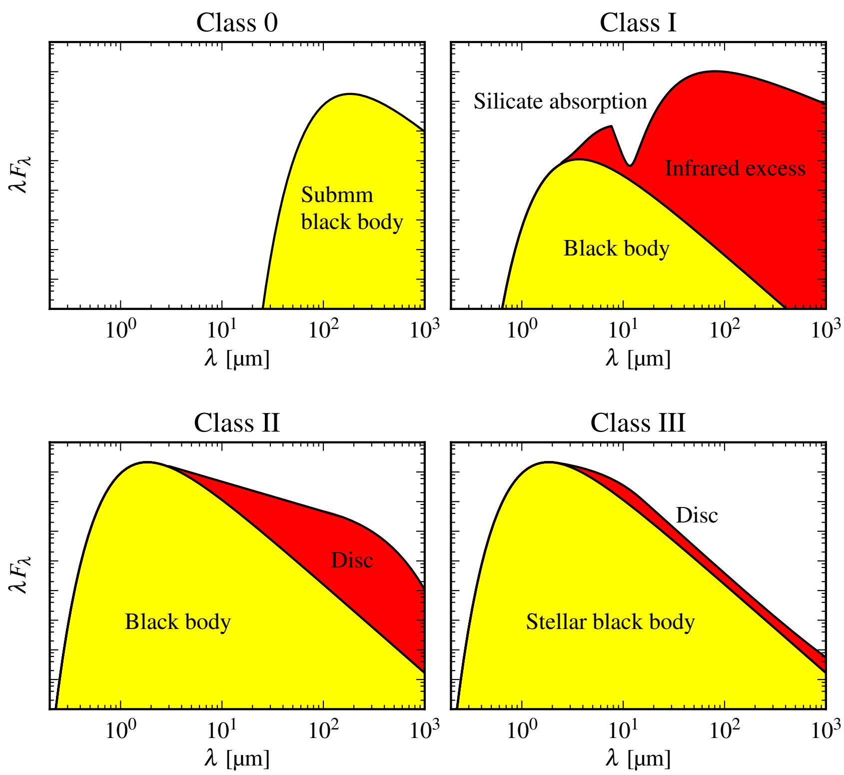

Figure 1.2: Schematic SEDs of the different observationally defined classes. The yellow portions denote black-body curves, and the red portions any excess to this black body. From Lindberg (2013).

a massive disk. Finally, Class III systems correspond roughly to the weak-line T Tauri stage with its dispersing disk. Figure 1.1 shows the different stages of star formation, and how they are thought to relate to the observationally defined classes, while Figure 1.2 shows schematic SEDs of the observationally defined classes.

Three tracers of protostellar class, all calculated from the SED, have been defined. The original tracer is the spectral index, α, defined as

$$\alpha = \frac{d \log \lambda S_\lambda}{d \log \lambda},$$

where S_λ is the SED and α is calculated between 2.2 μm to 20 μm. André et al. (1993) introduced the ratio between submm luminosity and bolometric luminosity as a tracer of the most deeply embedded objects, that are not normally detected between 2.2 μm and 20 μm

$$\frac{L_{smm}}{L_{bol}} = \frac{\int_0^{c/350\,\mu m} S_\nu \, d\nu}{\int_0^\infty S_\nu \, d\nu},$$

where the submm luminosity, L_{smm}, is measured onwards of 350 μm. Finally, Myers & Ladd (1993) introduced the "bolometric temperature" – a protostellar equivalent to the effective temperature – which

Table 1.1: Definition of class boundaries following Lada (1987), André et al. (1993), and Chen et al. (1995). Note, that there is no boundary defined between Classes 0/I for α, and Classes I/II and II/III for L_{smm}/L_{bol}.

	α	L_{smm}/L_{bol}	T_{bol}
Class 0	...	$\geqslant 0.5\,\%$	$< 70\,\mathrm{K}$
Class I	$\geqslant 0$	$< 0.5\,\%$	$70\,\mathrm{K} \leqslant T_{bol} < 650\,\mathrm{K}$
Class II	$-2 \lesssim \alpha \leqslant 0$	...	$650\,\mathrm{K} \leqslant T_{bol} < 2800\,\mathrm{K}$
Class III	$-3 < \alpha \lesssim -2$	...	$\geqslant 2800\,\mathrm{K}$

is the temperature of a black body with the same mean frequency as the SED

$$T_{bol} = 1.25 \times 10^{-11} \frac{\int_0^\infty \nu S_\nu \, d\nu}{\int_0^\infty S_\nu \, d\nu} \, \mathrm{K}.$$

Similar to L_{smm}/L_{bol} the bolometric temperature is best at distinguishing the embedded Class 0 and I objects (Evans et al., 2009), but functions as a tracer all the way up to the end of the PMS stage, where it becomes identical to the effective temperature. Table 1.1 lists class definitions for the different tracers.

The advantage of the observationally defined classes is that they provide an objective way of distinguishing between the evolutionary stages of YSOs. The different tracers are not always in agreement with each other (e.g. Evans et al. 2009; Dunham et al. 2014), and are generally subjects to different observational uncertainties, such as projection and luminosity effects, which means that they are not always in agreement with the physical stage they seek to trace. Still, the observational classifications provide the main framework for discussing the evolution of YSOs – e.g. the rate with which they evolve from the deeply embedded to the PMS stages. Assuming a Class II lifetime of 2 Myr (Spezzi et al., 2008), Evans et al. (2009) used the relative numbers between the different classes to estimate the length of the embedded Class 0+I phase to ~0.5 Myr.

1.1.4 *Circumstellar disks*

Understanding the formation of circumstellar disks is a central question of star formation – they are, after all, the birthplace of planets such as our own – but they are also important to other aspects of the evolution of YSOs, for example as mediators of accretion onto the central object. Disks are ubiquitous around young stars, as evidenced by the excess of infrared emission measured towards YSOs in young clusters (Hernandez et al., 2007), or by the discovery of more than 1000 planetary systems (http://www.exoplanet.eu), which indicates

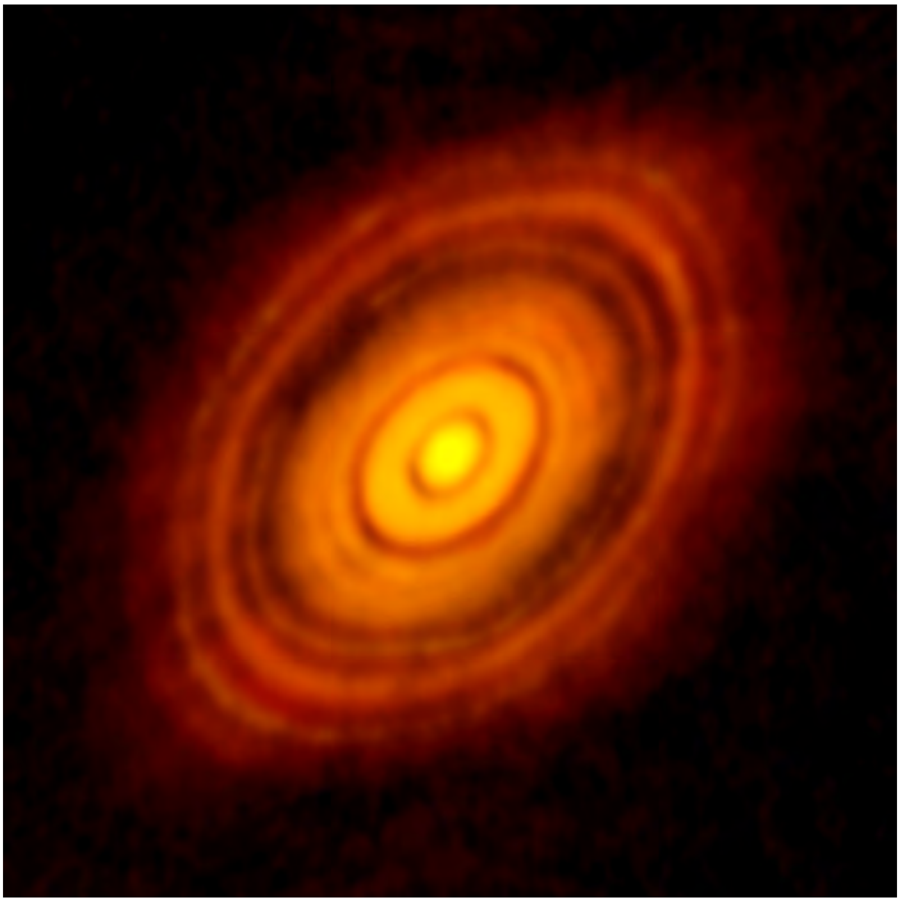

Figure 1.3: 1.3 mm continuum image of HL Tau observed with ALMA. The diameter of the disk is ≈ 235 AU and the smallest resolved scales are ≈ 5 AU. Credit: ALMA, ALMA Partnership et al. (2015).

that most, if not all, Sun-like stars must, at some point, have been encircled by a disk. Figure 1.3 shows the, by now, famous 1.3 mm continuum image of the young disk HL Tau, observed by the Atacama Large Millimeter Array (ALMA) (ALMA Partnership et al., 2015). The image shows a number of gaps in the disk, interpreted as being possible sites of planet formation. This is very interesting, not only because this is the first time such gaps have been imaged, but also because of the young age of of HL Tau ($\lesssim 1$ Myr), which suggests that planet formation may commence earlier than previously thought.

Theoretically, and in the absence of magnetic fields, the formation of a circumstellar disk is a natural consequence of conservation of angular momentum during the core-collapse phase (Terebey et al., 1984), as even a small initial rotation of the dense core, translates into high rotational velocities at the small scales relevant to protostellar systems. With the presence of magnetic fields the situation gets more complicated. An ionized fluid undergoing a rotating collapse, with a magnetic field running parallel to the rotation axis, will experience magnetic breaking, as the magnetic field lines get wrought up and magnetic forces exert a torque on the infalling material, which is effective at transporting angular momentum outwards. This "magnetic breaking catastrophe" (Galli et al., 2006) is very effective and may completely suppress the formation of rotationally supported disks for magnetic field strengths typical of dense cores (Allen et al., 2003).

The theoretical prediction that the formation of rotationally supported disks is suppressed in magnetised cores is clearly at odds with observations, which show that disks are common around young stars. Several mechanisms for solving this problem have been investigated, including non-ideal magnetohydrodynamics (MHD) effects (e.g. Armitage 2011), misalignment between rotation and magnetic field axes (e.g. Joos et al. 2012), and turbulence which may distort the magnetic field and hamper its ability to transport angular momentum outward (e.g. Seifried et al. 2012, 2013). The latter effect especially seems to be an effective way of overcoming the magnetic breaking catastrophe.

Although it is well-established that circumstellar disks are very common around young stars, there is still some uncertainty as to how early they form. This is connected to the fact that long-wavelength observations of both high resolution and high sensitivity are needed to detect disks around the deeply embedded Class 0 and I protostars; something that has only become possible with the advent of large submm interferometers such as the Submillimeter Array (SMA) and ALMA.

Interferometric continuum surveys of embedded protostars generally reveal the presence of compact emission around the protostars, that cannot be reproduced by models of envelope emission, and are therefore interpreted as being disks (e.g. Looney et al. 2000; Harvey et al. 2003; Jørgensen et al. 2005a, 2009; Enoch et al. 2011). Although this is a powerful tool for getting data from several objects, thereby being able to address how common early disks are in a statistical sense, the weakness of this method is that it provides no information about the kinematics of the disks, so there is no way to address if the compact object is, in fact, a rotationally supported disk. For example, Chiang et al. (2008) using the theoretical collapse model of Tassis & Mouschovias (2005) showed that a disk is not necessary for reproducing compact emission similar to that seen in the observational studies. Also, collapse models of magnetised cores predict the formation of magnetically supported pseudodisks (Galli & Shu, 1993a,b), which come about as magnetic pinching forces deflect the infalling material towards the midplane.

Molecular line observations are necessary to gain access to kinematic information that can reveal whether the rotation profile of a disk candidate is consistent with Keplerian rotation ($v_\phi \propto r^{-0.5}$) or infall under conservation of specific angular momentum ($v_\phi \propto r^{-1}$; Belloche 2013). The situation is complicated by the fact that many moleculare species become optically thick in the innermost parts of the deeply embedded protostellar systems. Even so, Keplerian rotation has been detected towards a number of Class I sources (e.g. Brinch et al. 2007b; Lommen et al. 2008; Harsono et al. 2014), and even towards a few Class 0 sources (Tobin et al., 2012; Murillo & Lai, 2013; Lindberg et al., 2014). Although there is still much work to be done, the evidence points towards disk formation occurring very early on in the evolution of protostellar systems.

1.2 ACCRETION OF YOUNG STELLAR OBJECTS

Understanding how YSOs gain their mass is a central question of star formation with ties to a diverse range of phenomena such as the origin of the Initial Mass Function (IMF), the formation and evolution of circumstellar disks, and the mass ejection in jets and outflows. It is clear from the discussion in Sect. 1.1.4 above that, because of conservation of angular momentum, the evolution of accretion rates and the evolution of circumstellar disks must be intimately connected. Accretion is thought to proceed in a fashion where infalling material is first accreted onto the disk from where it will eventually make its way onto the central object after getting rid of its excess angular momentum. Disk material can lose its angular momentum through the launching of jets and winds (Blandford & Payne, 1982), through magnetic braking, or through viscous accretion (Pringle, 1981), which is capable of moving material inwards while moving angular momentum outwards. Physical sources of this viscosity include gravitational and Magnetorotational Instabilities (MRIs) (e.g. Armitage 2011).

It is difficult to unambiguously infer the accretion rates toward young stars. In PMS stars, that have lost their envelope and are therefore visible at short wavelengths, accretion rates are often traced by the strength of the Hα emission line at 6563 Å. Values inferred with this method indicate that the accretion rates of PMS stars form a broad distribution spanning from $10^{-11}\,M_\odot\,yr^{-1}$ to $10^{-7}\,M_\odot\,yr^{-1}$ with a mean of $\sim 1.4 \times 10^{-9}\,M_\odot\,yr^{-1}$ (Manara et al., 2012). Coupling to models of stellar evolution indicate that accretion rates tend to decrease with age (Hartmann et al., 1998) and increase with stellar mass (Muzerolle et al., 2003). While the negative age correlation can be easily explained by the gradual dissipation of the disk the physical basis for the positive mass correlation is more elusive.

In two studies of time-dependent accretion variabilities Costigan et al. (2012, 2014) found accretion rates in PMS stars to be roughly constant over both very short (hours) and very long time-scales (years). The authors found that over time-scales of days accretion rates could change by a factor of ~2, which they interpreted as being due to asymmetric accretion flows that are modulated by the rotation of the central object. Despite the relative constancy of accretion rates inferred for PMS stars, this stage also hosts the FUor and EXor objects that un-

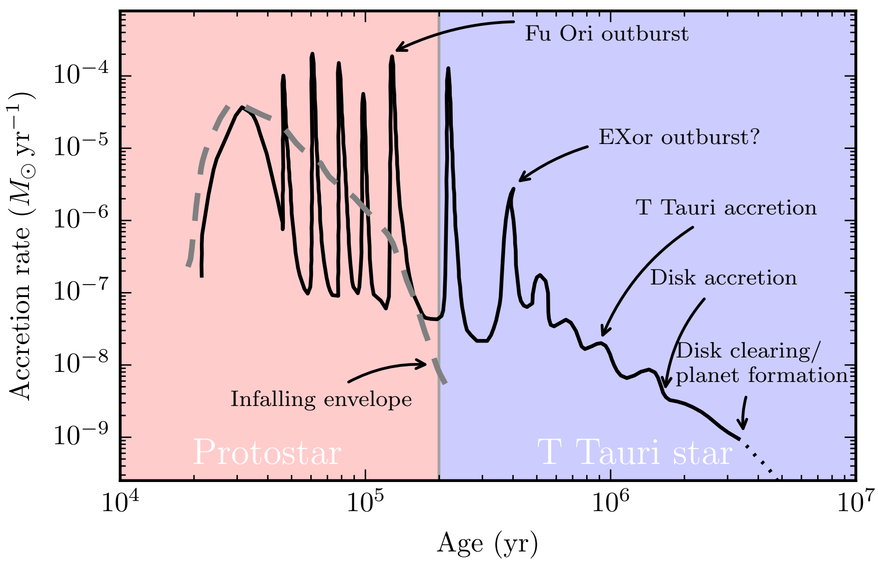

Figure 1.4: Schematic outline of the evolution of accretion rates throughout the star formation phase. Based on Hartmann (2008).

dergo high amplitude luminosity bursts thought to trace variations of the underlying accretion rates. EXor objects are characterised by showing repetitive outbursts of small amplitude and short duration relative to the FUor objects (Herbig, 1989). Originally, the EXor objects were thought to represent bursts in older more evolved systems relative to the FUor objects. The discovery of several new bursting PMS stars in recent years have muddled the picture quite a bit and cast doubt on whether the distinction between FUor and EXor type objects is even a meaningful one (Audard et al., 2014). Both types of outbursts are still, however, recognised as originating from accretion variabilities. Figure 1.4 shows, schematically, how the accretion rates of YSOs are thought to evolve with time.

1.2.1 *Protostellar accretion*

For embedded objects accretion rates can be inferred by measuring the luminosity of the protostar, which can be written as the sum of two components

$$L_{tot} = L_{phot} + L_{acc} = L_{phot} + f_{acc}\frac{Gm\dot{m}}{r}.$$

Here L_{phot} is the luminosity arising from processes that are intrinsic to the protostar, such as gravitational contraction and deuterium burning, while L_{acc} is the luminosity arising from accretion onto the protostar. For deeply embedded objects it is often assumed that L_{acc} dominates over L_{phot} so that $L_{tot} \sim L_{acc}$ (e.g. Dunham et al. 2010). m and r are the mass and radius of the protostar while $\dot{m}$ is the instantaneous accretion rate onto the protostar. f_{acc} is the fraction of the gravitational energy that is radiated away. Assuming $f_{acc} = 1$, a protostellar mass and radius of $0.5\,M_\odot$ and $2.5\,R_\odot$, and an accretion rate of $2 \times 10^{-6}\,M_\odot\,yr^{-1}$ (as predicted by the Shu 1977 collapse model), this implies an accretion luminosity of $\sim 10\,L_\odot$.

With the launch of the Infrared Astronomical Satellite (IRAS) in 1983 it became possible to identify and measure accurate bolometric luminosities of embedded protostars for the first time. Kenyon et al. (1990) surveyed 17 embedded protostars in the Taurus-Auriga star-forming region and found an average velocity of $\sim 1\,L_\odot$, in clear disagreement with the $\sim 10\,L_\odot$ expected from simple physical arguments. Following the launch of the Spitzer Space Telescope and the Herschel Space Observatory, with their high sensitivities and ability of carrying out observations at even longer wavelengths, many more embedded protostars have been detected in the nearby star-forming regions and we now know that the distribution of protostellar luminosities (the Protostellar Luminosity Function; PLF) is a broad distribution, spanning more than three orders of magnitude, with a median luminosity of $1\,L_\odot$–$2\,L_\odot$ (e.g. Evans et al. 2009; Kryukova et al. 2012; Dunham et al. 2013).

The inability of simple physical arguments to accurately predict the observed luminosity distribution is known as the "luminosity problem" and was first discussed by Kenyon et al. (1990). Any solution to the luminosity problem has to be able to explain, not only the median of the PLF, but also the large spread. Furthermore, given that stars obtain most of their mass in the embedded stage, which is estimated to take $\sim 0.5\,Myr$ (Evans et al., 2009), an average accretion rate of $2 \times 10^{-6}\,M_\odot\,yr^{-1}$ is still needed to assemble a one solar mass star. These constraints suggest a solution to the luminosity problem involving non-uniform accretion rates that are characterised by a smooth decline from early to late stages, by short intermittent bursts of high accretion (episodic accretion, see Sect. 1.2.2), or by a combination of the two.

The finding that accretion needs to be non-steady to explain the observations is not altogether surprising. The collapse of a Bonnor-Ebert sphere, which is non-singular isothermal core in hydrostatic equilibrium, for example, naturally produces a high initial infall rate, which declines over time (Foster & Chevalier, 1993). Similarly, Padoan et al. (2014), using a large MHD simulation of a molecular cloud, found that a gradual decline in the average large-scale infall rate is capable of reproducing both the IMF and the PLF. This finding is supported by multiple other numerical simulations that also find an overall decline in accretion rates with time (e.g. Offner et al. 2009; Dunham & Vorobyov 2012), as well as purely analytical studies such as Offner & McKee (2011), who found that several theoretical accretion models with smoothly varying accretion rates were able to reproduce the observed PLF

1.2.2 *Episodic accretion*

While it does not appear that episodic accretion needs to be invoked to reproduce the PLF, it is still a viable solution to the luminosity problem (e.g. Dunham et al. 2010; Offner & McKee 2011; Dunham & Vorobyov 2012), probably coupled with an overall decrease in the large-scale infall rate from early to late stages. Observationally, the evidence for episodic accretion events originate from the FU Orionis objects (Herbig 1966, 1977; see Audard et al. 2014 for a recent review), that are young stars observed to undergo high-amplitude long-lived luminosity bursts at optical wavelengths interpreted as being due to increased accretion. FU Orionis objects, or FUors, are likely slightly embedded objects, spanning the Class I/II divide, encircled by massive disks that facilitate the large accretion bursts. Theoretically, this is expected to happen if material is allowed to pile up in the disk before being released onto the star through some accretion instability. Several candidate mechanisms for driving the accretion bursts have been investigated including both MRI and gravitational instabilities (Vorobyov & Basu, 2005; Zhu et al., 2009), that are also suspected of being responsible for driving the overall accretion through the disk, and thermal instabilities (Bell & Lin, 1994). While it is not clear exactly how these mechanisms operate or what the relative importance is between them it is clearly important that mass is allowed to build up in the disk over some period of time, or the large accretion outbursts become difficult to explain. Indeed, the accretion evolution in the gradually decreasing accretion scenario discussed in the previous section is largely controlled by the evolution of the cores, while the episodic accretion paradigm discussed here is controlled by the evolution of the disks. Any discussion about episodic accretion therefore also automatically becomes a question of whether the accretion rates are primarily regulated by the cores or by the disks.

Deeply embedded objects are not visible at shorter wavelengths making it difficult to ascertain whether, and to what degree, they are subject to the same type of episodic outbursts as their more evolved counterparts. This difficulty is both connected to the smaller number of known deeply embedded objects, and the fact that space based telescopes are needed to perform surveys at the mid-infrared wavelengths where such embedded bursts are predicted to have their peak flux (Johnstone et al., 2013). To date, the only deeply embedded protostar that has been observed to undergo a direct and abrupt change in luminosity is the Class 0 protostar, HOPS 383, which was observed to increase its 24 µm flux by a factor of 35 between 2004 and 2008 (Safron et al., 2015).

Because the direct detection of deeply embedded bursts is very challenging, an alternative approach is to look for evidence of past accretion bursts in these objects. Two methods for doing this deserve

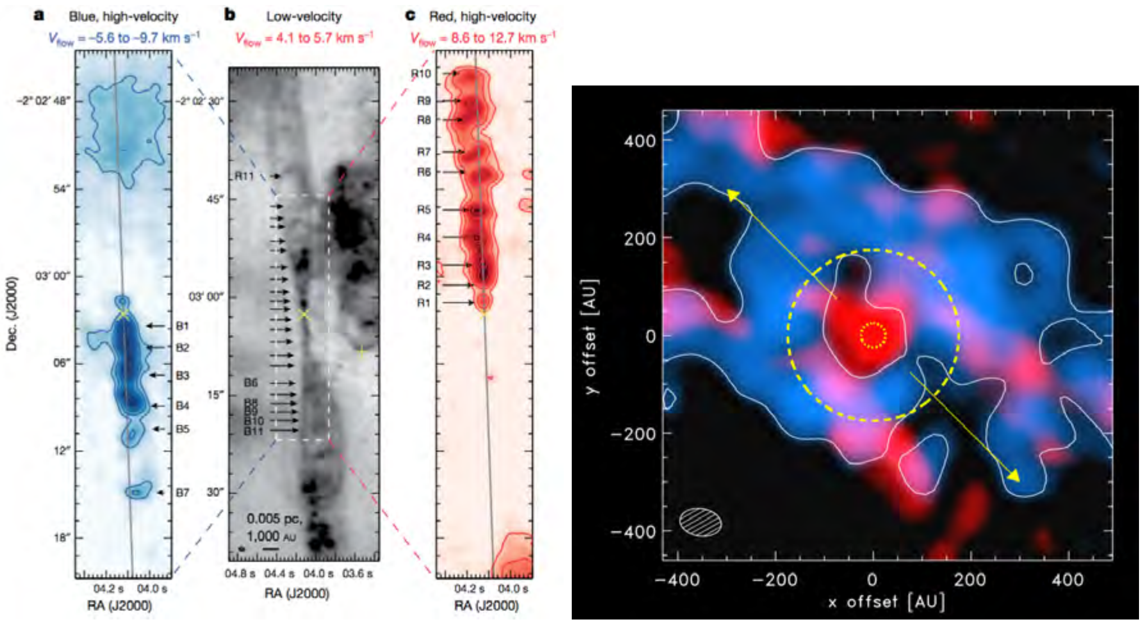

Figure 1.5: Left: Outflow knots observed towards the Class 0 source CARMA 7. From Plunkett et al. (2015). Right: Observed emission of CH_3OH (red) and $H^{13}CO^+$ (blue). $H^{13}CO^+$ is depleted towards the middle. From Jørgensen et al. (2013).

special attention, namely the detection of clumpy outflows and chemical tracers. The mass ejection in molecular jets and outflows is expected to be proportional to the mass accretion rate (Shu et al., 1994), meaning that the detection of "knots" or "bullets" in the outflows of YSOs can be used to determine if the accretion has been higher in the past (e.g. Arce et al. 2013). A recent example of this is Plunkett et al. (2015) who used ALMA observations of $^{12}CO\, J = 2-1$ to detect clumpy outflows in the Class 0 source CARMA-7 (see Figure 1.5). The distance between the knots in CARMA-7 correspond to a length of the quiescent periods in-between the bursts, which is of the order of few hundred years, although there is some uncertainty about this due to the inclination of the system not being known.

Chemistry can be used to trace past accretion events in situations where the chemistry in the disk and envelope of a system is brought into an out-of-equilibrium situation by an accretion burst, in such a way that it takes a while for the system to find its way back to an equilibrium. As long as this out-of-equilibrium situation pertains it can be used to trace the physical conditions during the event (e.g. Visser & Bergin 2012; Visser et al. 2015; Vorobyov et al. 2013). One of the best examples of this is the case of the low-mass protostar IRAS 15398–3359, which was observed by Jørgensen et al. (2013) to have HCO^+ distributed in a ring like structure around it (see Figure 1.5). The authors concluded that the best explanation for the lack of HCO^+ towards the centre is for it to have been destroyed by water, except that the temperatures in the region where HCO^+ is missing are so low that all the water is expected to be frozen-out on dust grains. An accretion burst within the past 100 yr to 1000 yr could have raised the temperatures sufficiently to bring water into the gas-phase from where it would then still be in the process of refreezing. Observations of CO_2 ice bands can also help in determining whether a star has undergone substantial changes to its luminosity in the past. In particular, the presence of pure CO_2 ices is a good indicator of significant thermal processing (e.g. Visser & Bergin 2012; Kim et al. 2012; Poteet et al. 2013).

2 METHODS

2.1 OBSERVATIONAL TECHNIQUES

Astronomers get their knowledge about the universe by measuring, as accurately as possible, the small fraction of light that makes its way from the distant stars and galaxies and down to Earth. For this reason observational astronomy can be viewed as an everlasting quest for improving our measurements in terms of sensitivity, spatial resolution and spectral coverage. Due to reprocessing by the dusty envelopes surrounding young stars and because of the low temperatures of molecular clouds star formation is most readily studied at wavelengths longer than ≈10 μm. This poses various observational challenges since, between roughly 10 μm and 0.5 mm Earth's atmosphere is mostly opaque (see Figure 2.1), meaning that observations at these wavelengths have to be carried out from space. The first infrared space telescope to be launched was IRAS in 1983 (Neugebauer et al., 1984), which surveyed the sky at four wavelengths between 12 μm and 100 μm. IRAS was followed by the Infrared Space Observatory (Kessler et al., 1996), which was launched in 1995 and covered wavelengths from 2.5 μm to 240 μm; by the Spitzer Space Telescope (Werner et al., 2004), which was launched in 2003 and covered wavelengths from 3 μm to 160 μm; and finally by the Herschel Space Observatory (Pilbratt et al., 2010), which was launched in 2009 and covered wavelengths from 55 μm to 671 μm. At wavelengths approaching 1 mm the atmosphere becomes transparent and observations can again be carried out from Earth. The transmission of the atmosphere at submm and mm wavelengths is highly dependent on the column density of water in the atmosphere above the telescope, meaning that dry sites at high altitudes are preferred when building new telescopes.

Another challenge when observing at long wavelengths lies in the spatial resolution. The highest achievable resolution of any optical system is determined by the diffraction limit, which can be written as

$$\theta = k\frac{\lambda}{D}\,\text{radian} \approx k\,2\times10^{5}\frac{\lambda}{D}\,\text{arcsec}, \tag{2.1}$$

where λ is the observing wavelength, D is the telescope diameter, and k is a constant of order unity that depends on the exact shape and illumination of the telescope aperture. For an uniformly illuminated circular disk (an Airy disk), which is a good model for most telescopes, $k \approx 1.06$ if the resolution is measured as the Full Width at Half Maximum (FWHM) of the diffraction pattern. The diffraction limit of a

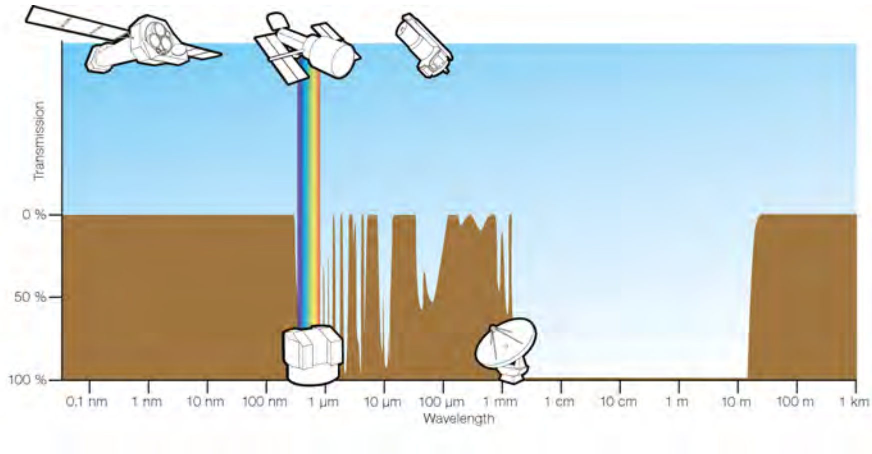

Figure 2.1: Sketch of atmospheric transmission as a function of wavelength. The atmosphere is transparent at optical and radio wavelengths, and otherwise mostly opaque. At wavelengths $\gtrsim 0.5\,\mathrm{mm}$ the atmosphere slowly begins to become transparent. Generally, the transmission of the atmosphere at submm and mm wavelengths depends heavily on the column density of water vapour in the air. Image Credit: ESA/Hubble (F. Granato).

$2.5\,\mathrm{m}$ telescope observing at $550\,\mathrm{nm}$ is $\approx 0.05''$, which is much lower than what is typically realisable in practice. This is primarily because of turbulence in the atmosphere, which means that resolutions $\lesssim 0.5''$ are typically unachievable without the use of adaptive optics. The diameters of optical telescopes are therefore primarily driven by a desire to collect more photons, rather than a desire to improve the theoretical resolution. At longer wavelengths the situation is very different; for a $2.5\,\mathrm{m}$ telescope observing at $1\,\mathrm{mm}$ the diffraction limit is $\approx 1'28''$. With a diameter of $100\,\mathrm{m}$, the largest fully steerable single-dish radio telescope in the world is the Green Bank Telescope, which translates into a resolution of $5.6''$ at a wavelength of $2.6\,\mathrm{mm}$ (the smallest wavelength that this telescope operates at). Structural limitations prohibit the construction of steer-able dishes much larger than $100\,\mathrm{m}$, and other techniques therefore have to be employed to increase the spatial resolution.

2.1.1 *Interferometry*

The spatial resolution of submm and mm observations can be increased by building an array of telescopes that work together as an interferometer. The maximum spatial resolution of an interferometer is inversely proportional, not to the diameter of the individual telescopes, but to the maximum distance between them.

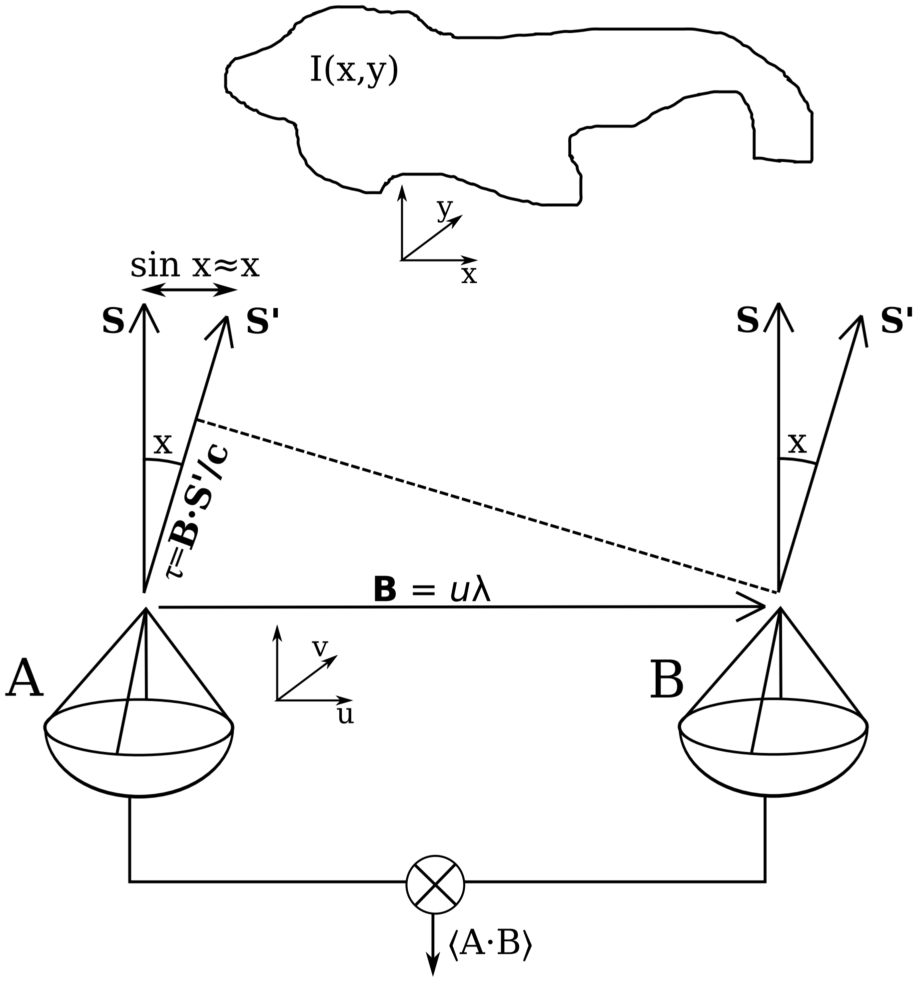

Figure 2.2: The two-element interferometer.

2.1.1.1 *The two-element interferometer*

Real submm and mm interferometers are typically made up of ~10 or more individual telescopes, but the conceptual workings of any interferometer can be understood in terms of the two-element interferometer, which is introduced here here. Figure 2.2 shows two single-dish telescopes, A and B, that are pointing towards the same point in the sky (the phase centre), defined by the pointing unit vector, **S**. The telescopes are separated by a projected baseline vector, **B**, as seen from the phase centre. Let us assume that the telescopes measure an electromagnetic plane wave coming from a point in the sky with co-ordinates (x, y) measured relative to the phase centre, and described by the new pointing unit vector, $\mathbf{S}'$. The offset from the phase centre is assumed to be small enough that the celestial sphere can be approximated by a plane, so that we do not have to concern ourselves with a third "depth" coordinate. The signals received by each telescope can be written down as

$$E_A(x,y,t) = A(x,y)\ e^{-2\pi i \nu (t-\tau)}$$
$$E_B(x,y,t) = A(x,y)\ e^{-2\pi i \nu t},$$

where $A(x,y)$ is the amplitude of the signal originating from (x,y), ν is the frequency of the incoming radiation and the time delay, $\tau = \mathbf{B}\cdot\mathbf{S}'/c$, is due to the signal taking slightly longer to reach telescope A. The signal measured by each telescope is mixed to calculate the time averaged cross-correlation

$$\begin{aligned}\langle E_A(x,y,t)\, E_B^\star(x,y,t)\rangle &= \langle A(x,y)\, A^\star(x,y)\rangle\ e^{-2\pi i \nu (t-\tau)}\ e^{2\pi i \nu t} \\ &= I(x,y)\ e^{2\pi i \nu \mathbf{B}\cdot\mathbf{S}'/c},\end{aligned} \tag{2.2}$$

where, in the last step, we have inserted $\mathbf{B}\cdot\mathbf{S}'/c$ in place of τ and used that the measured intensity of the source is simply the cross-correlation of its electric field with itself. If u is the number of wavelengths that fit between the telescopes along the baseline axis that runs parallel to x, and ν is the number of wavelengths that fit between the telescopes along the baseline axis that runs parallel to y, then $\mathbf{B}\cdot\mathbf{S}' = \lambda\,(ux + \nu y)$. Inserting this into Eq. (2.2) and integrating over the entire field of view takes us to the final result:

$$V(u,\nu) = \int PB(x,y)\ I(x,y)\ e^{2\pi i (ux+\nu y)}\, d\Omega, \tag{2.3}$$

where we have used that, for an electromagnetic wave, $\nu\lambda = c$. Eq. (2.3) is known as the van Cittert-Zernike theorem (van Cittert, 1934; Zernike, 1938), which relates the intensity distribution of the source on the sky, $I(x,y)$, to the visibility function, $V(u,\nu)$, which is a function of the projected baselines between pairs of telescopes. The quantity that is measured by an interferometer is therefore $V(u,\nu)$ and not the intensity distribution itself. $PB(x,y)$ is the primary beam of the interferometer which reflects the fact the telescopes are mostly sensitive to radiation coming from the pointing direction. Typically, the primary beam can be approximated by a Gaussian with a FWHM of λ/D where D is the diameter of the individual telescopes in the array.

The derivation of the van Cittert-Zernike theorem hinges on a few assumptions that it is important to be aware of. Most importantly, the observed source is assumed to be incoherent. Otherwise, cross-terms of the form $\left\langle E_A(x_1,y_1,t)\, E_B^\star(x_2,y_2,t)\right\rangle$ would have had to be included in the cross-correlation, when integrating over the field of view in the step leading up to Eq. (2.3). If the source is incoherent these cross-terms average to zero. It is also assumed that the source is far enough away relative to the size of the interferometer that all telescopes point in exactly the same direction, and that they measure the same plane-wave from the source. Finally, the angular extent of the source on the sky has to be small enough that the celestial sphere can be regarded as a plane or a third vector component has to be added to $\mathbf{B}$ and $\mathbf{S}'$. Typically, all these assumptions are satisfied for astronomical observations.

2.1.1.2 *Aperture synthesis*

The visibility function in Eq. (2.3) is seen to be the Fourier transform of the intensity distribution multiplied by the primary beam. In the limit where $V(u,v)$ is known exactly, inferring $I(x,y)$ is a simple question of calculating the inverse Fourier transform of $V(u,v)$. In practise, $V(u,v)$ is never fully sampled as each pair of telescopes contribute just one point to the (u,v)-plane (strictly speaking two points but as $I(x,y)$ is a real function its Fourier transform will be conjugate symmetric and the second point is superfluous). Even though the sampling can be improved by a large number of individual telescopes in the array, or by long time-series, interferometers will always lack very small baselines, corresponding to large scale emission on the sky, since no two telescopes can be spaced closer than the diameter of a dish.

The measurements of $V(u,v)$ can be represented by a sampling function $V'(u,v)$ consisting of delta-dirac functions at the baselines of the interferometer. Invoking the convolution theorem we see that

$$\begin{aligned}\mathcal{F}^{-1}\left[V'(u,v)\times V(u,v)\right] &= \mathcal{F}^{-1}\left[V'(u,v)\right] * \mathcal{F}^{-1}\left[V(u,v)\right] \\ &= B(x,y) * I(x,y),\end{aligned}$$

where $\mathcal{F}^{-1}\left[V'(u,v)\right] = B(x,y)$ is called the "dirty beam", and represents the response of a point source given the sampling of the (u,v)-plane. One typically wants to sample the (u,v)-plane well enough that the dirty beam resembles a centrally peaked Gaussian, but even then it will typically contain considerable side bands. To secure a good (u,v)-coverage an array consisting of several telescopes at various distances from one another has to be used. The total number of baselines in an array is given by $N\left(N-1\right)/2$, where N is the number of telescopes. As Earth rotates the position of the source on the sky changes, meaning that the projected baselines in the array change as well. Using the the rotation of Earth to improve the (u,v)-coverage is a central design component of most interferometers.

$\mathcal{F}^{-1}\left[V'(u,v)\times V(u,v)\right]$ is called the "dirty image" and is the convolution of $I(x,y)$ by the dirty beam. To get a better representation of $I(x,y)$ one wishes to interpolate $V(u,v)$ to get estimate the missing baselines, a process that is often also referred to a deconvolution. The algorithm most widely used for deconvolution is known as the `CLEAN` algorithm (Högbom, 1974), and works by subtracting point sources from the dirty image. The indirect assumptions made about the source for this algorithm to work is therefore that it can be decomposed into point sources, and that $V(u,v)$ is relatively smooth.

Figure 2.3: The submillimter Array. Image credit: Afshin Darian.

Employing the `CLEAN` algorithm also requires a good (u, v)-coverage for the method to converge to a good solution.

2.1.1.3 *The Submillimeter Array*

The Submillimeter Array (Ho et al. 2004; see Figure 2.3) is a submm and mm interferometer situated on Mauna Kea, Hawaii, at an altitude of 4080 m above sea level. The array operates between frequencies of 180 GHz and 700 GHz (1.7 mm and 0.5 mm) and consists of eight 6 m telescopes, that can moved around between different configurations providing baselines in the range of 9 m to 500 m. Chapter 6 discusses observations taken with the SMA

2.2 RADIATIVE TRANSFER

It is not possible for astronomers to bring the subjects of their research into a laboratory for experimentation. Instead, they rely solely on measuring the tiny fraction of light that make its way from the source through the vast nothingness of space only to be intercepted by one the various telescopes that have been built on Earth for exactly that purpose. Having spent large amount of money on building the telescopes that gather the light, most funding agencies consider it to be of central importance that scientists make an effort of interpreting measured radiation. This is where the concept of radiative transfer become useful as one can construct a physical model of an astronomical object and use radiative transfer methods to predict how that object would appear when observed with a telescope. This section introduces some of the basic concepts of radiative transfer. The material is based largely on the introductions given to the subject by Rybicki & Lightman (1979); Gray (2008); and Dullemond (2012).

2.2.1 *Thermodynamic equilibrium*

We start out by repeating some basic thermodynamics, which is important for radiative transfer. Thermodynamic equilibrium describes a system that is completely isolated from its surroundings so that no exchange of energy takes place, and where matter and radiation have had time to interact with one another to settle into an equilibrium. For such a system the kinetic motions of the particles, their level populations, and the radiation field can all be described by a single parameter, which we call the temperature. The particle speeds are distributed according to the Maxwell-Boltzmann distribution

$$f(v) = 4\pi \left(\frac{m}{2\pi k_B T_{kin}} \right)^{\frac{3}{2}} v^2 e^{-\frac{mv^2}{2k_B T_{kin}}},$$

where k_B is the Boltzmann constant and m is the particle mass. The energy levels of the particles, which could be either molecules or atoms, are populated according to the Boltzmann distribution

$$n_i/N = \frac{1}{\sum_j g_j e^{-E_j/k_B T_{ex}}} g_i e^{-E_i/k_B T_{ex}} = \frac{1}{Z(T_{ex})} g_i e^{-E_i/k_B T_{ex}}, \quad (2.4)$$

where n_i, g_i, and E_i are respectively the population number, statistical weight, and energy of the level. The partition function, $Z(T_{ex})$, is the sum over all possible states the atom or molecule can occupy, and N is the total number of particles. n_i/N is therefore the probability that the particle occupies the i'th energy level and is called the fractional population number. Finally, the thermal radiation field of the system follows Planck's radiation law

$$B_\nu = \frac{2h\nu^3}{c^2} \frac{1}{e^{\frac{h\nu}{k_B T_{rad}}} - 1},$$

where c is the speed of light. In thermodynamic equilibrium the kinetic temperature, T_{kin}, the excitation temperature, T_{ex}, and the radiation temperature, T_{rad} are all equal.

Atoms and molecules can be excited into different energy states through both collisional and radiative processes. At high densities, where collisional interactions dominate, $T_{kin} = T_{ex}$ and the medium is said to be in Local Thermodynamic Equilibrium (LTE). In LTE small regions of the source are in thermodynamic equilibrium with themselves, but not necessarily with the radiation passing through those regions. The high densities associated with regions in LTE also serve to keep the mean free path of photons short so that only a small fraction of radiation escape. The escape of only a negligible amount of radiation, is one of the defining characteristics of blackbodies, from which the Planck radiation law is derived, meaning that the thermal emission from a region in LTE can also be expected to follow Planck's radiation law.

2.2.2 *Fundamental quantities*

The radiative flux, F_ν, can be defined by considering an area, dA, placed in a radiation field. An energy, dE, passes across this area over a given time interval, dt, and over a given bandwidth, $d\nu$. F_ν have cgs units of $\mathrm{erg\,s^{-1}\,cm^{-2}\,Hz^{-1}}$ and is formally defined as

$$F_\nu = \frac{dE}{dA\,dt\,d\nu}.$$

For an isotropic source (a source that emits equally in all directions) the radiative flux is subject to the inverse square law, $F_\nu \propto r^{-2}$, where r is the distance to the source, and can therefore not be considered a fundamental quantity of the source.

It is possible to define another quantity, similar to the radiative flux, which is independent of distance from the source. This quantity, called the radiative intensity, I_ν, has units of $\mathrm{erg\,s^{-1}\,cm^{-2}\,Hz^{-1}\,ster^{-1}}$ and is defined as

$$I_\nu = \frac{dE}{dA\,dt\,d\nu\,d\Omega\,\cos\theta} = \frac{F_\nu}{d\Omega\,\cos\theta},$$

where $d\Omega$ is the solid angle and the dependence on $\cos\theta$ comes about because the projected area of dA becomes smaller as the angle, θ, from the surface normal grows larger. The dependence on the solid angle, $d\Omega$, ensures that I_ν does not depend on the distance from the source.

Detectors on Earth, such as the CCD detectors mounted on optical telescopes or the bolometer detectors mounted on some submm and mm telescopes, measure the radiative flux by collecting all the light that falls into the solid angle extended by the detector pixel on the sky. If the source is extended over several pixels, so that the actual solid angle of the source can be determined, it is possible to measure I_ν directly.

2.2.3 *The radiative transfer equation*

For a ray of light travelling through vacuum the radiative intensity, I_ν, remains constant

$$\frac{dI_\nu}{ds} = 0,$$

where ds is an infinitesimal line segment along the ray. If the radiation propagates through a medium the radiative transfer equation takes the form

$$\frac{dI_\nu}{ds} = j_\nu - \alpha_\nu I_\nu = \alpha_\nu\left(S_\nu - I_\nu\right), \tag{2.5}$$

where the emissivity, j_ν, which is the radiation that is added to the beam along the line of sight, has units of $\mathrm{erg\,s^{-1}\,cm^{-3}\,Hz^{-1}\,ster^{-1}}$

and the extinction coefficient, α_ν, which is proportional the the amount of radiation being removed from the beam, has units of cm^{-1}. $S_\nu \equiv j_\nu/\alpha_\nu$ is known as the "source function"[1], and can be seen from Eq. (2.5) to play the role of "attractor" of the intensity; that is, I_ν will seek to approach S_ν asymptotically.

2.2.3.1 *Dust radiative transfer*

j_ν and α_ν include contributions from both the gas and dust in the system. Despite only making up ~1 % of the mass of the ISM dust is responsible for virtually all continuum absorption and emission. If the emission is thermal then $S_\nu = B_\nu(T)$ and $\alpha_\nu = \rho_{\mathrm{dust}}\kappa_\nu$, where ρ_{dust} is the dust density measured in $\mathrm{g\,cm}^{-3}$. κ_ν is called the mass weighted dust opacity, or simply the dust opacity, and has units of $\mathrm{cm}^2\,\mathrm{g}^{-1}$. κ_ν is a useful quantity because α_ν, which is really the inverse of the mean free path, can intuitively be recognised to be proportional to the local dust density, while κ_ν is a property of the dust. κ_ν can be either calculated or measured for different dust compositions, and tabulations relevant to various kinds of astrophysical problems exists (e.g. Ossenkopf & Henning 1994; Weingartner & Draine 2001).

For thermal dust in a purely absorptive medium, the radiative transfer equation is comparatively easy to solve as it can be integrated directly. However, radiation can also be removed from a ray through the process of scattering, which complicates the picture considerably because this implies that the problem can no longer be solved one ray at a time. The emissivity and extinction coefficient can be split up into their scattering and absorption components: $j_\nu^{\mathrm{tot}} = j_\nu^{\mathrm{emis}} + j_\nu^{\mathrm{scat}}$ and $\alpha_\nu^{\mathrm{tot}} = \alpha_\nu^{\mathrm{abs}} + \alpha_\nu^{\mathrm{scat}}$. After some manipulation Eq. (2.5) can be written as

$$\frac{dI_\nu}{ds} = \alpha_\nu^{\mathrm{tot}}\left[\epsilon_\nu S_\nu^{\mathrm{abs}} + (1-\epsilon_\nu)S_\nu^{\mathrm{scat}} - I_\nu\right],$$

where $\epsilon_\nu = \alpha_\nu^{\mathrm{abs}}/\alpha_\nu^{\mathrm{tot}}$ is the photon destruction probability. For normal thermal emission $S_\nu^{\mathrm{abs}} = B_\nu(T)$, while S_ν^{scat} has to be determined through other means; often S_ν^{scat} is determined using Monte Carlo methods.

1 Note that α_ν has nothing to do with the spectral index, α, used for protostellar classification in Chapter 1. Nor does the source function, S_ν, have anything to do with the SED although their symbols are the same.

2.2.3.2 *Line radiative transfer*

For the gas, absorption and emission takes place over narrow ranges of frequencies, giving rise to so-called spectral lines. For these the emissivity and extinction coefficients can be written as

$$
\begin{aligned}
j_\nu^{\mathrm{gas}} &= \frac{h\nu_0}{4\pi} n_u A_{ul} \phi(\nu) \\
\alpha_\nu^{\mathrm{gas}} &= \frac{h\nu_0}{4\pi} \left(n_l B_{lu} - n_u B_{ul}\right) \phi(\nu),
\end{aligned}
$$

where u and l refer to the upper and lower energy level of the transition. $\phi(\nu)$ is the spectral line profile, which include the various types of broadening spectral lines are subject to, such as thermal broadening, pressure broadening, natural broadening, and any kind of isotropic velocity broadening (e.g. microturbulence). A_{ul}, B_{ul}, and B_{lu} are the Einstein coefficients for spontaneous emission, induced emission, and photo absorption respectively. They are related by

$$
\begin{aligned}
A_{ul} &= \frac{2h\nu_0^3}{c^2} B_{ul} \\
g_l B_{lu} &= g_u B_{ul}
\end{aligned}
$$

In general, the level populations n_i change according to a set of coupled differential equations

$$
\frac{dn_i}{dt} = \sum_{j\neq i}^{N} n_j P_{ji} - n_i \sum_{j\neq i}^{N} P_{ij}, \tag{2.6}
$$

where N is the number of energy levels, and the P_{ij} are the reaction rates given by

$$
P_{ij} = \begin{cases} A_{ij} + B_{ij} J_{ij} + C_{ij} & \text{if } E_i > E_j \\ B_{ij} J_{ij} + C_{ij} & \text{if } E_i < E_j \end{cases} . \tag{2.7}
$$

J_{ij} is the mean intensity integrated over the line

$$
J_{ij} = \frac{1}{4\pi} \int\int \phi(\nu) I_\nu \, d\nu d\Omega,
$$

and $C_{ij} = n_{\mathrm{col}} K_{ij}$ are the collision rates, typically measured in s^{-1}, between the atom or molecule in question and its collision partner. n_{col} is the number density of the collision partner, typically measured in units of cm^{-3}, and K_{ij} is the collision coefficient, typically measured in units of $cm^3\,s^{-1}$. K_{ij} is unique to the collision partner and the atom/molecule in question and is generally dependent on both temperature and the transition in question. K_{ij} is typically available from tabulations, for example, from the Leiden atomic and molecular database[2]. Depending on whether one deals with an atomic or

2 http://home.strw.leidenuniv.nl/~moldata/

molecular gas the most frequent collision partner is most often free electrons or molecular hydrogen. If more than one collision partner is important one can calculate the rates, C_{ij}, between different collision partners independently before adding them together. The time dependence of Eq. (2.6) vanishes once a statistical equilibrium has been established so that $dn_i/dt = 0$, and the solution of the coupled set of differential equations can commence. Because of the dependence of the mean intensity in Eq. (2.6) the statistical equilibrium solution cannot be solved locally, but couples to the rest of the model, and the problem has to be solved iteratively. Specialised codes have been developed to solve this global problem such as `RATRAN`, for one- and two-dimensional problems (Hogerheijde & van der Tak, 2000), and `LIME` for three-dimensional problem (Brinch & Hogerheijde, 2010).

If LTE can be assumed, the process of determining the level populations becomes almost trivial because the populations numbers will be distributed according to the Boltzmann distribution, Eq. (2.4). In LTE only a list of energy levels of the atom or molecule in question and a tabulated partition function is needed to calculate the population numbers (if the list of energy levels is large enough then a tabulated partition function is not even necessary since it can be calculated from the levels themselves). In addition to having to be solved iteratively, the full non-LTE problem also requires knowledge about the collision coefficients, K_{ij}, and the density of the collision partners, n_{col}. As discussed in Sect. 2.2.1, LTE is applicable if collisions can be assumed to be responsible for excitation and de-excitation of the energy levels in the system. To get a sense of whether LTE is applicable or not one can define a critical number density which is the density where a level is just as likely to get de-excited by a spontaneous radiative decay as by a collision with another particle

$$n_{\text{crit}} = \frac{A_{ul}}{\sum_i K_{ui}}.$$

For densities higher than the critical density the medium can be assumed to be in LTE.

2.2.4 *Calculating dust temperatures*

We have so far discussed the origins of j_ν and α_ν for both dust and line radiative transfer. If LTE can be assumed, and in the absence of scattering, solving the radiative transfer equation, Eq. (2.5), for both dust and line radiative transfer is relatively straightforward, except for the fact that we also need to know the temperatures. In general dust and gas temperatures are not equal, but they can be assumed to equilibrate at high densities where collisions dominate.

2.2.4.1 *Dust in thermal equilibrium*

Because of the high dust opacities, dust grains are quick to equilibrate to a thermal balance where they emit as much energy as they absorb. We observe a small amount of dust sitting at some distance away from a star, which supplies a steady stream of photons. The distance from the star is assumed to be large enough that it can be considered a point source, and the dust is assumed to be optically thin at all wavelengths. In radiative equilibrium the heating and cooling rates of the dust are going to be equal, which can be written as

$$\int_0^\infty \kappa_\nu F_\nu^\star \, d\nu = 4\pi \int_0^\infty \kappa_\nu B_\nu(T_{\rm dust}) \, d\nu,$$

where the left term is the the heating rate from the star, and the right term is the cooling rate of the dust. If we assume for a moment that the dust opacities are grey (independent of wavelength), so that they can be taken outside the integrals, this expression can be written as

$$T_{\rm dust} = \left(\frac{F^\star}{4\sigma_{\rm SB}}\right)^{\frac{1}{4}} = \left(\frac{L_{\rm bol}}{8\pi\sigma_{\rm SB}}\right)^{\frac{1}{4}} \frac{1}{\sqrt{r}}$$

$\int_0^\infty F_\nu^\star \, d\nu = F^\star$ is the total flux output of the star, $\int_0^\infty B_\nu(T_{\rm dust}) \, d\nu = \frac{\sigma_{\rm SB}}{\pi} T_{\rm dust}^4$ is the Stefan-Boltzmann law, and $L_{\rm bol} = 4\pi r^2 F^\star$ is the bolometric luminosity of the star.

More generally, if the opacities are not independent of wavelength, the dust temperature can be written as

$$T_{\rm dust} = \sqrt{\frac{R_\star}{2r}} \left(\frac{\kappa_P(T_\star)}{\kappa_P(T_{\rm dust})}\right)^{\frac{1}{4}} T_\star, \tag{2.8}$$

where it has been assumed that the central star emits like a blackbody with radius $R_\star$ and temperature $T_\star$. The Planck mean opacity, $\kappa_P(T)$, is defined as

$$\kappa_P(T) = \frac{\int_0^\infty \kappa_\nu B_\nu(T) \, d\nu}{\int_0^\infty B_\nu(T) \, d\nu} = \left(\frac{\sigma_{\rm SB}}{\pi} T^4\right)^{-1} \int_0^\infty \kappa_\nu B_\nu(T) \, d\nu,$$

and is the average opacity weighted by the Planck emission at a temperature of T. Eq. (2.8) has to be solved iteratively since both sides depend on $T_{\rm dust}$, but convergence is fast. Eq. (2.8) is valid for optical thin dust far from the star. At optical thick wavelengths, dust far away from the star is shielded by the dust further in, and one has to iterate through the radiative transfer equation, Eq. (2.5), to solve the problem.

2.2.4.2 *Monte Carlo calculation of dust temperatures*

Another method to calculate the dust temperatures, is the Monte Carlo method of Bjorkman & Wood (2001), often enhanced with the cell volume method of Lucy (1999). This method, which relies on the propagation of "photon packets" through some cell based model, has many advantages over other type of methods, such as its applicability to three-dimensional models and its ease of use.

Starting from the basics, the method works by taking the energy output of the star (or some other source of heating) over some time interval, Δt, and chopping it up into a number of photon packets, N_γ. The energy of each photon packet is then

$$E_\gamma = \frac{\Delta t L_{bol}}{N_\gamma}.$$

Note that while the individual photon packet are monochromatic, the photon packets do not all share the same frequency, which is sampled according to the spectrum of the heating source. This also means that each photon packet corresponds to a different number of physical photons.

A photon packet is emitted from the star in a random direction. At some point the photon packet is either absorbed or scattered. If the photon packet is absorbed it will dump all its energy into that cell, raising the dust temperature of the cell the process. Assuming thermal equilibrium the photon packet is immediately re-emitted, and the temperature in the cell is updated by calculating which temperature the cell must have to emit all its energy

$$T_i = \left(\frac{N_i L_{bol}}{4 N_\gamma \kappa_P(T_i) m_i \sigma_{SB}} \right)^{\frac{1}{4}}.$$

The index, i, refers to the cell; m_i is the mass of the cell; and $N_i = E_i/E_\gamma$ is the total number of photon packets absorbed by the cell so far.

Optically thin cells have a low probability of ever undergoing an absorption event, even though some of the physical photons in the photon packets will undoubtedly be absorbed. This can be solved by adding a bit of energy to the cell regardless of whether a photon packet is absorbed or not, $E_i := E_i + E_\gamma \alpha_\nu \Delta s$, where Δs is the length of the photon path through the cell. This is the cell volume method of Lucy (1999).

The big question is how to choose a new frequency for the re-emitted photon packet. The probability distribution of photons emitted from a cell should be

$$p(\nu) d\nu = \frac{j_\nu^{emis}}{\int_0^\infty j_\nu^{emis} \, d\nu} d\nu, \tag{2.9}$$

where the cell emissivity, $j_\nu^{emis} = \alpha_\nu B_\nu(T_{final})$, depends on the final temperature of the cell. This naturally poses a problem since calculating the final temperature is the goal of the procedure. The clever point is that $B_\nu(T)$ is a monotonically increasing function for all frequencies so that $B_\nu(T_k) > B_\nu(T_{k-1})$, where k and $k-1$ represent successive absorption events. If α_ν is simultaneously independent of temperature (which is not always the case, in which case the method breaks down), then the emissivity between two successive re-emission events, $j^{\rm emis}_{\nu,k} > j^{\rm emis}_{\nu,k-1}$ for all frequencies. This means that we can define a quantity, $\Delta j_{\nu,k} = j_{\nu,k} - j_{\nu,k-1}$, where after all absorption events

$$j_{\nu,\rm final} = \sum_{k}^{n} \Delta j_{\nu,k}.$$

The probability distribution for individual emission events can be chosen so that

$$p_k(\nu)d\nu = \frac{\Delta j_{\nu,k}}{\int_0^\infty \Delta j_\nu \, d\nu} d\nu,$$

so that, after the final absorption event, the total number of photon packets emitted from the cells will be distributed according to the Eq. (2.9).

2.2.5 *RADMC-3D*

In this work I have used the radiative transfer code `RADMC-3D`[3] (see Dullemond & Dominik 2004 for a description of the two-dimensional version of the code). This code is capable of calculating radiative transfer models of full three-dimensional problems. It uses the method of Bjorkman & Wood (2001) to calculate the dust temperatures with the cell volume method of Lucy (1999) for optically thin cells. In the absence of scattering `RADMC-3D` is able to calculate images by direct integration of Eq. (2.5). If scattering is included the code is able to run a short monochromatic Monte Carlo simulation to determine the scattering source function. `RADMC-3D` also includes a line radiative transfer module, with capabilities of calculating line emission in LTE mode, as well some capabilities of non-LTE calculations (although a full non-LTE solver is not included). Both the dust radiative transfer and line radiative transfer modules of `RADMC-3D` have been used in this work (see Chapters 4 and 5).

3 http://www.ita.uni-heidelberg.de/~dullemond/software/radmc-3d/

3 THE RESEARCH

3.1 SHORT DESCRIPTION

The study of star formation is in an era of rapid development facilitated, in part, by the many new observations that have been made available to the community during the last decade. These observations are predominantly from the space-based telescopes, Spitzer and Herschel, which have provided high-sensitivity surveys at the mid-infrared wavelengths not observable from Earth; and they are from ground-based interferometers such as SMA and ALMA, which are capable of observing at submm and mm wavelengths with sub-arcsecond resolution. Concurrently with the observational advances, numerical simulations of star-forming regions have become both larger and ever-more sophisticated as technological advances have pushed the boundaries of what is computationally achievable.

It is an important task to bring together the fields of observational astronomy and numerical simulations, both because it is important to make sure the simulations are able to reproduce observational results, and because simulations are a useful tool for interpreting the physical reality behind the observations. This project has been focused on doing exactly that, with a particular focus on the evolution of the deeply embedded Class 0 and I protostars. The choice to focus on these objects is motivated partly by the fact that these are some of the objects about which we have increased our knowledge the most in the past decade, partly by the simple truth that they are the objects that are traced best by the simulations that were available to me in this project.

The simulations, that have been used as a basis for this work, have been run using the Adaptive Mesh Refinement (AMR) code `RAMSES`. They are global simulations of molecular clouds with boundary conditions set according to the Larson scaling relations (Larson, 1981), but with enough levels of AMR that they also resolve individual protostellar systems. The protostars that form in these simulations are represented by sink particles, point particles that acquire mass and momentum from the surrounding fluid. Notably, these sink particles do not provide any stellar feedback; instead, the simulations form several hundred of them, meaning that the problem can be studied from a statistical rather than an object-by-object viewpoint.

The method I have used to couple observations and numerical simulations is based on creating synthetic observables (SEDs, images, and line cubes) from the simulation, which can then be compared directly to real observations. This is in contrast to the alternative, which would be to infer physical quantities from the observations and compare these to the same physical quantities in the simulations. Both approaches require some assumptions to be made, but we chose the former approach because the assumptions made when going from "physics" to "observations"-space are generally fewer and more tractable. These assumptions include calculating the feedback from the protostar on its environment, assuming a dust-to-gas ratio, and determining which dust opacities should be used.

The synthetic observables are produced using the radiative transfer code `RADMC-3D`, which is capable of calculating dust continuum images, SEDs, and molecular line cubes. The simulations include several thousand protostellar systems, and for this reason I have written sophisticated python front-ends to both `RADMC-3D` and `RAMSES` to ease the job of producing and analysing the resulting radiative transfer models. The `RADMC-3D` models themselves consist of cubical cut-outs from the simulation with size $30\,000\,\mathrm{AU} \times 30\,000\,\mathrm{AU} \times 30\,000\,\mathrm{AU}$ centred around individual protostars.

3.2 PUBLICATIONS

The research is presented in three papers, which are appended in Chapters 4, 5, and 6. These papers are

1. (Frimann et al. 2016a): Large-scale numerical simulations of star formation put to the test. Comparing synthetic images and actual observations for statistical samples of protostars

2. (Frimann et al. 2016b): Protostellar accretion traced with chemistry. Comparing synthetic $C^{18}O$ maps of embedded protostars to real observations

3. Frimann et al. (in preparation): Protostellar accretion traced with chemistry. High resolution $C^{18}O$ and continuum observations towards deeply embedded protostar in Perseus

Here follows brief summaries of the appended papers.

3.2.1 *Paper I: Large-scale numerical simulations of star formation put to the test. Comparing synthetic images and actual observations for statistical samples of protostars*

The first paper presents a comprehensive analysis of one of the largest simulations of a molecular cloud ever carried out. The simulation is a $5\,\mathrm{pc} \times 5\,\mathrm{pc} \times 5\,\mathrm{pc}$ periodic box of a molecular cloud, and uses AMR to resolve individual protostellar systems down to a cell-size of $8\,\mathrm{AU}$. Using advanced radiative transfer method we create synthetic observables of several thousand simulated protostellar systems.

The paper presents a number of direct comparisons to already published observational studies. We calculate SEDs of the protostars in the simulation and use them to calculate evolutionary tracers, such as bolometric temperatures, T_{bol}, and L_{smm}/L_{bol}. These are then compared to the observed distributions, and are found to match these well. The distribution of protostellar luminosities in the simulations is compared its observational counterpart and is likewise found to match it well. Both examples are important benchmarks of the simulation and indicate that the overall spectral and accretion evolution of the simulated protostars is in agreement with the observations.

Synthetic continuum observations are calculated to determine if an excess of compact emission at small scales around protostars can be used as a method to detect circumstellar disks. We find that the small-scale emission from the simulation is to low compared to the continuum survey of embedded protostars by Jørgensen et al. (2009), which can again be traced back to issues with the spatial resolution. Finally, we study the distance distribution between cores and protostars in the simulation to see how far protostars migrate from their parental core, and find them to be closely associated.

In general, we find that the synthetic observables are able to reproduce many of the observed results, but we are also able to point out some weaknesses of the simulation. Above all, we establish the direct comparison between observations and simulations as a powerful tool for interpreting observations and for benchmarking simulations.

3.2.2 *Paper II: Protostellar accretion traced with chemistry. Comparing synthetic $C^{18}O$ maps of embedded protostars to real observations*

CO is typically frozen-out on dust grains at temperatures $\lesssim 30$ K. Following an accretion burst, which will increase the heating from the protostar, CO will sublimate from the dust grains at large distances from the protostar. After the burst ends the CO will take a while to freeze back out onto the dust grains, meaning that in the intermediate period the enhanced spatial distribution of CO around the protostar, can be used as a tracer of variable accretion. The second paper presents synthetic $C^{18}O$ maps, calculated with radiative transfer methods from a large simulation of a molecular cloud. This simulation is very similar to the one analysed in the first paper, but has better accretion physics and a lower resolution (minimum cell-size of 50 AU. One notable consequence of the latter point is that the simulation does not include any disk physics. The goal of the paper is to study chemical tracers of variable accretion, and simple freeze-out/sublimation chemistry is therefore added to the models during the post-processing stage.

The synthetic maps are compared to the $C^{18}O$ observations presented by Jørgensen et al. (2015), who found $C^{18}O$ to be widely distributed in a sample of 16 embedded protostars, indicating that large accretion variability is common in such objects. Using synthetic observations we confirm that the methodology used in the observational paper is capable of measuring the physical extent of gas-phase CO surrounding a protostar, but are not able to reproduce the observed distribution. We trace this back to the lack of sufficient accretion variability in the simulation, which can likely be traced back to the fact that the simulation does not include disk physics.

3.2.3 *Paper III: Protostellar accretion traced with chemistry. High resolution $C^{18}O$ and continuum observations towards deeply embedded protostar in Perseus*

In the third paper, which is an observational study, we measure the spatial extent of $C^{18}O$ towards a sample of 20 deeply embedded protostars in the Perseus molecular cloud. We also analyse continuum observations of the same sample to see whether a link between episodic accretion events and the presence of disks can be established. The paper can thus be considered a follow-up study of both Jørgensen et al. (2015) and of Paper II.

We find that the distribution of spatial extents of $C^{18}O$ towards the sample of sources is, at least, as wide as that of Jørgensen et al. (2015). We also see a clear trend that low-luminosity sources have a higher probability of having their $C^{18}O$ emission distributed over a large area, compared to the current protostellar luminosity, relative to the high-luminosity sources in the sample. The objects with the most enhanced distribution of $C^{18}O$ are simultaneously some of the objects with the highest excesses of compact emission, which can be perceived as evidence of the presence of a circumstellar disk.

3.3 OUTLOOK

There are several possible directions in which to take the research presented in the three papers summarised above. Here I present ideas and thoughts for possible future projects. Paper I presents a comprehensive analysis of one of the largest simulations of a molecular cloud ever carried out, with one of primary goals being to make sure its predictions agree with observations. Many of the analyses applied to that simulation could be applied to other simulation as long as those simulations are cell-based, and as long as they form enough protostars to make statistical comparisons possible. Calculating distributions of T_{bol}, L_{smm}/L_{bol}, and L_{bol} have been shown in Paper I to be examples of good benchmark tests, partly because the observed distributions are well known, and partly because they tie into fundamental physical and evolutionary questions about star formation. Likewise, it will be interesting to follow the development of new molecular cloud simulations like the ones analysed in the papers as more physics is added to them (e.g. proper stellar evolution models, stellar feedback, simple gas chemistry, etc.), and see how this affects the results of Paper I.

A small project, with ties to the measurements of T_{bol} and L_{smm}/L_{bol} in Paper I, is the question of how the radiation from other stars influence the SED measured of a single protostar. In Paper I we did not include any kind of external heating of the analysed protostars, partly because of the difficulty of doing an automated analysis for a RADMC-3D model where several protostars are contributing, partly because we found in tests that including a generic Interstellar Radiation Field (ISRF) (such as the one by Black 1994) produced anomalous SEDs with too much emission at the shorter wavelengths, likely due to a lack of shielding by ambient cloud. Having access to a global simulation of a molecular cloud, it should be a relatively simple matter to calculate how efficient the ambient cloud is at shielding individual protostellar system from radiation from other stars. This is not an altogether new idea; for example, Shirley et al. (2002) found that it was necessary to reduce the strength of the Black (1994) ISRF by 70 % to obtain good fits for a number of one-dimensional radiative transfer models of protostellar cores. This project would address these questions in a more fundamental manner because of the more realistic cloud structure.

Papers II and III are devoted to the study of protostellar accretion; Paper II from a modelling perspective, and Paper III from an observational perspective. There are a number of ways to bring this research forward. One of the main conclusions of Paper II was that disk physics is a necessary component for the production of accretion bursts. A relatively straightforward extension to the project is to analyse higher-resolution simulations, where the disks are resolved, to see whether this triggers the occurrence of accretion bursts. So-called zoom-in simulations, which are simulations that include the entire molecular cloud so that the boundary conditions are realistic but only resolves one protostellar system, are a good candidate for this extension. Such simulations are being run by the numerical astrophysics group in Copenhagen using the same overall set-up as in the simulation analysed in Papers I and II. Depending on what physics is included in these simulation (the simulations being run currently use an isothermal equation of state) this may also give hints regarding to the relative importance of different types of disk instabilities (gravitational, thermal, MRI).

Because RAMSES is a cell-based code it was not possible to follow the dynamical evolution of the simulated protostellar systems analysed in Paper II. Specifically, a proper treatment of the freeze-out/sublimation problem requires the ability to follow the temporal evolution of individual dust grains. If, for example, the envelope is in the process of collapsing when the luminosity burst happens, then the spatial distribution of gas-phase CO will not only depend on the refreezing time scale, but also on the free-fall time scale. Such dynamical effects can be included in the cell-based simulations through the addition of "tracer particles", which can be embedded in the simulation as passive scalars so that they do not affect the hydrodynamical evolution of the system. The possibility of including tracer particles have been added to the `RAMSES` code by members of the computational astrophysics group in Copenhagen.

One of the biggest uncertainties on the conclusions of Papers II and III is whether or not the sublimation temperature of CO is roughly constant between different astronomical sources. If the sublimation temperature of CO is highly variable then this might explain the large scatter of the $C^{18}O$ extents seen in observations. Because of the difficulty of replicating astronomical conditions in laboratories, and the difficulty of modelling this effect analytically or numerically, this is a problem that is currently best addressed observationally. One way to address this problem would be to replicate the analysis carried out for CO in Papers II and III as well as in Jørgensen et al. (2015), but for some other molecule. The goals of this would be twofold: (1) to see if a distribution of spatial extents similar to that seen for CO can be reproduced; and (2) to compare measurements of individual objects to see if the spatial extent of the new molecule vary "in-phase" with that of CO. A good candidate molecule for such a study would be H_2CO, which has a sublimation temperature that is still low-enough ($\approx$38 K; Aikawa et al. 1997) that the H_2CO can be resolved with an interferometer such as the SMA.

3.4 OWN CONTRIBUTIONS VERSUS CONTRIBUTIONS OF COLLABORATORS

This section details the contribution of myself to the appended papers versus the contributions of co-authors

PAPER I The simulation itself was run by Troels Haugbølle, while I did the entire subsequent post-processing and analysis of the simulation, including the radiative transfer modelling of the 14 000 simulated protostellar systems presented in the paper. I did all the analysis work presented in the paper except for the hierachical multiplicity analysis described in the second paragraph of Sect. 4.3.1. I made all the figures in the paper except for Fig. 4.3, which shows the IMF. I wrote the entire paper except for Sect. 4.2.1 and the second paragraph of Sect. 4.3.1. Both co-authors read and commented on the paper, but any substantial changes were implemented by me.

PAPER II The simulation itself was run by Troels Haugbølle, while I did the entire subsequent post-processing and analysis of the simulation, including the radiative transfer modelling of the simulated protostellar systems presented in the paper. I also developed the method for including freeze-out and sublimation chemistry into the post-processing after discussions with Paolo Padoan. I did all the analysis work presented in the paper apart from the spurious sink analysis described in Sect. 5.2.1. I made all figures in the paper. I wrote the entire paper except for Sect. 5.2.1. All co-authors read and commented on the paper, but any substantial changes were implemented by me.

PAPER III The initial (pipeline) calibration of the observations was carried out by Mike Dunham (the observations themselves were performed in service-mode at the telescope as part of a larger survey). All subsequent reduction and imaging of the data was done by me. I did all the analysis work, made all the figures and wrote the entire paper. The interpretation of the results were discussed with Jes Jørgensen, who also read and commented the manuscript.

Part II

PUBLICATIONS

4

PAPER I: LARGE-SCALE NUMERICAL SIMULATIONS OF STAR FORMATION PUT TO THE TEST. COMPARING SYNTHETIC IMAGES AND ACTUAL OBSERVATIONS FOR STATISTICAL SAMPLES OF PROTOSTARS

Søren Frimann[1], Jes K. Jørgensen[1], and Troels Haugbølle[1]

[1] Centre for Star and Planet Formation, Niels Bohr Institute and Natural History Museum of Denmark, University of Copenhagen, Øster Voldgade 5-7, DK-1350 Copenhagen K, Denmark

Appeared in *Astronomy & Astrophysics*, vol. 587, article no. A59, March 2016

Abstract

Context. Both observations and simulations of embedded protostars have progressed rapidly in recent years. Bringing them together is an important step in advancing our knowledge about the earliest phases of star formation.

Aims. To compare synthetic continuum images and Spectral Energy Distributions (SEDs), calculated from large-scale numerical simulations, to observational studies, thereby aiding in both the interpretation of the observations and in testing the fidelity of the simulations.

Methods. The adaptive mesh refinement code, `RAMSES`, is used to simulate the evolution of a $5\,\mathrm{pc} \times 5\,\mathrm{pc} \times 5\,\mathrm{pc}$ molecular cloud. The simulation has a maximum resolution of $8\,\mathrm{AU}$, resolving simultaneously the molecular cloud on parsec scales and individual protostellar systems on AU scales. The simulation is post-processed with the radiative transfer code `RADMC-3D`, which is used to create synthetic continuum images and SEDs of the protostellar systems. In this way, more than 13 000 unique radiative transfer models, of a variety of different protostellar systems, are produced.

Results. Over the course of $0.76\,\mathrm{Myr}$ the simulation forms more than 500 protostars, primarily within two sub-clusters. The synthetic SEDs are used to the calculate evolutionary tracers T_{bol} and $L_{\mathrm{smm}}/L_{\mathrm{bol}}$. It is shown that, while the observed distributions of the tracers are well matched by the simulation, they generally do a poor job of tracking the protostellar ages. Disks form early in the simulation, with 40 % of the Class 0 protostars being encircled by one. The flux emission from the simulated disks is found to be, on average, a factor ~6 too low relative to real observations; an issue that can be traced back to numerical effects on the smallest scales in the simulation. The simulated distribution of protostellar luminosities spans more than three order of magnitudes, similar to the observed distribution. Cores and protostars are found to be closely associated with one another, with the distance distribution between them being in excellent agreement with observations.

Conclusions. The analysis and statistical comparison of synthetic observations to real ones is established as a powerful tool in the interpretation of observational results. By using a large set of post-processed protostars, which make statistical comparisons to observational surveys possible, this approach goes beyond comparing single objects to isolated models of star-forming cores.

4.1 INTRODUCTION

The study of star formation is in an era of rapid development. Over the last decade, infrared surveys of nearby molecular clouds, e.g. from the Spitzer Space Telescope and the Herschel Space Observatory, have dramatically increased the number of known Young Stellar Objects (YSOs). Additionally, these surveys have contributed to a better understanding of some of the key questions in star formation, including the evolutionary timescales of YSOs and the distribution of protostellar luminosities (see Dunham et al. 2014 for a recent review). At the same time, sub-millimetre and millimetre interferometers, such as the Submillimeter Array (SMA) and the Atacama Large Millimeter Array, have become able to resolve the small-scale structure, around very deeply embedded objects. Such observations have, for example, demonstrated the presence of Keplerian disks around several Class I sources (e.g. Brinch et al. 2007b; Lommen et al. 2008; Harsono et al. 2014), and around a few Class 0 sources (Tobin et al., 2012; Murillo & Lai, 2013; Lindberg et al., 2014).

Increasing computing power has also fuelled significant progress in the field of numerical simulations. For example, a number of studies following the collapse of protostellar cores and the formation of disks and outflows have recently appeared (e.g. Commerçon et al. 2012a,b; Santos-Lima et al. 2012, 2013; Li et al. 2013; Myers et al. 2013; Seifried et al. 2013; Nordlund et al. 2014). Such studies typically follow the collapse of a single core, resulting in the formation of a single star. Using Adaptive Mesh Refinement (AMR) it is possible to simulate a molecular cloud on parsec scales, while simultaneously resolving the environment around individual protostars on AU scales (Padoan et al. 2012, 2014; Haugbølle et al. in preparation). The advantages of this approach are that the influence of the large-scale environment, on the protostellar evolution, is automatically included, and that a global simulation, which forms a large number of protostars, makes it possible to study star formation in the simulation in a statistical manner.

It is an important task to bring together the fields of observations and numerical simulations. Simulations can provide valuable insights into the physics behind observations, while observations are important for validating the simulations. Typically, such validations are done by inferring a physical parameter from the observations, e.g. the Initial Mass Function (IMF), which is then compared to the same parameter in the simulation. Another option is to use forward modelling, and create synthetic observables from the simulations, which can then be compared directly to observations (Padoan et al., 1998). The advantage of the latter approach is that it is generally easier, and involves fewer assumptions, to transform a three-dimensional physical model to synthetic observables, than the other way around. Examples of studies that use synthetic observables to predict observational signatures of different types of YSOs include Commerçon et al. (2012a,b) who predicted the observational signatures of first hydrostatic cores, Dunham & Vorobyov (2012) who studied episodic accretion as a solution to the luminosity problem, and Mairs et al. (2014) who looked at the evolution of starless cores in molecular clouds.

This paper presents synthetic continuum images and SEDs[1] of protostars created from a simulation with an unprecedented spatial dynamic range of 2^{17} ($\approx 130\,000{:}1$), encompassing simultaneously molecular cloud and protostellar system scales. The synthetic observables are compared directly with a number of observational studies. The outline of the paper is as follows: Section 4.2 introduces the numerical simulation and the post-processing used to create the synthetic observables. Section 4.3 describes the physical characteristics of the simulation, including the identification of cores and disks. Section 4.4 deals with protostellar classification and the ability of observationally defined tracers to follow the physical evolution of protostellar systems. Section 4.5 compares the synthetic images and SEDs to three different observational studies: Section 4.5.1 focuses on disk formation, compared to the continuum survey of Jørgensen et al. (2009); in Sect. 4.5.2 we compare the Protostellar Luminosity Function (PLF) in the simulation to its observed counterpart (Dunham et al., 2014); and in Sect. 4.5.3 we study the relationship between protostellar cores and protostars, compared to submm and infrared continuum images from Perseus and Ophiuchus (Jørgensen et al., 2008). Finally, Sect. 4.6 summarises the findings of the paper.

4.2 METHODS

This section introduces the simulation and the post-processing methods used for creating the synthetic images and SEDs. Only a short description of the technical aspects of the simulation and of the sink particle implementation is presented here, while a more detailed discussion of the sink particle implementation is given in Haugbølle et

1 The synthetic observables and the various calculated parameters presented in the paper have been made available on-line on the web-page: http://starformation.hpc.ku.dk/index.php/synthetic-observations

al. in preparation. Preliminary results from that study were used as guidance for selecting the numerical parameters of this simulation. We also refer to Padoan et al. (2014), who presented a simulation very similar to the one analysed in this paper.

4.2.1 *The numerical simulation*

The simulation is carried out using the public AMR code RAMSES (Teyssier, 2002), modified extensively to include random turbulence driving, a novel algorithm for sink particles, and many technical improvements allowing for efficient scaling to thousands of cores. It is one of the largest simulations of a star-forming region ever carried out in terms of number of cells, dynamic range, and number of iterations, and required approximately 15 million CPU hours on the JUQUEEN supercomputer. More than 400 snapshots, with a 5000 yr cadence, were stored generating 20 TB of raw data and 5 TB of post-processed data.

4.2.1.1 *Initial conditions and physical setup*

We used a finite volume MUSCL scheme with an HLLD method to solve the compressible ideal magnetohydrodynamics (MHD) equations (Teyssier et al., 2006; Fromang et al., 2006) with an isothermal equation of state in a periodic box. The model is initialised with a uniform number density of $n_0 \approx 500\,\mathrm{cm}^{-3}$, a constant magnetic field strength of $B_0 = 9.4\,\mu\mathrm{G}$, and zero velocity. To create a supersonic turbulent medium, reminiscent of a molecular cloud, we drive the box with a smooth acceleration corresponding to a stirring of the gas. The turbulent driving is done with a solenoidal random forcing in Fourier space at wave numbers $1 \leqslant k \leqslant 2$ ($k = 1$ corresponds to the box-size). A solenoidal force is chosen to guarantee that collapsing regions are naturally generated in the turbulent flow, rather than directly imposed by the driving force. The amplitude is such that the three-dimensional rms sonic Mach number, $\mathcal{M}_s \equiv \sigma_{v,3D}/c_s$ (where $\sigma_{v,3D}$ is the three-dimensional rms velocity, and c_s is the speed of sound), is kept at an approximate value of 17.

To scale the simulation to physical units, we adopt a temperature $T = 10\,\mathrm{K}$ and a size $L_{box} = 5\,\mathrm{pc}$, which yields $\sigma_{v,3D} \approx 3.2\,\mathrm{km\,s}^{-1}$ (consistent with observed line-width size relations), $M_{box} \approx 3670\,M_\odot$ (assuming a mean molecular weight of 2.37), and a free-fall time, $t_{ff} \approx 1.5\,\mathrm{Myr}$. Gravity is not included during the first 15 dynamical times ($t_{dyn} \equiv L_{box}/(2\sigma_{v,3D}) \approx 1.5\,\mathrm{Myr}$), so that the turbulent flow can reach a statistical steady state, and the magnetic energy can be amplified to its saturation level (Federrath et al., 2011). Afterwards, the simulation is continued with gravity for a period of $0.77\,\mathrm{Myr}$ (one dynamical time). As shown below, this is marginally long enough to

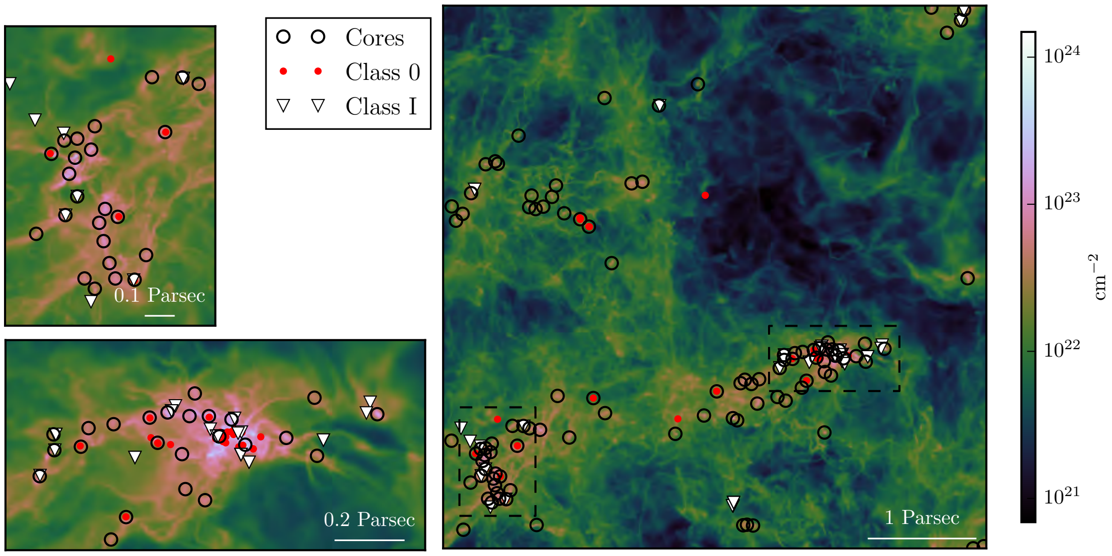

Figure 4.1: Gas column density, protostars, and cores in the simulation 0.6 Myr after the formation of the first protostar. The total number of embedded protostars at this point is 94.

allow for the formation of stars of a few solar masses, and thus to sample the Salpeter range of the stellar IMF.

The virial parameter, defined as $\alpha_{\rm vir} \equiv (5/6)\,\sigma^2_{v,3D}\,L_{\rm box}/(GM_{\rm box})$ (Bertoldi & McKee, 1992), is $\alpha_{\rm vir} = 2.64$. This parameter expresses the ratio between kinetic and gravitational binding energy for a uniform isothermal sphere. Its application as an approximate estimate of such energy ratios in simulations is non-trivial, partly because of the shape and periodic boundary conditions of the numerical box, and partly because of the filamentary distribution of the turbulent gas (Federrath & Klessen, 2012). The high global value of the viral number means that our box corresponds to a loosely bound low-mass star-forming cloud. However, as can be seen in Fig. 4.1, clusters with much lower viral numbers are formed locally in the turbulent flow, with star formation happening predominantly within two subclusters inside the box.

4.2.1.2 *Numerical parameters and the sink particle model*

The root grid of the AMR simulation contains 512^3 computational cells with a minimum spatial resolution (in the lowest density regions) of $\Delta x_{\rm root} = 5\,{\rm pc}/512 = 0.01\,{\rm pc}$. We use 8 refinement levels, each increasing the spatial resolution by a factor of two. Therefore the maximum spatial resolution (in dense regions) is $\Delta x = 8\,{\rm AU}$. The refinement criterion is based only on density: wherever the density on the root grid, first, and second refinement level are larger than 8, 64, and 512 times the mean density, one refinement level is added, increasing the resolution by a factor of two. Further levels are added for each increase in density by a factor of 4, to keep the shortest Jeans length resolved with at least 12 cells at all levels.

A sink particle is created at the highest level of refinement, when the gas density increases above $n \geqslant n_{max} = 8 \times 10^9\,\mathrm{cm}^{-3}$ corresponding to $L_J \leqslant 6\,\Delta x$. To create a sink particle it is also required that the gravitational potential has a local minimum in the cell, and that the velocity field is converging, $\nabla \cdot \mathbf{u} < 0$. Furthermore, sink particles cannot be created inside an exclusion radius of $r_{excl} = 12\,\Delta x$ around already created sink particles. These conditions for sink particle creation are similar to those implemented in previous works (Padoan et al., 2012, 2014; Bate et al., 1995; Krumholz et al., 2004; Federrath et al., 2010; Gong & Ostriker, 2013).

A sink particle is first created without any mass, but is immediately allowed to accrete. In this simulation, it accretes from cells that are closer than an accretion radius of $r_{acc} = 3\,\Delta x = 24\,\mathrm{AU}$, as long as the gas in those cells has a density above a threshold of $n_{acc} = 4 \times 10^9\,\mathrm{cm}^{-3} = 0.5\,n_{max}$. Only gas above this threshold is accreted from the cell and onto the sink particle, bringing the gas density slightly below the threshold in the process. The momentum of the sink particle is changed in accordance with the momentum of the accreted gas, while no magnetic flux is accreted, or removed from the remaining gas. In nature, some flux is lost due to reconnection and non-ideal effects close to the protostar, on scales smaller than what is reached in this simulation, but this would be non-trivial to include correctly in a sub-scale model, while maintaining the magnetic field solenoidal.

In nature, YSOs lose a large fraction of their mass due to winds and jets, launched from small scales not included in the simulation. To account for this mass loss, we apply an efficiency factor, $\epsilon_{wind} = 0.5$, to all accretion rates and sink particle masses *after* the simulation has finished running. Compared to newer versions of the code, where the mass is removed in situ while running the code (Padoan et al., 2014), and high-resolution zoom-in models around single stars (Nordlund et al., 2014), this has been shown to be an appropriate value for the resolution used in this simulation.

The characteristic time-step size, of the highest resolution cells in the simulation, is $\Delta t \sim 40\,\mathrm{days}$, resulting in roughly 7×10^6 iterations over the $0.77\,\mathrm{Myr}$ evolution. At the end of the simulation 505 sink particles have been created, containing $3.4\,\%$ of the total initial gas mass. The parameters of the simulation are summarised in Table 4.1.

To model *ab initio* the formation of individual stars, it is necessary to include much larger scales than those of pre-stellar cores, to avoid imposing ad hoc boundary and initial conditions. By driving the turbulence on a scale of $5\,\mathrm{pc}$, the formation of cores in the simulation is solely controlled by the statistics of the supersonic MHD turbulence, which naturally develops during the initial evolution of 15 dynamical times with no self-gravity. Furthermore, a box size of 5 pc allows the simulation to generate a large number of protostars, sampling well the statistical distribution of conditions for core formation in the turbulent flow.

The size of the root grid is chosen to be able to resolve the turbulence well everywhere. The maximum spatial resolution of 8 AU is partly dictated by the computational cost of the simulation, and by the goal of following the evolution of a large number of protostars with high enough resolution to resolve their disks in the embedded phase. In the rest of the paper we will refer to the sink particles as "protostars".

4.2.2 *Post-processing*

The first step in producing synthetic observables from the simulation is to calculate the temperatures of the dust, that are heated by the protostar. To do this, we use the dust radiative transfer code `RADMC-3D`[2] (see Dullemond & Dominik 2004 for a description of the 2D version of this code). `RADMC-3D` can handle AMR grids natively, and it is therefore not necessary to resample the density structures from the simulation onto a regular grid.

The total protostellar luminosity, $L_\star$, is modelled as the sum of the accretion luminosity, L_{acc}, due to mass accretion onto the protostar, and the photospheric luminosity, L_{phot}, due to deuterium burning and Kelvin-Helmholtz contraction

$$L_\star = L_{acc} + L_{phot} = f_{acc}\frac{G\dot{m}m_\star}{r_\star} + L_{phot}.$$

Here, $m_\star$ is the mass of the protostar, $\dot{m}$ the accretion rate onto the protostar, $r_\star$ the protostellar radius, and f_{acc} is the fraction of accretion energy radiated away. L_{phot} is calculated using the pre-main-sequence tracks of D'Antona & Mazzitelli (1997), where we follow Young & Evans (2005) and add 100 kyr to the tabulated ages, to account for the time difference between the beginning of core-collapse and the onset of deuterium burning. The accretion rate, $\dot{m}$, is calculated by recording the protostellar mass difference between individual snapshots. The typical snapshot cadence is $\approx$5000 yr meaning that the accretion rates are averaged over this time interval. To calculate the accretion luminosity, we assume a stellar radius of $2.5\,R_\odot$, while f_{acc} is assumed to be 1. All protostars are assumed to emit as perfect black bodies with an effective temperature, T_{eff}, of 1000 K.

The simulation contains more than 500 protostars and 200 million cells, and, because of memory constraints, the dust temperatures cannot be calculated simultaneously in the entire simulation. Instead, `RADMC-3D` is run on cubical cut-outs centred around individual pro-

2 http://www.ita.uni-heidelberg.de/~dullemond/software/radmc-3d/

tostars. These cut-outs have side lengths of ≈30 000 AU, where the exact sizes depend on the arrangement of the AMR levels. The cut-outs are made by cycling through each protostar in each snapshot, with every cut-out corresponding to one RADMC-3D model. Applying this procedure stringently, would yield a total of 44 531 RADMC-3D models. However, as described below, a number of reductions are made to this sample, bringing the total number of unique RADMC-3D models down to 13 632. Each individual cut-out may contain several protostars, but for each RADMC-3D model only one source of luminosity, originating from the central protostar, is included (see Appendix 4.8 for a discussion about how the inclusion of multiple sources of luminosity would affect the results).

Because of the technical set-up of the code, the simulation is not representative for more evolved protostars. The refinement criterion for the AMR levels depends solely on density, which is sufficient to follow the gravitational collapse. However, once the central density in a protostellar system falls below a certain threshold value, the spatial resolution starts dropping as well. A lower resolution leads to an increase of the the numerical viscosity, which in turn increases the rate with which the remaining material close to the protostar is either accreted or dispersed, accelerating the process, and leaving a "naked" protostar behind. To follow the protostellar evolution into the less embedded phases, it would be necessary to change the refinement criteria to retain high resolution around the protostars, even when the density in the inner regions start dropping. For late evolutionary stages the radiation of the central protostar on the physical structure (in particular, in the circumstellar disk) also becomes increasingly important. Consequently, in the following analysis, we will only use the embedded objects, and require the environments around the protostars to be as well resolved as possible: to include a system in the analysis, we require that the protostar lie in an AMR cell of level 5 or higher, corresponding to a cell size $< 63\,\mathrm{AU}$ and a minimum number density of $4 \times 10^6\,\mathrm{cm}^{-3}$.

Some protostars are too faint to be detected by infrared surveys, like the Cores to Disks (c2d) Spitzer survey (Evans et al., 2009) and similar. Such survey are typically complete down to a luminosity of $\sim 0.05\,\mathrm{L}_\odot$. In the simulation, we therefore assume that all protostars with a luminosity below this value are too faint to be detected, and they are removed from the sample.

We assume a uniform dust-to-gas mass ratio of 1:100 everywhere, and make use of the dust grain opacities of Ossenkopf & Henning (1994), corresponding to coagulated dust grains with thin ice mantles at a density of $n_{\mathrm{H}_2} \sim 10^6\,\mathrm{cm}^{-3}$. These opacities have been found, by several studies (e.g. van der Tak et al., 1999; Shirley et al., 2002, 2011), to be appropriate for dense cores. The opacities do not extend beyond 1.3 mm, and are therefore extrapolated at longer wavelengths,

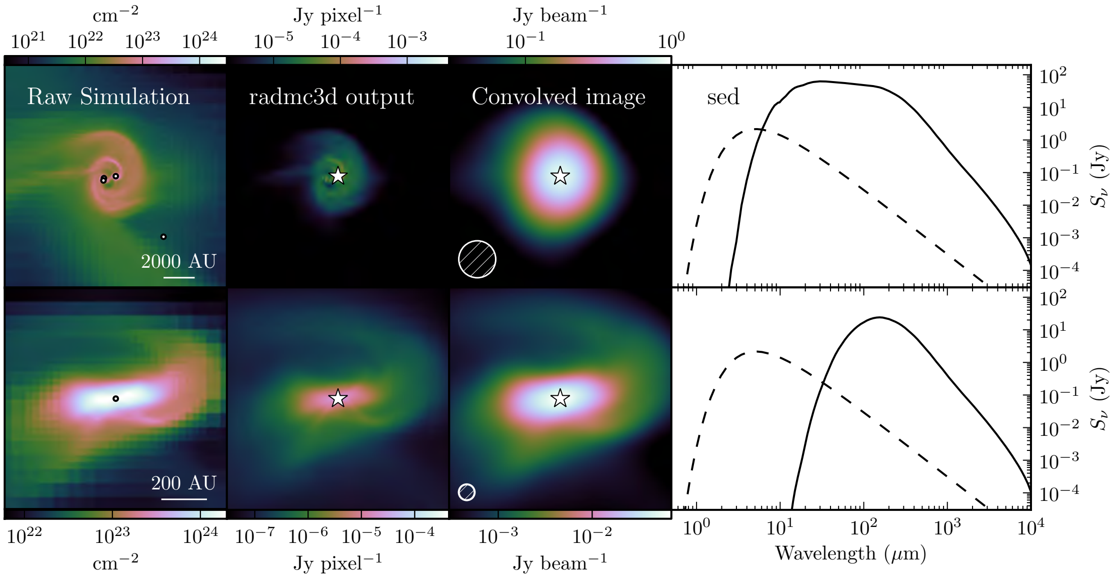

Figure 4.2: From raw simulation to synthetic observables for two different systems. From left to right: projected gas column density from the raw simulation, with dots indicating protostars; 850 µm RADMC-3D continuum images; continuum images after convolving with a Gaussian beam (Top: 15″. Bottom: 0.5″); SEDs of the systems, the dashed lines are the SEDs of the central protostars. The assumed distance to both systems is 125 pc.

using a power law ($\kappa_\nu \propto \nu^\beta$ with $\beta = 1.7$). RADMC-3D takes absorptive dust opacities, $\kappa_{\rm abs}$, as input while the opacities tabulated in Ossenkopf & Henning are total ones, including both scattering and absorption, $\kappa_{\rm tot} = \kappa_{\rm abs} + \kappa_{\rm scat}$. Dunham et al. (2010) demonstrated that $\kappa_{\rm scat}$ dominates over $\kappa_{\rm abs}$ between 0.1 µm and 10 µm. This study is mainly concerned with longer wavelengths, where scattering can be safely ignored.

RADMC-3D uses the Monte Carlo method of Bjorkman & Wood (2001) to calculate the dust temperatures. This method relies on the propagation of a number of "photon packets" through the model, which, in our case, has been set to one million. The optically thin parts of the resulting temperature profiles roughly follow a power law, $T_{\rm dust} \propto r^{-\beta}$ with $\beta \approx 0.4$.

Once the dust temperatures have been calculated, RADMC-3D is used to calculate continuum images and SEDs (see Fig. 4.2 for two examples). The continuum images are subsequently convolved with a Gaussian beam to simulate single-dish observations, or sampled in the (u, v)-plane to simulate interferometric observations. The SEDs are calculated by integrating the emission over a square aperture with side lengths of 2250 AU, corresponding to 15″ at 150 pc, centred around the central object. As standard, three orthogonal directions

Table 4.1: Simulation parameters.

L_{box} (pc)	M_{box} ($M_\odot$)	$\langle n \rangle$ (cm^{-3})	Δx_{min} (AU)	Δx_{max} (AU)	t^a (Myr)	$N_{snapshot}$	N_{star}	$N_{model}{}^b$
5	3670	505	8	2014	0.76	188	505	13 632

Notes. [a] Age of oldest protostar at the end of the simulation. [b] Total number of RADMC-3D models. Note, that because of reductions to the sample, and the fact that not all protostars are present in all snapshots, the total number of models is not equal to $N_{star} \times N_{snapshot}$ (see Sect. 4.2.2 for more details).

are sampled when calculating continuum images and SEDs, effectively increasing the amount of data with a factor of three.

4.3 PHYSICAL DESCRIPTION OF SIMULATION

4.3.1 *General overview*

Table 4.1 summarises key parameters of the simulation. The mean gas density in the simulation is within a factor of two of several nearby molecular clouds, such as Cha II, Lupus, and Ophiuchus (Evans et al., 2009). Of these, the simulation resembles Ophiuchus, which is still actively forming stars, the most. Approximately 80 $M_\odot$, or 2 %, of the gas in the cloud is found to lie at column densities $< 2 \times 10^{21}$ cm^{-2}, corresponding to a visual extinction threshold $A_V < 2$ mag (Bohlin et al., 1978). This is the same threshold used by Evans et al. (2009) to determine the masses of the clouds in the c2d Spitzer survey. The exact value depends somewhat on the orientation of the cloud relative to the observer, the assumed resolution of the extinction maps, and the age of the cloud, but in any case the majority of the material in the simulation is found in regions with $A_V \geqslant 2$ mag.

Our molecular cloud simulation reproduces well the Salpeter slope of the IMF, except for a clear overproduction of brown dwarfs, relative to the Chabrier system IMF (Chabrier, 2003) (see Fig. 4.3). We have made a hierarchical multiplicity analysis, which shows that, at the end of the simulation, the protostars are distributed in 389 single star systems; 56 stars in 28 binaries; 18 stars in 6 triple systems, and 42 stars in 6 multiple systems, including two systems with 11 and 13 members. The median seperation in the binary systems is 150 AU, which is higher than what is found observationally. This is a consequence of the 8 AU cell resolution, and the 96 AU exclusion radius, which preclude the possibility of modelling binaries resulting from disk fragmentation. Most of the brown dwarfs are formed in two dense sub-clusters, and are dynamically expelled at a young age. This

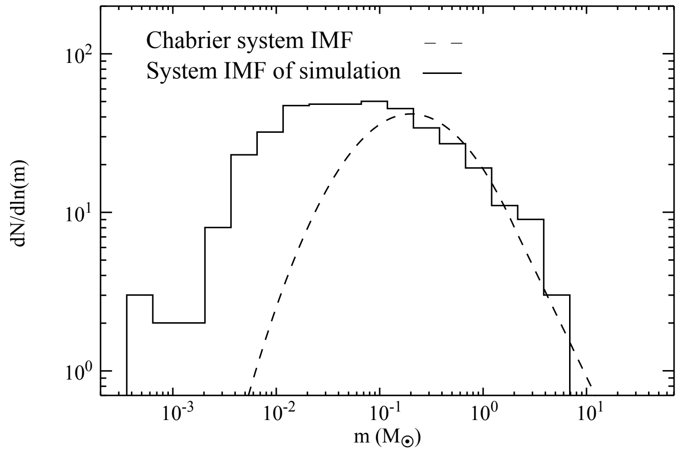

Figure 4.3: Initial mass function in the simulation containing ~500 protostars distributed in 429 systems and sampled 0.76 Myr after the formation of the first protostar. The dashed line is the corresponding Chabrier system IMF. We have excluded stars, which either have an accretion rate above $1 \times 10^{-5}\,M_\odot\,yr^{-1}$ (2 stars), would double their mass in less than 100 kyr (9 stars), or stars which are younger than 50 kyr (23 stars). This removes objects, which would not normally be included in an IMF, because they are heavily embedded, either due to young age or high accretion rates.

brown dwarf population does not affect the conclusions in the paper: most of them are not included in the post-processing, due to low accretion rates, and because of their low mass, they do not affect the mass reservoir available for the rest of the protostars.

Figure 4.1 shows the gas column density and positions of the embedded protostars and cores in the simulation 0.6 Myr after the formation of the first protostar. The total number of cores and protostars identified in the figure are 102 and 94 respectively. The number of protostars differs from the 505 listed in Table 4.1 because not all protostars have formed at this point, and because some protostars have been removed from the sample as described in Sect. 4.2.2.

Looking at Fig. 4.1, it is clear that protostars and cores tend to cluster around regions of high column density; something which is also observed in nature (e.g. Evans et al. 2009). Most of the star formation in the simulation is situated in two sub-clusters, roughly identified by the rectangular inserts in Fig. 4.1. The two clusters, defined by the inserts, both have a cross sectional area of $0.7\,pc^2$ and roughly the same mass ($285\,M_\odot$ and $276\,M_\odot$ respectively). The more massive cluster hosts 57 embedded protostars and 24 cores, while the less massive one hosts 15 embedded protostars and 24 cores. The two clusters began forming stars at roughly the same time, so this discrepancy is not due to time differences in the onset of star formation. An alternative explanation for the discrepancy is variations in the local density, and therefore virial numbers, reflected in the local star formation rates (Padoan et al., 2012). The gas in the less massive cluster is more dispersed than the gas in the massive cluster, which is concentrated around a very dense central region where the majority of the Class 0 protostars are located. More quantitatively, ~20 % of the gas mass in the massive cluster lie at column densities $>1 \times 10^{23}\,\mathrm{cm}^{-2}$, while the same is only true for ~2 % in the less massive cluster. In total, 77 % of the embedded protostars, and 47 % of the cores, shown in Fig. 4.1, are located in one of the two clusters.

4.3.2 *Cores in the simulation*

Dense cores are the smallest units in the hierarchical structure that molecular clouds are made up of, and can be defined as over-dense regions in the molecular cloud, corresponding to local minima of the gravitational potential. Typically, one distinguishes between protostellar and starless cores, depending on whether they are associated with a protostar or not. Observationally, dense cores are most readily detected by their continuum emission in the submm wavelength range. To this end, we have created synthetic 850 μm continuum images of all the protostars in the simulation, which are used to identify and characterise the cores in the simulation. Because of the finite sizes of the cut-outs, this method misses starless cores lying at distances $\gtrsim 15\,000$ AU from their nearest protostar. At 850 μm, the dust can be expected to be optically thin, and we can therefore include the missing regions by converting the raw column density maps, from the simulation, into dust continuum images using the formula, $S_\nu = N\kappa_\nu B_\nu(T_d)$. Here, N is the dust column density, κ_ν the dust opacity, and $B_\nu(T_d)$ the Planck function at a dust temperature, T_d, which we assume to take a value of 10 K. The continuum images are convolved with a Gaussian beam with Full Width at Half Maximum (FWHM) of 18″, assuming a distance to the cloud of 250 pc. The cores are identified and characterised using the core-finding algorithm, `CLFIND2D` (Williams et al., 1994). To accept something as a core, we require its peak flux to be $>0.15\,\mathrm{Jy\,beam}^{-1}$, and that it is resolved (radius > 9″). These choices were made to match the methodology used in the observational studies of Kirk et al. (2006); Jørgensen et al. (2008), to which the core list is compared in Sect. 4.5.3.

There are significant overlaps between the continuum images used for detecting the cores, and hence also a risk of counting individual cores several times. This is solved by checking the final list of cores for overlaps. In case two or more cores overlap, only the core with the highest peak flux is kept, while the rest are discarded. On average, we find approx 100 cores per snapshot, when assuming a cloud distance of 250 pc. Heating from the protostars increase the submm emission, and thereby also the number of core detections, meaning that this number depends on the number of protostars to a large degree, and on the assumed cloud projection and overall cloud evol-

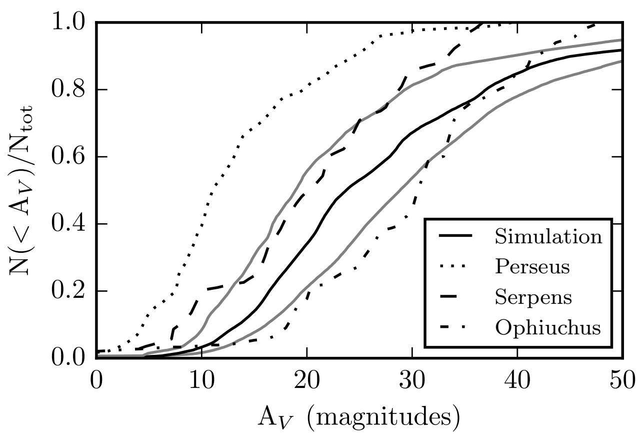

Figure 4.4: Cumulative distributions of visual extinctions of cores in the simulation, along with observations of Perseus, Serpens, and Ophiuchus from Enoch et al. (2007). The black solid line the simulated extinction curve, assuming a resolution of 90″ and a distance of 250 pc. The grey solid lines show the effect of increasing/decreasing the resolution by a factor of four.

ution to a smaller degree. The earliest snapshots, with only a handful of protostars, contain ~60 cores, while, onwards of 0.3 Myr after the formation of the first protostar, ~110 cores per snapshot are detected.

Studies of submm emission and extinction maps of molecular clouds suggest the existence of an extinction threshold, or equivalently a column density threshold, for core formation at $A_V \sim 8$ (Johnstone et al., 2004; Enoch et al., 2007; Konyves et al., 2013). Such a threshold is predicted theoretically by McKee (1989), whose model of photoionisation regulated star formation prohibits core collapse at extinctions $A_V \lesssim 4-8$. An alternative explanation for the observed extinction threshold is that cores are a product of Jeans fragmentation, and therefore primarily appear in the densest regions of the cloud (Larson, 1985).

The simulation is isothermal MHD, and does not include any ionising radiation, so any production of an extinction threshold, similar to that seen in observations, cannot be explained by the presence of photoionising radiation. To test for a possible extinction threshold of the cores in the simulation, we first convert the raw column density maps of the full simulated box into visual extinction maps using the conversion $\langle N_{H_2} \rangle / A_V \approx 1 \times 10^{21}\ \mathrm{cm^{-2}\ mag^{-1}}$ (Bohlin et al., 1978). By comparing the extinction maps to the positions of the cores, identified by their submm emission as described above, the visual extinction of all cores can be calculated and compared to observations.

The black solid line in Fig. 4.4 shows the cumulative distribution of core extinctions in the simulation, which clearly reproduces an extinction threshold like that seen in observations. Observed distributions from Perseus, Serpens and Ophiuchus, taken from Enoch et al. (2007), are plotted along with the synthetic data for comparison. The extinction maps, used by Enoch et al. (2007), have a resolution of 90″ so the synthetic extinction maps have been down-sampled by running a two-dimensional median filter across them with the same resolution, while assuming a distance to the cloud of 250 pc. The grey lines show the effect of increasing/decreasing the resolution of the extinction maps by a factor of four, and has the effect of shifting the distribution ≈5 mag towards higher extinctions when increasing the resolution, and vice versa when decreasing the resolution.

A glance at Fig. 4.4 reveals that the simulated distribution lies between the Serpens and Ophiuchus distributions. The shape of the simulated distribution is similar to the observations, with the notable difference that the simulated distribution has a tail towards high extinctions, not seen in any of the observed clouds. This tail is a result of the very dense cluster described at the end of Sect. 4.3.1, which likely has no counterpart in any of the observed local star-forming regions. An alternative explanation is that background stars cannot normally be detected through the densest regions of the observed clouds, meaning that the highest column densities might be missed in the observed extinction maps.

There are distinct differences between the observed cumulative distributions of Perseus (distance of 250 pc, Enoch et al. 2006), Serpens (415 pc, Dzib et al. 2010), and Ophiuchus (125 pc, de Geus et al. 1989). This is not simply a question of distance as Serpens is furthest away of the three clouds, while its cumulative distribution is intermediate between the other two. As shown in Fig. 4.4, changing the resolution by a factor of four (equivalent to changing the assumed distance by a factor of two), is sufficient to explain the difference between the Serpens and Ophiuchus distributions, which are matched well by the two grey lines. The fact that the Perseus distribution is not reproduced indicate that environmental factors also play a role. A detailed study into the nature of these environmental differences, and how they relate to the simulation, is beyond the scope of this work.

4.3.3 *Disks in the simulation*

The question of disk formation is a central one for observers and modellers alike. Rotationally supported, or *Keplerian*, disks form as a consequence of angular momentum conservation, and are characterised by their rotational velocity profile, $v_\phi(r) \propto r^{-0.5}$. Magnetically supported *pseudodisks* may develop in magnetised cores prior to the formation of Keplerian disks, as magnetic pinching forces deflect infalling material away from the radial direction and towards the disk's midplane (Galli & Shu, 1993a,b). Magnetically supported pseudodisks are not expected to have the same rotation profiles as Keplerian disks; instead one may assume that the infalling material, in such disks, conserve specific angular momentum, which suggests $v_\phi(r) \propto r^{-1}$ (Belloche, 2013).

4.3.3.1 *Disk detection methods*

With a sample consisting of more than 13 000 individual objects, a simple, yet robust, method for determining if a given system contains a disk, is needed to be able to draw conclusions based on statistics. We have devised a method for this, which we will call the α-angle method, based on the ratio between the radial and rotational motions in a system. The first step is to find the rotation axis, $\vec{\Omega}$, of the system.

$$\vec{\Omega} = \frac{\sum_i \rho_i \cdot \vec{r}_i \times \vec{v}_i}{\sum_i \rho_i},$$

where the sum is over all cells located within a radius of 400 AU from the protostar. ρ_i, $\mathbf{r_i}$ and $\mathbf{v_i}$ are respectively density, position and velocity of individual cells relative to the central protostar. The result is weighted with density to make the disk's high-density midplane count more towards the determination of the rotation axis. We find that this gives a robust determination of the disk plane, except for the cases where the central protostar is associated with one or more companion protostars, which may interfere with the determination of the rotation axis. Approximately 40 % of the protostars, in the sample, are accompanied by one or more protostellar companions within the 400 AU inclusion radius. In the following, these systems are disregarded.

Using the rotation axis as a reference, the velocities can be resolved into radial and rotational components, v_r and v_ϕ, where v_r is defined such that the outward direction is positive. We go on to calculate the mass weighted averages of these velocities, $\langle v_r \rangle$ and $\langle v_\phi \rangle$, within a radius of 400 AU from the protostar. The final result is the angle, α, defined as

$$\alpha \equiv \arctan \frac{-\langle v_r \rangle}{\langle v_\phi \rangle}.$$

α is the angle between the "average" velocity vector of the gas in the system and the $\hat{\boldsymbol{\phi}}$ unit vector. $\alpha = \pi/2$ thus corresponds to a system of purely infalling material, $\alpha = 0$ to pure rotation, and $\alpha = -\pi/2$ to pure outflow. This way of characterising the relationship between radial and rotational motions was first introduced by Brinch et al. (2007a), and first used in the context of a numerical simulations by Brinch et al. (2008). By manually inspecting a large number of systems, we determine that disks are mainly found for values of α lying in the range, $0 \leqslant \alpha \leqslant 0.2\,\pi/2$, which is the criterion adopted for claiming the presence of a disk using this method.

The α-angle method is not able to distinguish between Keplerian disks and other types of rotating structures. In an effort to test the

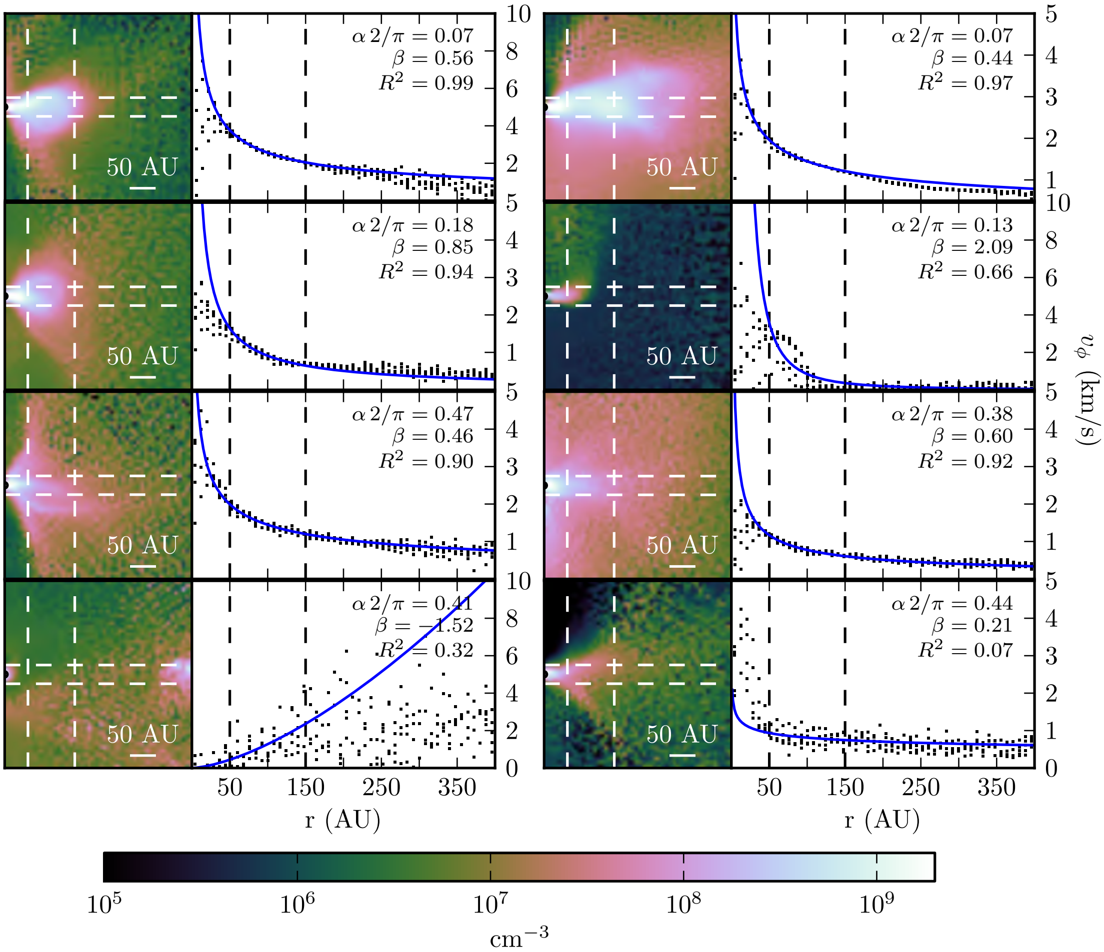

Figure 4.5: Examples of disks in the simulation. The dashed lines indicate the regions used for fitting the rotation curves for the power law method. The blue solid line in each panel is the best fitting power law. In the top right corner of each panel is given the angle α, R^2, and the power law index, β. Top row: systems that are disks by both the α-angle and the power law method. Second row: disks by the α-angle method, but not by the power law method. Third row: disks by the power law method, but not by the α-angle method. Bottom row: disks by neither method.

performance of the α-angle method, we also fit power law functions of the form, $v_\phi(r) = A\,r^{-\beta}$, to the systems in the sample. To fit a power law function, the rotational velocities are averaged in the azimuthal direction, and collected into 10 AU $\times$ 10 AU sized bins to create a cross-section of the disk, similar to the density cross-sections shown in Fig. 4.5. The fitting range is restricted to 20 AU above and below the disk's midplane, and between 50 AU and 150 AU in the radial direction. The inner boundary of 50 AU is chosen to avoid issues related to the spatial resolution of the simulation, while the outer boundary of 150 AU is chosen to avoid fitting beyond the outer edge of as many disks as possible. As a goodness-of-fit parameter we use R^2, which is defined as

$$R^2 \equiv 1 - \frac{SS_{\text{res}}}{SS_{\text{tot}}} = 1 - \frac{\sum_i \left(v_{\phi,i} - f_i\right)^2}{\sum_i \left(v_{\phi,i} - \langle v_\phi \rangle\right)^2},$$

where SS_{res} and SS_{tot} are the squared sum of the residuals, relative to the fit and the mean value respectively. To claim the presence of a Keplerian disk, using the power law method, we require two criteria to be fulfilled: first we ensure that the power law function is a good match to the rotational velocities by requiring that $R^2 > 0.8$; second we require the power law exponent, β, to fall within the range $0.25 \leqslant \beta \leqslant 0.75$.

4.3.3.2 *Comparing methods of disk detection*

Figure 4.5 shows cross sections of some of the systems in the simulation along with scatter plots of the rotational velocities in the disk's midplane. The top row of panels in Fig. 4.5 shows two systems, for which both the α-angle and power law method predict the presence of a disk. The second row of panels shows systems, that are disks by the α-angle method, but not by the power law method. The system in the left panel is rejected because the power law exponent, β, is too steep, while the system in the right panel appears to harbour a $\approx$100 AU sized disk, which is too small to be fitted well by the power law method. The third row of panels shows systems, which are disks by the power law method, but not by the α-angle method. In both these systems it is difficult to identify any structure, recognisable as a disk, from the density cross-sections. The bottom row of panels shows examples of systems that are disks by neither method. Table 4.2 presents a quantitative comparison between the α-angle and power law methods. The two methods agree 82 % of the time, and both methods find disks around approximately half the protostars in the sample.

There is a degree of arbitrariness to the range of β values used by the power law method to detect Keplerian disks. Narrowing the range to $0.4 \leqslant \beta \leqslant 0.6$ decreases the disk fraction from 49 % to 35 %. Thus, even when imposing a more conservative range on the power

Table 4.2: Comparison between the α-angle and the power law methods for disk detection. To claim detection of a disk, using the α-angle method, we require that $0 \leqslant \alpha \leqslant 0.2\,\pi/2$. To claim detection of a Keplerian disk, on scales between 50 AU and 150 AU, using the power law method, we require the power law exponent to fall into the range $0.25 \leqslant \beta \leqslant 0.75$ and $R^2 > 0.8$.

		α-angle method		
		Disk	No disk	
Power law method	Disk	42 %	7 %	**49 %**
	No disk	11 %	40 %	**51 %**
		53 %	**47 %**	

law exponent, more than one third of the systems are still found to have rotation curves consistent with Keplerian rotation. The results presented in this section illustrate that the α-angle method is a robust way of detecting disks in the simulation. Even though the method is not sensitive to the shape of the rotation profile, most of the disks found using this method are consistent with Keplerian rotation. For the remainder of this paper we use the α-angle method for disk detection, and claim the presence of a disk if α falls into the range $0 \leqslant \alpha \leqslant 0.2\,\pi/2$.

4.4 CLASSIFICATION OF PROTOSTARS

Traditionally, YSOs are sorted into four different observationally defined classes: 0, I, II, and III (Lada & Wilking, 1984; Lada, 1987; André et al., 1993). Two widely used tracers for determining the class are the bolometric temperature, T_{bol} (Myers & Ladd, 1993), and the ratio between sub-millimetre and bolometric luminosity, $L_{\mathrm{smm}}/L_{\mathrm{bol}}$ (André et al., 1993), both of which are calculated from the SED

$$
\begin{aligned}
T_{\mathrm{bol}} &= 1.25 \times 10^{-11} \frac{\int_0^\infty \nu S_\nu \, d\nu}{\int_0^\infty S_\nu \, d\nu} \, \mathrm{K} \\
\frac{L_{\mathrm{smm}}}{L_{\mathrm{bol}}} &= \frac{\int_0^{c/350\,\mu\mathrm{m}} S_\nu \, d\nu}{\int_0^\infty S_\nu \, d\nu} .
\end{aligned}
$$

Table 4.3 gives the definition of class boundaries for $L_{\mathrm{smm}}/L_{\mathrm{bol}}$ and T_{bol}.

In the standard picture of star formation (Adams et al., 1987), a star is born in an isolated dense core, which is collapsing under its own gravity. The core eventually dissipates, revealing a pre-main-sequence star encircled by a massive disk. By applying the standard picture, the four observationally defined classes can be interpreted as an evolutionary sequence in which Class 0/I corresponds to a system still

Table 4.3: Definition of class boundaries following André et al. (1993) and Chen et al. (1995). Note, that for L_{smm}/L_{bol} there is no boundary defined between Classes I/II and II/III.

	L_{smm}/L_{bol}	T_{bol}
Class 0	$\geqslant 0.5\,\%$	$< 70\,K$
Class I	$< 0.5\,\%$	$70\,K \leqslant T_{bol} < 650\,K$
Class II	...	$650\,K \leqslant T_{bol} < 2800\,K$
Class III	...	$\geqslant 2800\,K$

embedded within an infalling envelope, with Class 0 being those systems where more than half the mass still resides in the envelope (André et al., 1993).

Although it is generally agreed that the progression through the observationally defined classes roughly correspond to a monotonic progression in time (e.g. Evans et al. 2009), several authors (e.g. Robitaille et al. 2006; Dunham et al. 2010) have pointed out that there is not a one-to-one correspondence between the observationally defined classes and the physical evolution of protostellar systems. For example, in systems which contains a disk, T_{bol} is known to be very sensitive to the orientation of the system relative to the observer. This led Robitaille et al. (2006) to propose a distinction between observationally defined classes and physically defined stages. This distinction is followed here, where systems with $M_\star/M_{env} < 1$ are referred to as Stage 0, and $M_\star/M_{env} > 1$ as Stage I. The mass within a radius of 10 000 AU from the protostar (diameter of 0.1 pc) is used as a proxy of the envelope mass. In this section, we study the classification of protostars, focusing on the performance of T_{bol} and L_{smm}/L_{bol} as evolutionary tracers of embedded protostars.

4.4.1 *Distribution of classes*

Figure 4.6 shows the distribution of T_{bol} and L_{smm}/L_{bol} for the protostars in the simulation, along with real observations. The observations are a conjunction of data from c2d (Evans et al., 2009), the Spitzer Gould Belt survey (GB) (Dunham et al., 2013), and the Herschel Orion Protostar Survey (HOPS) (Fischer et al., 2013; Manoj et al., 2013; Stutz et al., 2013); also see Dunham et al. (2014). The synthetic data in Fig. 4.6 are displayed as a probability density function. The contour levels are chosen so that the contours cover between 90 % and 10 % of the data in steps of 10 %. This way of displaying the data, and the definition of the contour levels, is used throughout the paper.

Generally, the synthetic and observed distributions in Fig. 4.6 agree well with one another. The biggest difference between the two is that

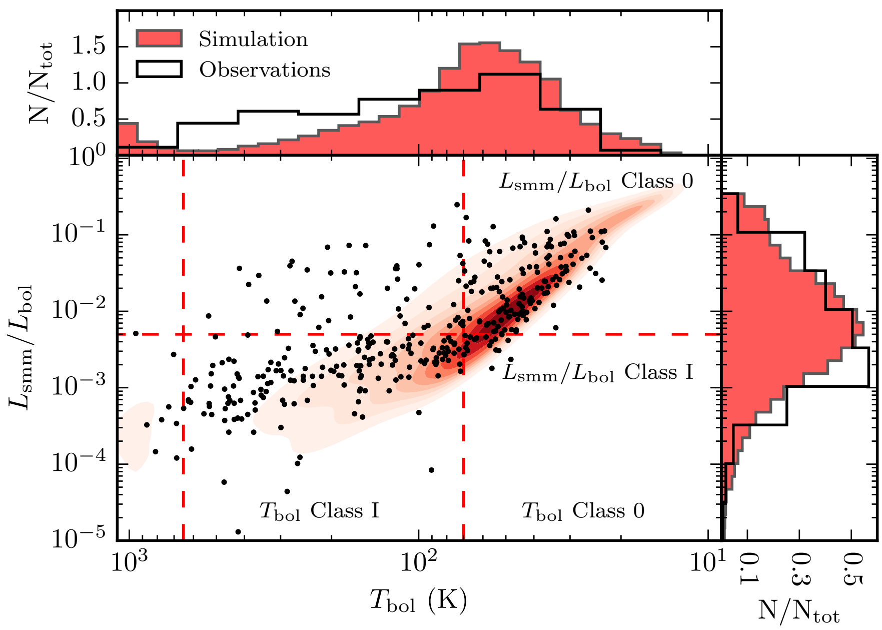

Figure 4.6: Distribution of T_{bol} and L_{smm}/L_{bol}, for the protostars in the simulation (red contours), and from observations (black dots). The contour levels cover 90 %, 80 %, 70 %, ... of the simulated points. The marginal distributions of each variable are shown as histograms at the edges. The observations are a conjunction of data from c2d, GB, and HOPS (see Dunham et al. 2014). Protostars are expected to evolve from upper right to lower left. For the fraction of (synthetic) points recorded in each quadrant see Table 4.4.

the fraction of protostars in the simulation with $T_{bol} \gtrsim 200$ K is significantly reduced relative to the observations. This is a consequence of the spatial resolution in the simulation, which is 8 AU in the best resolved regions. At high densities, such as those found very close to young protostars, this is not enough for the dust to become optically thin to radiation at wavelengths $\lesssim 100$ µm. If the physical extent of the high-density region naturally cover several cells – e.g. a deeply embedded Class 0 source, or the plane of a circumstellar disk – this is no problem. However, in cases where the physical extent of the high-density region is smaller than one cell – e.g. a disk viewed face-on – it effectively makes the protostar look more embedded than it should be. For the types of objects and the wavelengths studied here, this is no concern. To study more evolved objects or shorter wavelengths, higher spatial resolution or a sub-scale model of the central cell around each protostar, is needed.

4.4.2 *Reliability of evolutionary tracers* T_{bol} *and* L_{smm}/L_{bol}

A central question, when dealing with evolutionary tracers, is how well they are able to predict the physical evolution of protostars. A

Table 4.4: Fraction of synthetic data in each class quadrant in Fig. 4.6.

		T_{bol}		
		Class II	Class I	Class 0
L_{smm}/L_{bol}	Class 0	0 %	7 %	48 %
	Class I	5 %	32 %	8 %

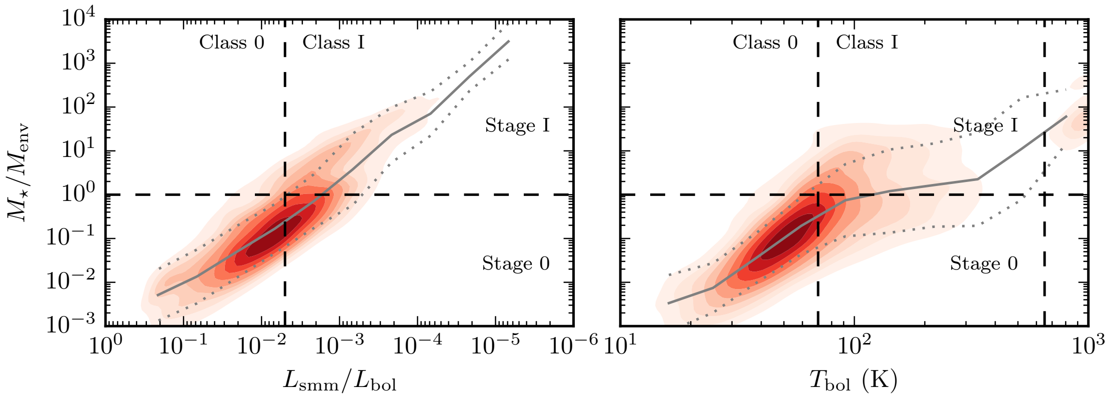

Figure 4.7: L_{smm}/L_{bol} and T_{bol} vs. stage. The grey line is a binned median of the data, and the dotted lines indicate the one sigma uncertainties.

natural first step in answering this question is to determine how often the two agree with each other. Based on the class boundaries, listed in Table 4.3, we find that T_{bol} and L_{smm}/L_{bol} agree on the classification 85 % of the time (see Table 4.4). This is nearly equal to the 84 % agreement reported by Dunham et al. (2014).

Figure 4.7 plots T_{bol} and L_{smm}/L_{bol} vs. stage to study how well the evolutionary tracers agree with the physical stage. The figure shows that L_{smm}/L_{bol} and stage are tightly correlated throughout both the Class 0 and I phases. T_{bol} correlates well with stage during the deeply embedded Class 0 phase, while, in the less embedded Class I phase, it does not. From Fig. 4.7 it can be seen that there is significant cross contamination, especially in the Stage 0/Class I quadrant, however, this is easily explained as a consequence of the simplistic assumption made about the envelope masses. A more careful analysis of the actual masses of protostellar envelopes is beyond the scope of this work, and quantitative predictions about the relationship between the physically defined stages, and observationally defined classes, should therefore be avoided.

L_{smm}/L_{bol} and T_{bol} are designed to quantify the infrared excess of the SED, which depends on the amount of dust surrounding the protostar. Figure 4.8 therefore shows envelope plotted mass against L_{smm}/L_{bol} and T_{bol}. The figure shows that M_{env} does correlate with

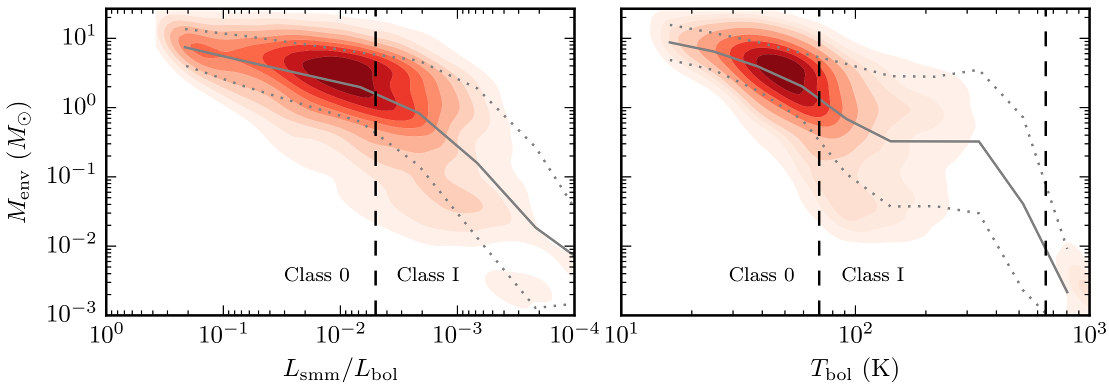

Figure 4.8: Envelope mass vs. L_{smm}/L_{bol} and T_{bol}. The grey line is a binned median of the data, and the dotted lines indicate the one sigma uncertainties.

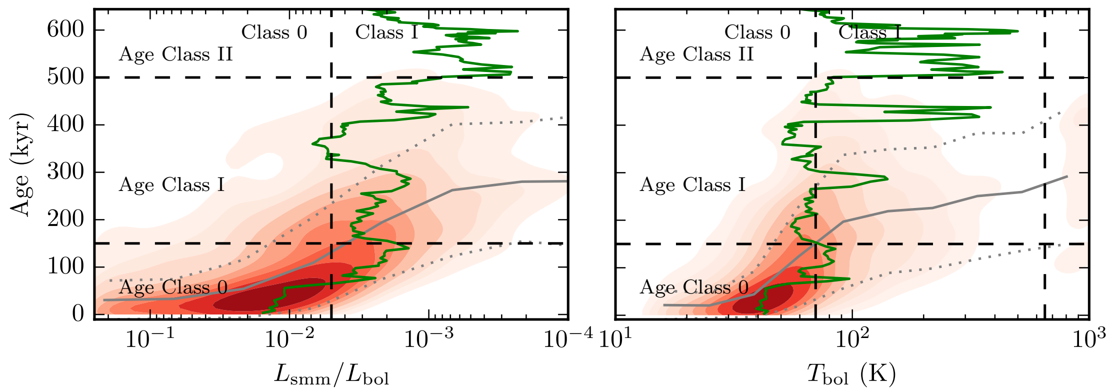

Figure 4.9: L_{smm}/L_{bol} and T_{bol} vs. protostellar age. See Table 4.5 for the fraction of points recorded in each quadrant. The green line shows the evolution of one protostar, which grows to a final mass of $3.6\,M_\odot$. The grey line is a binned median of the data, and the dotted lines indicate the one sigma uncertainties.

L_{smm}/L_{bol} and T_{bol}, but that the correlation is not as strong as with the physical stage in Fig. 4.7.

Finally, it is instructive to study how L_{smm}/L_{bol} and T_{bol} correlate with protostellar age. By counting the number of YSOs in each class, and assuming a Class II lifetime of 2 Myr, the approximate lifetimes of Class 0 and I sources can be estimated to 150 kyr and 350 kyr respectively (Evans et al., 2009; Dunham et al., 2014). The determination of accurate ages for young stars is very difficult (Soderblom et al., 2014), meaning that the assumed Class II age may easily be wrong by a factor of two or more. At the same time, the fraction of YSOs in the different classes differs between individual clouds (Evans et al., 2009), indicating that the local environments also play a role. Figure 4.9 shows protostellar age as function of L_{smm}/L_{bol} and T_{bol}, and Table 4.5 records the fraction of points in each quadrant. For ages

Table 4.5: Fraction of synthetic data in each class quadrant in Fig. 4.9.

		L_{smm}/L_{bol}		
		Class 0	Class I	Class II
Age	Class II	0 %	2 %	...
	Class I	13 %	30 %	...
	Class 0	42 %	13 %	...
		T_{bol}		
		Class 0	Class I	Class II
Age	Class II	0 %	1 %	0 %
	Class I	14 %	25 %	4 %
	Class 0	42 %	13 %	1 %

< 150 kyr, Class 0 protostars (as measured by the SED) outnumber Class I protostars by a factor 3.2 for both L_{smm}/L_{bol} and T_{bol}. For ages between 150 kyr and 500 kyr, the Class I/Class 0 ratio is roughly 2.3. The simulation has not been run for long enough to provide statistical information about systems older than 500 kyr. The results do demonstrate an overall trend, in which older protostars are more likely to be less embedded and vice versa, but the scatter is substantial.

Figure 4.9 also includes an evolutionary track of an example protostar, which grows to a final mass of $3.6\,M_{\odot}$. The track clearly shows that L_{smm}/L_{bol} and T_{bol} are not monotonic functions of time, and that individual protostars may cross the Class 0/I boundary several times during their evolution. Generally, L_{smm}/L_{bol} and T_{bol} are sensitive to changes in the total amount of dust surrounding the protostar, to changes in the distribution of dust in the system, and to changes of the protostellar luminosity. The influence of such effects are studied in the following section. The evolutionary track, shown in Fig. 4.9, show that, at least for individual systems, T_{bol} and L_{smm}/L_{bol} are poor indicators of age.

Overall, the results of the section show that L_{smm}/L_{bol} and T_{bol} agree on the classification most of the time, and that the marginal distributions of T_{bol} and L_{smm}/L_{bol} match the observations well. Apart from the fact that L_{smm}/L_{bol} show a tighter correlation with physical stage throughout both the Class 0 and I phases, relative to T_{bol}, the analysis does not indicate that either tracer has a significant advantage over the other.

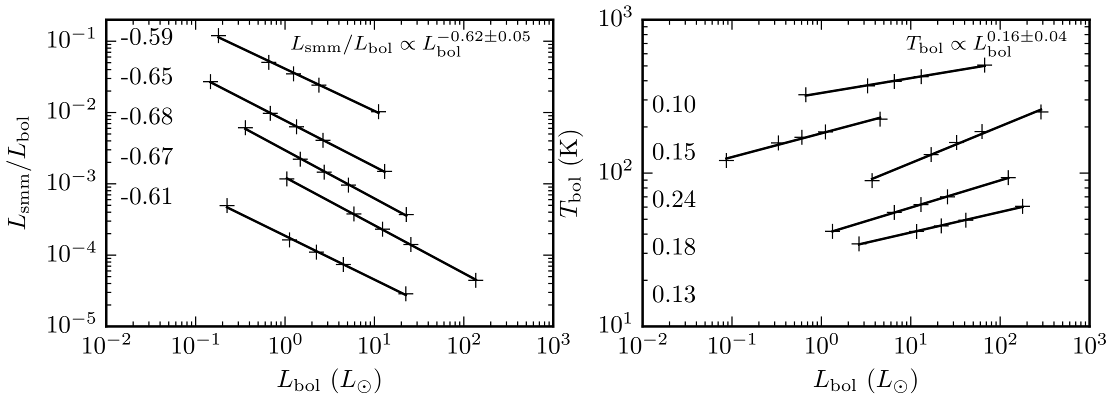

Figure 4.10: Dependence of L_{smm}/L_{bol} and T_{bol} on L_{bol}. The solid lines are power law fits to individual systems, and the numbers indicate the exponents of the fits. The results after fitting all 200 protostars in the sub-sample are shown in the upper right corner. The objects shown in the figure have been chosen to show the dependence on L_{bol} for a wide range of L_{smm}/L_{bol} and T_{bol} values.

4.4.3 *Effective temperature, luminosity and projection effects*

T_{bol} and L_{smm}/L_{bol} are expected to depend on different parameters such as the effective temperature and luminosity of the central protostar, and the orientation of the system relative to the observer. In this section, the influence of these parameters on T_{bol} and L_{smm}/L_{bol} are investigated.

So far, it has been assumed that all protostars in the simulation are perfect black bodies with temperatures of 1000 K. This is clearly unrealistic; however, we find that changing the effective temperature of the central object, while keeping the luminosity constant, do not affect the results. This is because the emission from the protostar is completely reprocessed in the optically thick part of the envelope so that the exact shape of its spectrum becomes irrelevant.

The luminosity of the central protostar, on the other, hand does influence the shape of the observed SED. Luminous protostars heat their surroundings to high temperatures, and high temperature regions in disks and envelopes emit a larger fraction of their light at shorter wavelengths, making luminous protostars appear less embedded. We have extracted a sub-sample of 200 protostars, chosen at random from the original sample, and recalculated their SEDs after multiplying their luminosities by 0.1, 0.5, 2 and 10. Changing the luminosity by a factor of two makes 40 % and 10 % of the protostars cross the Class 0/I boundary for L_{smm}/L_{bol} and T_{bol} respectively. Changing the luminosity by a factor of ten changes these numbers to 60 % and 20 %. In Fig. 4.10 the dependence of L_{smm}/L_{bol} and T_{bol} on luminosity is illustrated for a few objects. The luminosity dependence is fitted well by a power law, and after fitting power laws to all protostars in the sub-sample we find

$$L_{smm}/L_{bol} \propto L_{bol}^{-0.62\pm0.05} \quad \text{and} \quad T_{bol} \propto L_{bol}^{0.16\pm0.04}. \tag{4.1}$$

The results show that L_{smm}/L_{bol} is more sensitive to changes in the luminosity than T_{bol}.

In systems with non-spherical geometry, the orientation of the system relative to the observer, will also affect L_{smm}/L_{bol} and T_{bol}. T_{bol}, in particular, is known to be very sensitive to projection effects, while L_{smm}/L_{bol}, which, contrary to T_{bol} is unaffected by changes in the short wavelength emission, is expected to be less susceptible to changing projection. Probably the most extreme and simultaneously, one of the most common cases in which the orientation of a system relative to the observer is important for protostellar classification, is in case of the presence of a circumstellar disk. A disk viewed edge-on will appear more embedded than the same disk viewed face-on. Using the disk criterion adopted in Sect. 4.3.3, we have calculated edge- and face-on SEDs of more than 8000 disks in the simulation, to test if, and how much, T_{bol} and L_{smm}/L_{bol} are affected. We find, when going from edge- to face-on, that 30 % of the protostars change from Class 0 to I for L_{smm}/L_{bol}, and 50 % for T_{bol}. Knowing that the systems in the simulation generally appear more embedded than they should for T_{bol} (cf. Sect. 4.4.1), we expect this to be a lower limit. L_{smm}/L_{bol} changes its class roughly one time out of three, not because of L_{smm}, which does not depend on the orientation of the system, but because of the measured luminosity, L_{bol}, which, on average, increases by a factor 2.5 when going from edge- to face-on. This is a result of shielding by the dust, which means that a smaller fraction of the light escape through the disk's midplane relative to other directions.

4.5 COMPARING SIMULATIONS AND OBSERVATIONS

4.5.1 *Disks and flux ratios*

The formation of circumstellar disks is a natural consequence of conservation of angular momentum during the core-collapse phase of star formation. Because of contamination from the envelope, direct detection of disks in embedded objects is very challenging, and requires high-resolution and high-sensitivity observations at long wavelengths. For this reason, there is still some uncertainty as to how early circumstellar disks actually form. In recent years, observational studies have demonstrated the presence of Keplerian disks around several Class I protostars (e.g. Brinch et al. 2007b; Lommen et al. 2008; Harsono et al. 2014), while for Class 0 protostars only three unambiguous detections have been reported so far (Tobin et al., 2012; Murillo & Lai, 2013; Lindberg et al., 2014).

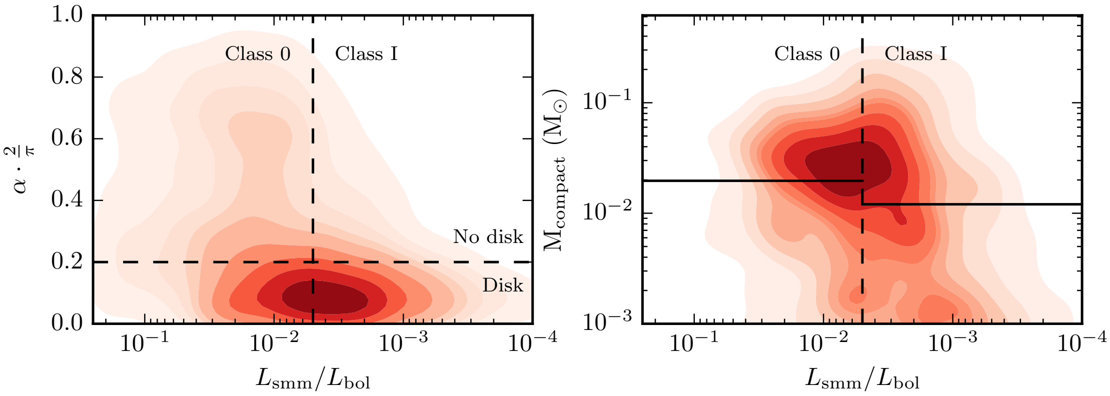

Figure 4.11: Left: α-angle vs. L_{smm}/L_{bol}. Right: compact mass vs. L_{smm}/L_{bol}. The right panel only includes systems with disks ($0 \leqslant \alpha \leqslant 0.2\,\pi/2$). The compact mass may be regarded as an upper limit to the disk mass, since the contribution from the envelope has not been subtracted. The horizontal lines are median masses for the two classes.

Equipped with the α-angle method for disk detection, described in Sect. 4.3.3, we are able to answer fundamental questions about the properties of the disks in the simulation. The left panel of Fig. 4.11 displays the angle α plotted against L_{smm}/L_{bol}, and shows that the majority (74 %) of the Class I systems have values of α in the range $0 \leqslant \alpha \leqslant 0.2\,\pi/2$, indicating the presence of a disk. This is in good agreement with observations, that report a disk fraction $\gtrsim 80\,\%$ in star forming regions younger than 1 Myr (e.g. Wyatt, 2008). The disk fraction in the Class 0 objects is lower because many systems are still dominated by infall, but even so 40 % still have values of α consistent with the presence of a disk.

The right panel of Fig. 4.11, which only includes systems that harbour a disk, shows compact masses vs. L_{smm}/L_{bol}. The "compact mass" is defined as the mass within a radius of 400 AU from the protostar, and thus includes contributions from both the disk and the inner envelope. The compact mass can be regarded as an upper limit to the disk mass, and is used because of difficulties in disentangling disk and envelope masses.

A number of studies have tried to disentangle the dust continuum emission between large-scale envelopes and circumstellar disks (e.g. Looney et al. 2003; Jørgensen et al. 2005a; Eisner et al. 2005; Lommen et al. 2008; Enoch et al. 2011). Jørgensen et al. (2009) studied 10 Class 0 and 10 Class I protostars, using a combination of interferometric and single-dish continuum observations, and developed a framework to interpret these observations based on comparisons with simple dust radiative transfer models. The single-dish observations, presented in Jørgensen et al. (2009), are from the James Clerk Maxwell Telescope, have a wavelength of 850 μm, a resolution of 15″, and were used to measure the combined emission from the disk and envelope. The interferometric observations are from the SMA, have a wavelength of $1100\,\mu m$, flux extracted at a baseline length of $50\,k\lambda$ (corresponding to a resolution of $\approx 4''$), and were used to probe the disk emission, while resolving out the contribution from the envelope. Assuming optically thin dust, the compact interferometric flux, $S_{50\,k\lambda}$, can be assumed to be directly proportional to the disk mass, while the extended single-dish flux, $S_{15''}$, can be assumed to be proportional to the combined disk and envelope mass.

In recreating the continuum observations described above, we have assumed a source distance of $150\,pc$, and rescale the observd fluxes of Jørgensen et al. (2009) to match this distance. We have checked that the results presented in the following are not altered by changing the assumed distance to $220\,pc$, which is the distance to most of the observed objects in Jørgensen et al. (2009). We assume a detection threshold of $0.15\,Jy\,beam^{-1}$ for the synthetic single-dish observations (Kirk et al., 2006), and $10\,mJy$ for the interferometric observations. Jørgensen et al. (2009) converted their fluxes into disk and envelope masses, but, in order to make as few assumptions as possible, only the fluxes are compared here.

The top row of panels in Fig. 4.12 shows compact and extended flux, $S_{50\,k\lambda}$ and $S_{15''}$, plotted against T_{bol}. The synthetic compact fluxes are, on average, smaller by a factor of ~6 relative to the observations; the synthetic extended fluxes are likewise, on average, smaller relative to the the observations by a factor of ~2. Adding the missing interferometric flux to the single-dish flux, brings it into agreement with the observations, showing that the reduced synthetic flux can be explained by the lack of compact emission alone. The lack of compact emission is likely due to the spatial resolution in the simulation not being sufficiently high to avoid numerical dissipation at the small spatial scales relevant for disks. Specifically, the numerical viscosity is artificially high on small scales leading to rapid accretion of material onto the protostar, which would have otherwise remained in the disk. This also means that the disk masses can be expected to be underestimated by the same factor.

The bottom left panel of Fig. 4.12 shows the ratios between compact and extended fluxes. Assuming a spherical envelope model with $\rho \propto r^{-1.5}$, Jørgensen et al. (2009) calculated that pure envelope emission is expected to yield a flux ratio $S_{50\,k\lambda}/S_{15''} = 0.04$, shown by the horizontal dashed line in the figure. A ratio above this value indicates the presence of an unresolved massive component, such as a disk. All but one of the systems presented in Jørgensen et al. (2009) have a flux ratio consistent with the presence of a disk. Based on the discussion above, we expect the synthetic flux ratios to be smaller relative to the real ones with a factor ~3, which is also seen to be the case.

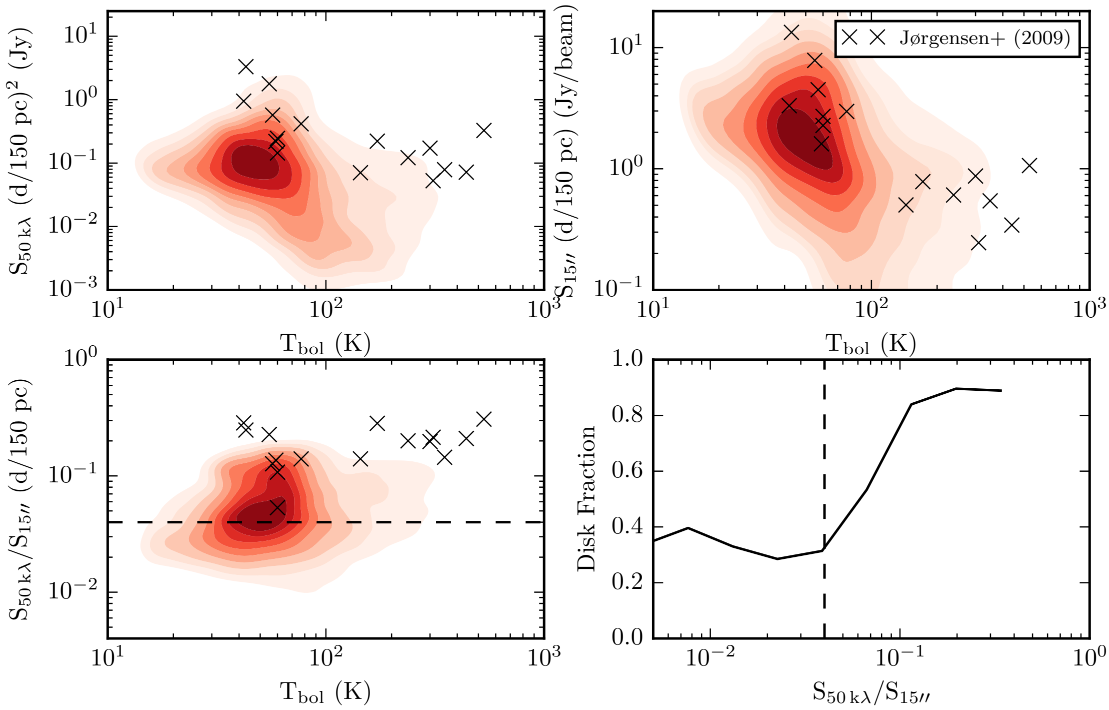

Figure 4.12: Top left: compact fluxes from the simulation compared directly to 1.1 mm SMA observations. Top Right: extended fluxes from the simulation compared directly to 0.85 mm SCUBA observations. The fluxes have been rescaled to a common distance of 150 pc. For the interferometric fluxes this is just the inverse square law $F \propto d^{-2}$. For the single-dish fluxes we follow Jørgensen et al. (2009) who, based on a density profile corresponding to a free-falling envelope ($\rho \propto r^{-1.5}$), found $F \propto d^{-1}$. Bottom left: flux ratios. The horizontal dashed line corresponds to the flux ratio expected for pure envelope emission (Jørgensen et al., 2009). Bottom right: disk fraction vs. flux ratio. The solid line is the fraction of systems which contains a disk in each bin. The vertical dashed line is the same as the horizontal dashed line in the lower left panel.

A central hypothesis of Jørgensen et al. (2009) is that the flux ratio, between compact and extended emission, can be used as a tracer of disk occurrence. To test this hypothesis, the disk fraction has been plotted as function of flux ratio in the bottom right panel of Fig 4.12. The disk fraction is defined as the number systems containing a disk, divided by the total number of systems in each bin. The solid line in the figure is the disk fraction, and the dashed line indicates the limit of pure envelope emission. The disk fraction is roughly constant at ≈30 %, with perhaps a shallow negative slope, up to a flux ratio of approximately 0.05, above which is begins to climb rapidly. For flux ratios below 0.05 the total fraction of systems that contain a disk is 33 %, while, for flux ratios above 0.05, the fraction is 76 %.

Because of the missing material on small scales, the flux ratios, measured from the synthetic observables, are systematically reduced relative to the observations. This precludes any quantitative comparison between observed and simulated flux ratios, since the uncertainties related to the small-scale physics in the simulation are considerable. Qualitatively, the results do demonstrate that a protostar is more likely to be encircled by a disk at higher flux ratios, supporting the hypothesis of Jørgensen et al. (2009).

4.5.2 *The protostellar luminosity function*

The observed PLF is a roughly log-normal distribution, spanning more than three orders of magnitude, with a median luminosity of $\approx 1.3\,L_\odot$ (Evans et al., 2009; Dunham et al., 2013, 2014). A long-standing issue in low-mass star formation is the so-called "luminosity problem", where young stars are under-luminous with respect to expectations from simple physical models. The gravitational collapse of a spherical core, for example, yields an expected accretion rate, of $\sim 10^{-5}\,M_\odot\,yr^{-1}$, which corresponds to $L_{acc} \sim 30\,L_\odot$, assuming a stellar mass of $0.25\,M_\odot$ and radius of $2.5\,R_\odot$; more than a factor of ten above the observed median.

The luminosity problem was first noticed by Kenyon et al. (1990) who, as a possible solution suggested, that material accrete onto the protostar in short high-intensity bursts, giving rise to an episodic accretion paradigm. Observational evidence for episodic accretion include the FU Orionis objects, which are pre-main-sequence stars undergoing accretion bursts raising their observed luminosity to $\sim 100\,L_\odot$ (see Audard et al. 2014 for a recent review). Recently, Jørgensen et al. (2013) showed how water, left in the gas phase after an accretion burst, can explain the lack of HCO^+ around the deeply embedded protostar IRAS 15398–3359, thereby illustrating the potential of using chemical signatures as a tracer of episodic accretion.

Episodic accretion events, induced by disk instabilities, have been used with some success to reconcile models and observations (e.g.

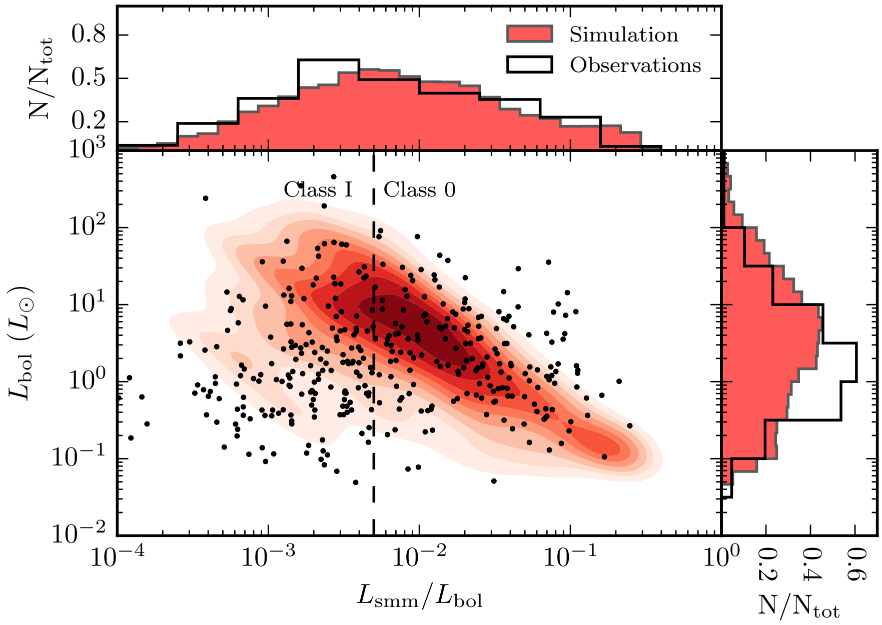

Figure 4.13: Distribution of L_{bol} and L_{smm}/L_{bol}, for the protostars in the simulation (red contours), and observations (black dots). The marginal distributions of each variable are shown at the edges. The observational data is the same, as was used in Fig. 4.6. Median luminosities of both simulation and observations are recorded in Table 4.6.

Dunham & Vorobyov 2012). In a recent paper Padoan et al. (2014) – using a simulation similar to the one analysed here, but with lower spatial resolution, smaller box-size, and covering a longer time-span – argued for a different paradigm in which accretion rates are regulated by turbulence induced variations in the large-scale mass infall from the envelope and onto the disk/star system.

Figure 4.13 plots L_{bol} against L_{smm}/L_{bol} in a fashion similar to the "BLT" diagrams first introduced by Myers & Ladd (1993), but with L_{smm}/L_{bol} replacing T_{bol} as an evolutionary tracer. Table 4.6 records the median luminosities of the protostars in the simulation, as well as in the observations. The observational data are the same conjunction

Table 4.6: Median luminosities from observations and simulation. The first row is the observed luminosities of the combined c2d+GB+HOPS data (Dunham et al., 2014). The second row records the luminosities from the simulation.

	Class 0	Class I	All
Observations	1.9 $L_\odot$	1.4 $L_\odot$	1.7 $L_\odot$
Simulation	2.1 $L_\odot$	5.4 $L_\odot$	3.3 $L_\odot$

of c2d, GB, and HOPS data, that were used to study the distribution of T_{bol} and L_{smm}/L_{bol} in Sect. 4.4.1. The simulated luminosities are, on average, a factor of two larger than the observed luminosities. However, the spread of the observed luminosities, spanning more than three orders of magnitude, is reproduced well by the simulation.

There is a natural difference between the inferred bolometric luminosity of any given source, measured by integrating over its SED, and its internal luminosity – depending, for example, on the viewing angle towards sources where the surrounding dust is very asymmetrically distributed. Direct tests, comparing the bolometric and internal luminosities of the protostars in the simulation, reveal that the widths of their distributions are similar, with the median of the internal luminosity distribution being enhanced by a factor of 1.3 relative to the bolometric distribution.

The median luminosities of the Class 0 and I protostars in the simulation are $2.1\,L_\odot$ and $5.4\,L_\odot$ respectively. For the Class 0 protostars this is close to the observed median of $1.9\,L_\odot$, while, for the Class I protostars, the simulated luminosities are enhanced by a factor ~5 relative to the observations. Looking at Fig. 4.13, observations and simulation agree well with one another, with the upper envelope of the simulated points following the relationship between L_{smm}/L_{bol} and L_{bol} given in Eq. (4.1). The upper envelope of the real observations follow the same relationship except for ~15 very embedded protostars at the Class 0 end, that are seen to fall above it. At the Class I end of the figure the observations show a high density of observed systems at luminosities between $\sim 0.1\,L_\odot$ and $\sim 5\,L_\odot$, that are not present to the same extent in the simulation. We believe this to be the objects that have evolved past their most embedded phase, and are lost in the simulation due to loss of spatial resolution (cf. discussion in Sect. 4.2.2). We also believe that the lack of these objects explain, why the median luminosity of the Class I protostars in the simulation, as well as the sample as a whole, is larger than the observed values.

4.5.3 *Association between protostellar cores and protostars*

One of the fundamental question in star formation is how protostars accrete their mass. In the standard picture of low-mass star formation (Adams et al., 1987), stars are born in dense molecular cloud cores, which also act as a mass reservoir for the protostars. In reality, most protostars are born in clusters, where dynamical interactions with other protostars may turn the process into a much more chaotic one. One of the questions in this area has been whether protostars stay in the dense environments, where they are born, throughout the main accretion phase, or if the situation is much more dynamic, where the motion of the protostars through the ambient medium, and the combined effect of the differential forces impacted by the turbulent ram pressure and the magnetic fields on the core compared to the protostar, is important for the accretion histories of protostars.

The relationship between cores and protostars has been studied in several of the nearby molecular clouds (Hartmann, 2002; Jørgensen et al., 2007b, 2008; Enoch et al., 2008). These studies all conclude that, on average, the embedded protostars do not migrate far away from the dense cores where they were born. This finding stands in contrast to some numerical simulations, such as Bate (2012), who found that the motion of protostars through the ambient medium plays a significant role for the accretion histories.

In this section, we study the protostellar cores in the simulation, with special focus on their association with embedded protostars. We compare our results to those of Jørgensen et al. (2008), who studied the properties of cores and protostars in the Ophiuchus and Perseus molecular clouds by utilising a combination of 850 μm SCUBA continuum images and mid-infrared Spitzer data. To this end, we have created synthetic 850 μm continuum images of all the protostars in the simulation, which are used to detect and characterise the protostellar cores. The method used for detecting cores in the simulation was described in Sect. 4.3.2. Jørgensen et al. (2008) used mid-infrared Spitzer observations to characterise and detect the positions of the observed protostars. These observations are not recreated, and the known positions of the protostars from the simulation are used instead. A normally distributed uncertainty, with FWHM of 7″, is added to the positions of the protostars to emulate the uncertainty due to the size of the Spitzer beam, and pointing uncertainty in the submm observations. We follow Jørgensen et al. (2008) and adopt a distance of 125 pc to Ophiuchus, and 250 pc to Perseus.

The number of detected cores varies depending on the assumed distance to the cloud. At a distance 125 pc, we find a total of 177 cores in the simulation, while at 250 pc we find 96 (last snapshot only). The decrease in the number of cores is partly a result of the less luminous cores no longer being detected at larger distances, partly due to the lower resolution of the maps, which serves to merge some cores. Nevertheless, many of the results presented below are independent on the assumed distance.

As discussed in Sect. 4.3.1, Class 0 and I protostars are found to be closely associated with regions in the cloud of high column density, both in nature (Evans et al., 2009) and in the simulation. Jørgensen et al. (2008) analysed the association between cores and protostars quantitatively by calculating the distance distribution between the two in Ophiuchus and Perseus. We repeat this analysis for the cores and protostars in the simulation, and plot the results in Fig. 4.14, which shows the distance distribution between cores and protostars in the simulation and in the observations of Jørgensen et al. (2008). The observed and synthesised distributions are seen to be very similar

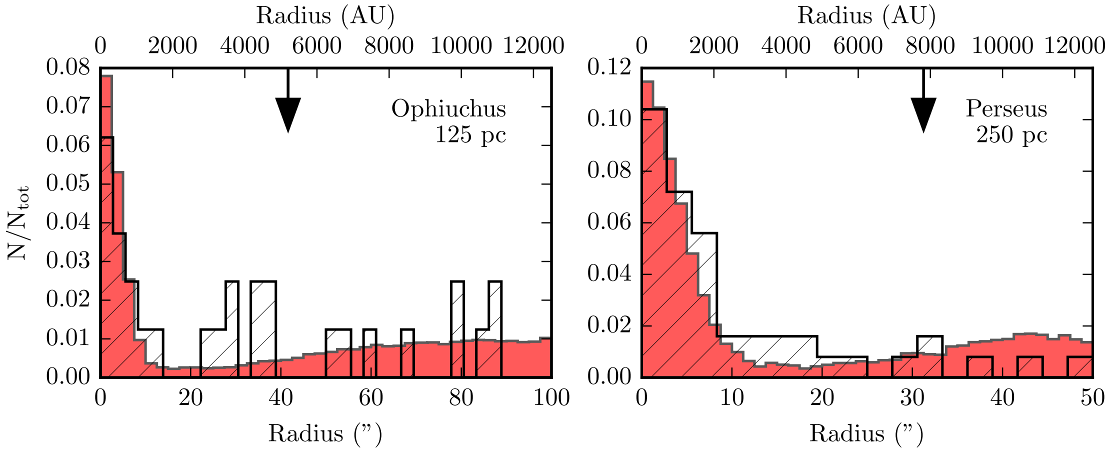

Figure 4.14: Distribution of distances between cores and their nearest protostar in the simulation (shaded histograms), and from observations of Ophiuchus and Perseus (hatched histograms). The black arrows indicate the average core radius in the simulation.

– applying a two-sample Kolmogorov-Smirnov test yields p-values of 0.6 and 0.1 for Ophiuchus and Perseus respectively – both of them peaking at small distances, confirming the close association between cores and protostars.

The distance distribution is slightly different between Class 0 and I protostars. Class 0 protostars are very narrowly distributed around the core centres, while the distribution of Class I protostars is somewhat wider, although still centrally peaked. 90 % of all Class 0 protostars lie within one core radius from their nearest core, while the same is true for 70 % of the Class I protostars. This is hardly surprising since Class 0 protostars are, by definition, deeply embedded objects, associated with high-density regions. For the distances corresponding to both Ophiuchus and Perseus, we find that ≈60 % of the embedded protostars in the simulation lie within 15″ of the nearest core. In comparison, Jørgensen et al. (2008) find that 47 % of the embedded protostars in Ophiuchus and 58 % in Perseus lie within 15″ of their nearest core, and simulation and observations are thus in good agreement with each other.

From Figs. 4.14 and 4.1 we see that some cores are protostellar (contains a protostar) while others are starless. Assuming a distance of 125 pc we find that 16 % of the cores are protostellar, while, for a distance of 250 pc, the fraction is 24 %. Protostellar cores are, on average, more luminous than starless cores due to the presence of an internal source of luminosity. It is therefore also not surprising that the fraction increases with distance, since a lot of the starless cores are not luminous enough to be detected at the larger distance. For comparison, Jørgensen et al. found 35 % the cores in Ophiuchus to be protostellar, and 58 % in Perseus.

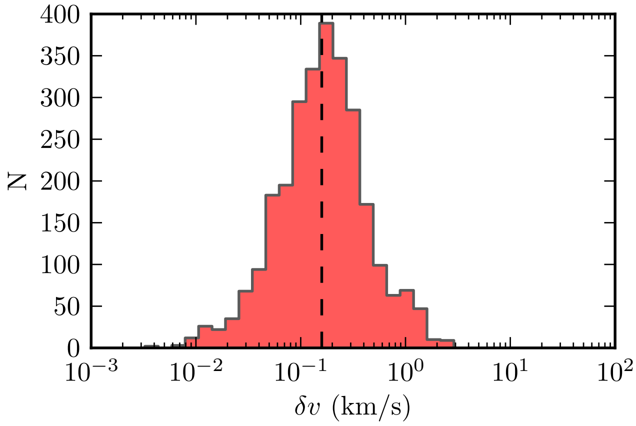

Figure 4.15: Distribution of protostellar velocities relative to the gas and dust within a distance of 5000 AU from the protostar. Only objects with no other protostars close by are included. The dashed line indicate the median value of the distribution.

Both Hartmann (2002) and Jørgensen et al. (2007b) used the close association found between cores and protostars to argue that the velocity dispersion of protostars relative to cores is very small. Based on the distribution of protostars around filaments, and assuming a stellar age of 2 Myr, Hartmann (2002) estimated an upper limit on the velocity dispersion in Taurus of $\approx 0.2\,\mathrm{km\,s^{-1}}$. Using an analysis like the one shown in Fig. 4.14, and assuming protostellar age of 0.1 Myr, Jørgensen et al. (2007b) estimated a velocity dispersion of $\approx 0.1\,\mathrm{km\,s^{-1}}$ in Perseus. These estimates can be tested by measuring the two-dimensional velocity distribution, of the protostars in the simulation, relative to the dust and gas in their immediate vicinity. To avoid uncertainties due to dynamical interactions, we have only included embedded protostars with no other protostars within a radius of 5000 AU. We also exclude protostars that have previously interacted dynamically with other protostars. The resulting distribution is shown in Fig. 4.15 and is seen to be roughly log-normal with a median velocity dispersion, δv, of $\approx 0.15\,\mathrm{km\,s^{-1}}$. 60 % of the protostars have a $\delta v < 0.2\,\mathrm{km\,s^{-1}}$, and 90 % have $\delta v < 0.5\,\mathrm{km\,s^{-1}}$. A manual inspection of the remaining protostars, with $\delta v > 0.5\,\mathrm{km\,s^{-1}}$, reveals that most are either subjects to dynamical interactions with the large cluster seen in Fig. 4.1, which is massive enough to interact with protostars even if no other protostars are present within 5000 AU, or they are passing through regions where the gas has several velocity components.

4.6 SUMMARY

This paper has presented an analysis of synthetic continuum images and SEDs, created from a large $5\,\text{pc} \times 5\,\text{pc} \times 5\,\text{pc}$ MHD simulation of a molecular cloud. Over the course of 0.76 Myr the simulation forms more than 500 protostars, primarily within two sub-clusters. Having created more than 13 000 unique radiative transfer models from the simulation, we have had access to an unprecedentedly large sample of synthetic observations, which have been compared to a number of observational studies. The main results of the paper are summarised as follows

1. The simulation reproduces an extinction/column density threshold for cores, similar to that seen in observations (e.g. Johnstone et al. 2004; Enoch et al. 2007). Because the simulation is ideal MHD the threshold cannot be explained by the presence of photoionising radiation (McKee, 1989). An alternative explanation is that the cores are a product of Jeans fragmentation and therefore primarily appear in the densest regions of the cloud (Larson, 1985).

2. Values of the evolutionary tracers T_{bol} and L_{smm}/L_{bol} are calculated for all the SEDs in the sample. We find that the agreement between observed and synthetic distributions of T_{bol} and L_{smm}/L_{bol} is excellent, and that the two tracers agree on the classification of Class 0 and I protostars 85 % of the time, which is similar to the 84 % agreement recorded from observations (Dunham et al., 2014). L_{smm}/L_{bol} correlates strongly with the physically defined stage over the entirety of its range. The same is true for T_{bol} in the Class 0 phase, but not in the Class I phase. Neither tracer correlates well with age, showing that T_{bol} and L_{smm}/L_{bol} are poor indicators of this.

3. Both T_{bol} and L_{smm}/L_{bol} depend on parameters such as protostellar luminosity and the projection of the system relative to the observer. For individual sources the luminosity dependence is fitted well by a power law. We show that L_{smm}/L_{bol} is more sensitive to changes in the luminosity, while T_{bol}, on the other hand, is more susceptible to projection effects.

4. We devise a novel method for detecting disks in the simulation (the α-angle method) based on the ratio between the radial and rotational motions of the gas around a protostar. This method, is found to be a simple, yet robust, way determining if a system contains a disk or not. Values of α lying within the range $0 \leqslant \alpha \leqslant 0.2\,\pi/2$ are found empirically to indicate the presence of a disk. Power law fits to the rotation profiles show, that the disks found with the α-angle method are consistent with Keplerian

rotation 80 % of the time. The remaining 20 % are expected to be other kinds of rotationally dominated structures, for example, magnetically supported pseudodisks.

5. Disks are found to form early on in the simulation, with one being found around 40 % of the Class 0 protostars. For the Class I protostars this fraction increases to 74 %.

6. Synthetic flux emission from the innermost regions around the protostars are found to be a factor of ~6 too low relative to the observations of Jørgensen et al. (2009). The extended fluxes ares likewise found to be too small by a factor ~2. The missing flux is likely a result of numerical effects on the small spatial scales in the simulation, where high numerical viscosity may cause material, that would have otherwise remained in the disk, to accrete onto the protostar.

7. Jørgensen et al. (2009) used the flux ratio between compact and extended fluxes as an indicator of the presence of disks. In the simulation, we find that the disk fraction does increase with flux ratio; 33 % of the systems in the simulation, with a flux ratio, $S_{50\,k\lambda}/S_{15''} < 0.05$, contain a disk, while the fraction increases to 76 % for ratios >0.05.

8. The observed PLF is a wide distribution, spanning more than three orders of magnitude, with a median luminosity of $\approx 1.7\,L_\odot$. The bolometric luminosities, of the protostars in the simulation, reproduce the spread of the observed PLF, while the median is enhanced by a factor of two relative to observations. We believe the difference between the observed and simulated PLF is due to the simulated sample not being complete for Class I sources.

9. We find that protostars and cores are closely associated with one another, and that the distribution of distances between them is in excellent agreement with observations from Perseus and Ophiuchus. The relative velocity distribution between protostars, and the gas in their immediate surrounding, is roughly log-normal with a median of $0.15\,\mathrm{km\,s^{-1}}$. Excluding dynamical interactions, protostars are, on average, not expected to migrate far away from the regions where they were born.

Some weaknesses of the simulation have been illuminated during the work presented here. Most notably, the refinement criteria for the code should be adapted to depend on more parameters than local density, to make it possible to follow the protostellar evolution all the way to the Class II phase. Other improvements, which will help obviating some of these weaknesses are the inclusion of sub-grid models for the inner-most cells, to deal with the resolution issue when doing radiative transfer, and stellar models for the protostars to accurately predict the luminosity.

Naturally, the ultimate goal is to understand the underlying physics of the star-formation processes, and thus also the assumptions in different flavours of simulations. The simulation includes the main ingredients to describe star formation in a piece of a molecular cloud: self-gravity, magnetic fields, driven turbulence, and sink particles. An important improvement will be to go beyond an isothermal equation of state, and to include ionising and non-ionising radiative feedback from the protostars, and cooling and heating processes. This is especially needed for a proper description of the interstellar medium near more massive stars. The spatial resolution of the simulation analysed in this paper is at the limits of what is currently computationally doable, but going to even higher physical resolutions, below 1 AU, will be needed to account for some of the feedback from the protostars, and to resolve smaller disks around more evolved protostars.

With this paper, it has been demonstrated how direct comparison between observations and simulations is a very powerful tool, both in terms of interpreting observations, and in terms of testing different types of simulations to see how well they are able to reproduce observational results. This approach goes beyond comparing single selected objects with isolated models of star-forming cores and allow for statistical comparisons with observational surveys.

4.7 ACKNOWLEDGEMENTS

The authors acknowledge Michael Dunham and the HOPS team for providing the observational data used in Figs. 4.6 and 4.13. We thank Christian Brinch, Michael Dunham, Åke Nordund, and Paolo Padoan for helpful discussions. We also thank the anonymous referee for providing helpful comments, which significantly improved the quality of the paper. This research was supported by a Lundbeck Foundation Group Leader Fellowship to JKJ as well as the European Research Council (ERC) under the European Union's Horizon 2020 research and innovation programme (grant agreement No 646908) through ERC Consolidator Grant "S4F". TH is supported by a Sapere Aude Starting Grant from the Danish Council for Independent Research. Research at Centre for Star and Planet Formation is funded by the Danish National Research Foundation. We acknowledge PRACE for awarding us access to the computing resource JUQUEEN based in Germany at Forschungszentrum Jülich for carrying out the simulation. Archival storage and computing nodes at the University of Copenhagen HPC center, funded with a research grant (VKR023406) from Villum Fonden, were used for the post-processing.

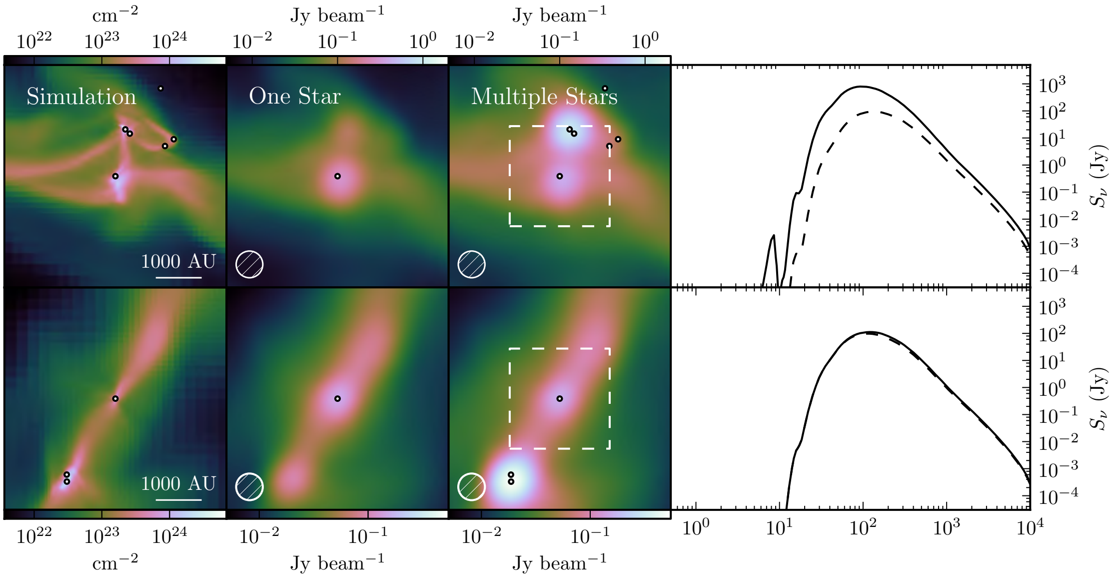

Figure 4.16: Two examples illustrating the effects of including multiple source of luminosity in the RADMC-3D models. From left to right: projected gas column density, with dots indicating protostars; 1100 μm RADMC-3D continuum images with only one source of luminosity; same continuum image, but with multiple sources of luminosity; SEDs of the systems, where the single-luminosity SED is indicated by the dashed line and the multiple-luminosity SED by the solid line. We have assumed a distance of 150 pc to the systems, and the continuum images have been convolved with a 4″ beam. The white dashed box in the images show the size and shape of the aperture over which the flux is integrated to calculate the SEDs. Selected physical parameters and observables of the central protostars in the two examples are presented in Table 4.7.

4.8 APPENDIX A: INCLUSION OF MULTIPLE SOURCES OF LUMINOSITY

This appendix investigates the effects on the synthetic continuum images and SEDs of including multiple sources of luminosity in the RADMC-3D models. The discussion is based on the two examples shown in Fig. 4.16.

The first example, shown at the top of Fig. 4.16, is a system consisting of six protostars. The central protostar has a luminosity of 2.3 L_{bol} and an age of 15.3 kyr. Four of the five remaining protostars in the cutout have luminosities < 0.2 L_{bol}, while the fifth protostar, which lies at a distance of 1100 AU from the central protostar, has a luminosity of 29.7 L_{bol}. Table 4.7 records selected physical parameters and observables of the system, for both one and multiple sources of luminosity. The methods used for obtaining the observables have not been adjusted to take into account that there are more source of luminosity in

Table 4.7: Selected physical parameters and observables of the central protostars shown in Fig. 4.16.

	$M_\star$ ($M_\odot$)	Age (kyr)	L_{bol} ($L_\odot$)	T_{bol} (K)	L_{smm}/L_{bol} (%)	$S_{50\,k\lambda\,1.1\,mm}$ (mJy)	$S_{4'',\,1.1\,mm}$ (mJy beam^{-1})	$S_{15'',\,0.85\,mm}$ (Jy beam^{-1})
Top example from Fig. 4.16								
One lum. source	0.08	15.3	2.3	39	2.3	92	265	2.37
Multiple luminosity sources			24.5	51	0.7	550	377	5.49
Bottom example from Fig. 4.16								
One luminosity source	0.25	43.2	2.8	46	1.3	53	150	1.60
Multiple luminosity sources			3.0	44	1.4	161	156	2.03

the models, but are the same as used in the main paper. The luminous protostar falls inside the aperture used for calculating the SED, which is consequently affected significantly. This has adverse effects on both the measured luminosity as well as $L_{\rm smm}/L_{\rm bol}$. The measured fluxes, both interferometric and single-dish, are also affected by the addition of multiple luminosity sources. The interferometric flux, $S_{50\,{\rm k}\lambda\,1.1\,{\rm mm}}$, is particularly affected since the method used to extract this flux is not sensitive to the location of the flux emission, but only the magnitude. With only one source of luminosity per model this approach poses no problem, but naturally overestimates the flux when multiple sources are included. The single-dish fluxes are also affected – the images in Fig. 4.16 have been convolved with a $4''$ beam, which is seen to be a good enough resolution to separate the emission from central protostar from its more luminous countarpart. Still, $S_{4'',\,1.1\,{\rm mm}}$, increases with a factor of 1.4 when going from one to multiple sources of luminosity. For the larger beam, $S_{15'',\,0.85\,{\rm mm}}$, the situation is worse because the the two sources can no longer be separated.

The second example, shown at the bottom of Fig. 4.16, is a system consisting of three protostars. The central protostar has a luminosity of $2.8\,L_{\odot}$, and the most luminous of the two remaining stars, which is at a distance of 2100 AU from the central protostar, has a luminosity of $7.9\,L_{\odot}$. The final protostar in the system has a luminosity $<0.1\,L_{\odot}$. The observables in this example are somewhat less affected by the inclusion of multiple sources of luminosity, partly because the distance to the neighbouring protostars is larger relative to the first example, partly because the additional sources of luminosities are order of magnitude brighter than the central protostar. This also means that the SED and $S_{4'',\,1.1\,{\rm mm}}$ are unaffected, while the interferometric flux and $S_{15'',\,0.85\,{\rm mm}}$ continue to be affected.

The analysis of the two examples show that the effects of introducing more than one source of luminosity into the models can have quite adverse effects on the observables. When analysing real observations, it is typically possible to extract the signal from the source one is interested in, while filtering away the signal from other nearby sources. Such work is often done on an object-by-object basis and may include the application of custom apertures, flagging part of the data, and subtracting the signal one is not interested in. It is, in principle, possible to do the same for the synthetic observations, but it is not feasible due to the vast number of models, which is why we decided on doing a simple pipeline analysis, made possible by only including one source of luminosity per model.

5

PAPER II: PROTOSTELLAR ACCRETION TRACED WITH CHEMISTRY. COMPARING SYNTHETIC $C^{18}O$ MAPS OF EMBEDDED PROTOSTARS TO REAL OBSERVATIONS

Søren Frimann[1], Jes K. Jørgensen[1], Paolo Padoan[2], and Troels Haugbølle[1]

[1] Centre for Star and Planet Formation, Niels Bohr Institute and Natural History Museum of Denmark, University of Copenhagen, Øster Voldgade 5-7, DK-1350 Copenhagen K, Denmark
[2] ICREA and Institut de Ciències del Cosmos, Universitat de Barcelona, IEEC-UB, Martí Franquès 1, E-08028 Barcelona, Spain

Appeared in *Astronomy & Astrophysics*, vol. 587, article no. A60, March 2016

ABSTRACT

Context. Understanding how protostars accrete their mass is a central question of star formation. One aspect of this is trying to understand whether the time evolution of accretion rates in deeply embedded objects is best characterised by a smooth decline from early to late stages or by intermittent bursts of high accretion.

Aims. We create synthetic observations of deeply embedded protostars in a large numerical simulation of a molecular cloud, which are compared directly to real observations. The goal is to compare episodic accretion events in the simulation to observations and to test the methodology used for analysing the observations.

Methods. Simple freeze-out and sublimation chemistry is added to the simulation, and synthetic $C^{18}O$ line cubes are created for a large number of simulated protostars. The spatial extent of $C^{18}O$ is measured for the simulated protostars and compared directly to a sample of 16 deeply embedded protostars observed with the Submillimeter Array. If CO is distributed over a larger area than predicted based on the protostellar luminosity, it may indicate that the luminosity has been higher in the past and that CO is still in the process of refreezing.

Results. Approximately 1 % of the protostars in the simulation show extended $C^{18}O$ emission, as opposed to approximately 50 % in the observations, indicating that the magnitude and frequency of episodic accretion events in the simulation is too low relative to observations. The protostellar accretion rates in the simulation are primarily modulated by infall from the larger scales of the molecular cloud, and do not include any disk physics. The discrepancy between simulation and observations is taken as support for the necessity of disks, even in deeply embedded objects, to produce episodic accretion events of sufficient frequency and amplitude.

5.1 INTRODUCTION

A protostar obtains most of its mass during the early embedded stages, where it is surrounded by large amounts of dust and gas. At this stage the protostellar luminosity is dominated by the release of gravitational energy due to accretion onto the central object. Numerous large-scale surveys (e.g. Evans et al. 2009; Kryukova et al. 2012; Dunham et al. 2013) have shown that the distribution of protostellar luminosities (the Protostellar Luminosity Function, PLF) is a wide distribution, spanning more than three orders of magnitude, with a median luminosity of $1\,L_\odot$–$2\,L_\odot$. To form a solar mass star within the duration of the embedded stage of ~0.5 Myr (Evans et al., 2009), an average accretion rate of $2 \times 10^{-6}\,M_\odot\,yr^{-1}$ is needed. Assuming a protostellar mass and radius of $0.5\,M_\odot$ and $2.5\,R_\odot$, this implies an accretion luminosity of $\sim 10\,L_\odot$, which is an order of magnitude above the observed median. The situation is further aggravated by the fact that other sources of luminosity, such as deuterium burning and Kelvin-Helmholtz contraction, also have to be taken into consideration.

The inability of simple physical arguments to accurately predict the observed PLF is known as the luminosity problem and was first noticed by Kenyon et al. (1990). Since its discovery more than two decades ago much work has gone into reconciling theory and observations; the problem has been approached through both analytical modelling (e.g. Dunham et al. 2010; Offner & McKee 2011; Myers 2012) and numerical simulations (e.g. Dunham & Vorobyov 2012; Padoan et al. 2014). A variety of different accretion scenarios, which can reproduce both spread and median of the observed PLF, have been presented, indicating that reproduction of the PLF alone is not sufficient to discriminate between different accretion scenarios.

The preferred scenario for resolving the luminosity problem requires a gradual decrease in the mean accretion rate together with episodic accretion bursts. Such accretion bursts are thought to be modulated by variations in the infall of material from large scales (Padoan et al., 2014) and by instabilities in circumstellar disks (Bell & Lin, 1994; Armitage et al., 2001; Vorobyov & Basu, 2005; Zhu et al., 2009; Martin & Lubow, 2011). Additionally, evidence from simulations indicates that episodic accretion may be needed to reproduce the peak of the Initial Mass Function (IMF; Lomax et al. 2014). Bursts are well-established in pre-main-sequence stars where they appear as FU Orionis type objects, which are young stellar objects showing strong, long-lived optical luminosity bursts (Herbig 1977; see Audard et al. 2014 for a recent review). It is not known whether deeply embedded protostars are subject to episodic outbursts to the same degree as their older, more evolved counterparts, since searches for luminosity bursts are most easily performed at optical and near-infrared wavelengths where deeply embedded objects cannot be detected. However, recently Safron et al. (2015) reported on the detection of the outbursting Class 0 protostar, HOPS 383, detected through brightening in the mid-infrared.

An accretion burst heats up the dust in the surrounding envelope on timescales that are negligible compared to the typical duration of an accretion burst (Johnstone et al., 2013). This has profound effects on the chemistry in the envelope since, following the increase in temperature, molecular ices will begin to sublimate from the dust grains and move to the gas-phase. The envelope cools rapidly once the accretion burst ends, and the molecules begin to refreeze back onto the dust grains. The process of refreezing proceeds slowly, meaning that molecules remain in the gas-phase for several thousand years following the end of the accretion burst and can therefore be used to determine whether the protostar has had a larger luminosity in the past (e.g. Visser & Bergin 2012; Vorobyov et al. 2013; Visser et al. 2015).

One of the best examples to date of using chemistry as evidence for a past luminosity burst is the case of IRAS 15398–3359, which was found by Jørgensen et al. (2013) to have $H^{13}CO^+$ distributed in a ring-like structure surrounding the protostar. The best explanation for the lack of $H^{13}CO^+$ in the innermost regions is for it to have been destroyed by water, except that the temperatures in the central regions of the envelope are too low for water ice to sublimate. The authors conclude that for water to be present in the gas-phase at these temperatures, the protostar must have undergone an accretion burst within the past $100\,\mathrm{yr}$ to $1000\,\mathrm{yr}$.

An alternative approach was presented by Jørgensen et al. (2015), who measured the spatial extent of $C^{18}O$ around 16 embedded protostars, using observations from the Submillimeter Array (SMA). By comparing the measured extents with the protostellar luminosities they found that approximately half the protostars in the sample have $C^{18}O$ distributed over a larger area than can be explained by their current luminosity, which is attributed to the protostars having had a significantly higher luminosity sometime during the past few thousand years.

This paper presents synthetic observations of $C^{18}O$ for a large sample of deeply embedded protostars, which are subjected to the same kind of analysis as in Jørgensen et al. (2015) and compared directly to their results. The synthetic observations are created from a large numerical simulation of a molecular cloud, which encompasses simultaneously protostellar system and molecular cloud scales. Simple chemistry is added to the model in the post-processing stage to be able to follow the sublimation and freeze-out of CO.

There are two goals of comparing synthetic and real observations: (1) to test the methodology employed for measuring the spatial extent of $C^{18}O$ in the observations and see how well it performs at capturing past bursts, and (2) to study how the spatial extent of $C^{18}O$, measured from the simulation, compares to the extents measured in the observations. The second point is of particular interest since the simulation is a rerun of the simulation presented in Padoan et al. (2014), where it was demonstrated that a gradual decrease in the accretion rate, together with accretion variability due to infall of material from large scales, can reproduce the observed PLF. The question at hand is whether this is enough to also explain other observables that are influenced by the accretion history, such as the measured $C^{18}O$ extents. The outline of the paper is as follows: Section 5.2 introduces the numerical simulation as well as the radiative transfer post-processing used to create synthetic observables. Section 5.3 presents the analysis applied to the synthetic observations and compare them to the observations. The results show that, while the methodology is capable of at measuring the extent of the gas-phase distribution of CO, the extents measured in the simulation are not as broadly distributed as in the observations. Section 5.4 discusses the reasons and implications of this discrepancy, while Sect. 5.5 summarises the findings of the paper.

5.2 METHODS

5.2.1 *The numerical simulation*

The numerical simulation has been run using the Adaptive Mesh Refinement (AMR) code, `RAMSES` (Teyssier, 2002), modified to include random turbulence driving, a novel algorithm for sink particles, and technical improvements allowing for efficient scaling to several thousand cores. The simulation is part of a suite of simulations run by Haugbølle et al. in preparation, investigating the IMF. It is simultaneously a rerun of the simulation presented by Padoan et al. (2014), except for a few aspects described below, and we refer to that paper for details on the numerical setup. The simulation encompasses simultaneously molecular cloud and protostellar system scales with a box-size of $4\,\mathrm{pc}$ and a minimum cell size of $50\,\mathrm{AU}$. The root grid of the simulation is 256^3, with an additional 6 levels of AMR on top. The refinement is based on density and is such that the Jeans length is resolved with at least 14 cells everywhere. The total mass in the box is $2998\,M_\odot$ corresponding to an average number density of $795\,\mathrm{cm}^{-3}$ assuming a molecular weight of 2.4. The initial magnetic field has a strength of $7.2\,\mu\mathrm{G}$. The simulation is run for a total time of $2.6\,\mathrm{Myr}$ and forms a total of 635 sink particles. Figure 5.1 shows the projected density, along with the sink particles, of one of the snapshots in the simulation.

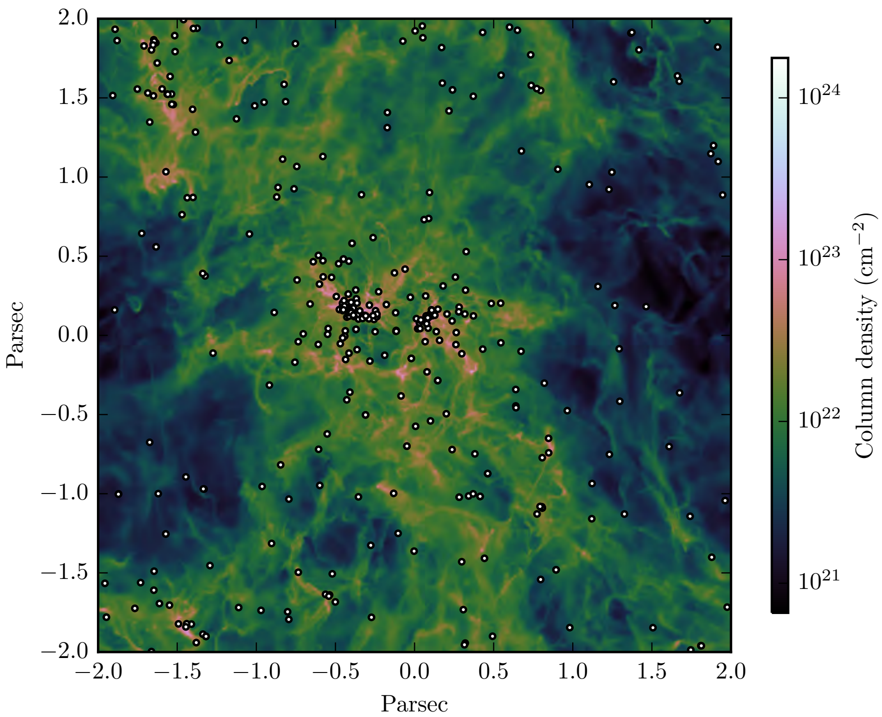

Figure 5.1: Projected gas number density and sink particle positions of a snapshot in the simulation 2.2 Myr after the formation of the first sink. The total number of sink particles at this point is 454.

There are two aspects where the present run differs from that of Padoan et al. (2014): (1) a slightly improved magnetohydrodynamics (MHD) solver and (2) changes in the numerical sink particle parameters. In the current run the slope reconstruction and limiting procedure interpolating from cell centres to cell interfaces is more isotropic and less diffusive, while still being stable in supersonic flows. Both the original and the present run use the HLLD solver, but switch to a diffusive Local Lax Friedrich (LLF) solver at trouble cells. In the original run we changed to the LLF solver at cells where the local fast mode speed exceeded 100 times the local sound speed, while for the present run we were able to switch at 300, reducing the typical number of cells where LLF is employed to ~2 %. The sink particle parameters were changed slightly. The density threshold for sink particle creation is increased with a factor of 13 to 2.1×10^6 times the average density or $1.7 \times 10^9\,\mathrm{cm}^{-3}$. This makes the algorithm more robust and we can reduce the minimum distance between new and existing sink particles from 16 to 8 cells, corresponding to 400 AU. We also reduced the threshold density for considering gas accretion with a factor of 30 to an overdensity of 5.3 or $4226\,\mathrm{cm}^{-3}$, to make it possible to follow accretion in evolved systems down to $10^{-10}\,\mathrm{M}_\odot\,\mathrm{yr}^{-1}$. The combined effect of the changes is less diffusive gas dynamics and an almost perfect suppression of spurious sink particles. We denote sink particles spurious if they are created by chance close to other sink particles instead of from bona fide gravitationally collapsing regions of the gas. This can happen, for example, in the accretion flow close to an existing sink particle, where the gas density can get very high. While it does not affect the conclusions of the Padoan et al. paper, we later found a method to estimate the fraction of spurious sinks and found it to be ∼10 % of all sinks in the original simulation. In the rest of the paper we refer to the sink particles as "protostars".

5.2.2 *Post-processing*

To produce observables the simulation is post-processed using the radiative transfer code `RADMC-3D`[1] (see Dullemond & Dominik 2004 for a description of the two-dimensional version of this code). Much of the post-processing is equivalent to what was done in Frimann et al. (2016a), so the reader is referred to that paper for details. The most important aspects of the post-processing are repeated here, along with a full description of the synthetic line observations.

As in Frimann et al. (2016a), `RADMC-3D` is run on cubical cut-outs with side lengths of ≈30 000 AU, centred around individual protostars. `RADMC-3D` can handle AMR grids natively and it is therefore not necessary to resample the simulation output onto a regular grid. The cut-outs are made by cycling through all protostars in all snapshots of the simulation, with each cut-out corresponding to one `RADMC-3D` model. Each individual cut-out may contain several protostars, but for each `RADMC-3D` model the central protostar is the only source of luminosity.

5.2.2.1 *Radiative transfer*

The thermal Monte Carlo module of `RADMC-3D` uses the method of Bjorkman & Wood (2001) to calculate the dust temperatures in the models. The method relies on the propagation of a number of "photon packets" through the model, which, in our case, has been set to ten million. We use the OH5 dust opacities of Ossenkopf & Henning (1994), corresponding to coagulated dust grains with thin ice mantles at a density of $n_{H_2} \sim 10^6\,\mathrm{cm}^{-3}$, which have been found to be appropriate for dense cores by several studies (e.g. Shirley et al. 2002, 2011). A dust-to-gas mass ratio of 1:100 is assumed everywhere. The luminosity of the central protostar is calculated as the sum between the accretion luminosity, arising from accretion onto the protostar, and the photospheric luminosity, arising from deuterium burning and Kelvin-Helmholtz contraction

$$L_\star = L_{phot} + L_{acc} = L_{phot} + f_{acc}\frac{G\dot{m}m_\star}{r_\star}, \tag{5.1}$$

1 http://www.ita.uni-heidelberg.de/~dullemond/software/radmc-3d/

where $m_\star$ is the mass of the protostar; $\dot{m}$ the instantaneous accretion rate onto the protostar; $r_\star$ the protostellar radius, taken to be $2.5\,R_\odot$; and f_{acc} is the fraction of accretion energy radiated away, taken to be 1. The accretion rate, $\dot{m}$, is calculated from an auxiliary output file of the simulation, recording the time evolution of the protostellar masses. The sampling rate of this time series has a median value of $\approx 30\,\mathrm{yr}$ meaning that accretion rates are averaged over this time interval. L_{phot} is calculated using the pre-main-sequence tracks of D'Antona & Mazzitelli (1997), where we follow Young & Evans (2005) and add $100\,\mathrm{kyr}$ to the tabulated ages to account for the time difference between the beginning of core-collapse and the onset of deuterium burning. The protostars are assumed to emit as perfect black bodies with an effective temperature of $1000\,\mathrm{K}$.

5.2.2.2 *Freeze-out and sublimation chemistry*

Simple freeze-out and sublimation chemistry is added to the code to simulate the situation following an accretion burst where molecules are still in the process of refreezing back onto the dust grains. Following Rodgers & Charnley (2003) the thermal sublimation rate of ices sitting on top of dust grains can be written as

$$k_{sub} = \nu \exp\left(-\frac{E_b}{k_B T_{dust}}\right). \tag{5.2}$$

The prefactor, ν, is set to $2 \times 10^{12}\,\mathrm{s}^{-1}$, appropriate for a first order reaction (Sandford & Allamandola, 1993). E_b is the binding energy of the molecule on the dust grains. We adopt a value for the binding energy, E_b/k_B, of $1307\,\mathrm{K}$ appropriate for a mixture between water and CO ice (Noble et al., 2012). This corresponds to a sublimation temperature, T_{sub}, of approximately $28\,\mathrm{K}$, where T_{sub} is defined as the temperature where the sublimation timescale is one year.

Following again Rodgers & Charnley (2003), the freeze-out rate can be written as

$$k_{dep} = 2.88 \times 10^{-11}\,\mathrm{s}^{-1} \sqrt{\frac{T_{gas}}{\mu\,10\,\mathrm{K}}}\,\frac{n_{H_2}}{10^6\,\mathrm{cm}^{-3}}, \tag{5.3}$$

where μ is the molecular weight of the considered species and the prefactor has been calculated assuming $n_{grain}/n_{H_2} = 2 \times 10^{-12}$, an average dust grain radius of $0.1\,\mu\mathrm{m}$, and unit sticking coefficient. Gas and dust temperatures are assumed to be equal.

The goal is to be able to calculate the gas-phase abundance of CO, $X_{co,gas} \equiv n_{co,gas}/n_{H_2}$, in each cell of the `RADMC-3D` model, while taking into account the luminosity history of the central protostar. The total CO abundance, $X_{co,tot} = X_{co,gas} + X_{co,grain}$, is set to the canonical value of 10^{-4}. `RAMSES` is a grid-based model, which means that it is not possible to follow the dynamical evolution of individual particles

– a follow-up study with tracer particles included in the RAMSES simulation will be able to do this, but probably not for a large sample of objects. Instead, the gas-phase abundance of CO is calculated using the procedure sketched out in the following paragraph.

The density distribution in the RADMC-3D model is held fixed, while the temperatures in the model are recalculated for a range of different luminosities, based on the luminosity history of the central protostar. The temperatures are not recalculated for each unique luminosity the protostar has had in the past, but are sampled on a logarithmic luminosity grid starting from $10^{-5}\,L_\odot$ and increasing in steps of 3 % from there. Naturally, the temperatures are only calculated for grid points within the luminosity range covered by the protostar. The grid is interpolated using a power law from the nearest grid point, $T_{\mathrm{interpolated}}/T_{\mathrm{grid}} = (L_{\mathrm{actual}}/L_{\mathrm{grid}})^{0.2}$, where the power law exponent has been measured empirically. $X_{\mathrm{co,gas}}$ is calculated individually in each cell of the RADMC-3D model, effectively making each cell its own one-zone model. If the dust temperature in a cell is higher than the sublimation temperature, $T_{\mathrm{dust}} > T_{\mathrm{sub}}$, then $X_{\mathrm{co,gas}} = X_{\mathrm{co,tot}}$; on the other hand if $T_{\mathrm{dust}} < T_{\mathrm{sub}}$ then $X_{\mathrm{co,gas}}$ is calculated using Eq. (5.3), with $\min(X_{\mathrm{co,gas}}) = 0.01 \times X_{\mathrm{co,tot}}$ to reflect the fact that non-thermal desorption processes (e.g. cosmic rays) ensure that CO is never completely frozen-out. The system is evolved starting from the maximum luminosity it has had in the past, where $X_{\mathrm{co,gas}}$ is initialised so that $X_{\mathrm{co,gas}} = X_{\mathrm{co,tot}}$ for $T_{\mathrm{dust}} > T_{\mathrm{sub}}$, and $X_{\mathrm{co,gas}} = 0.01 \times X_{\mathrm{co,tot}}$ for $T_{\mathrm{dust}} < T_{\mathrm{sub}}$.

5.2.2.3 *Synthetic line cubes*

The end product of the post-processing are synthetic observables, in the form of line cubes. The main isotopolouge of CO is optically thick at the densities found in protostellar cores so an optically thin isotopolouge is typically used. In this case, the synthetic line cubes are of the $C^{18}O$ J = 2–1 line and are produced using the line radiative transfer module in RADMC-3D assuming Local Thermodynamic Equilibrium (LTE). Jørgensen et al. (2002) showed that, for low J rotational transitions and the high densities characteristic of deeply embedded objects, LTE is a good approximation. The gas-phase abundances of CO are calculated as described in Sect. 5.2.2.2 above and we calculate the number densities of $C^{18}O$ assuming a $^{16}O/^{18}O$ ratio of 500. The spatial extent covered by the cubes is 10 000 AU × 10 000 AU and they are given a spatial resolution of 25 AU. This is a factor of two higher than the maximum resolution of the simulation, as well as in the RADMC-3D model, and we choose this slight over-sampling to ensure that the resolution of the model is not accidentally degraded by ray tracing along cell borders. The width of the spectral window is $10\,\mathrm{km\,s^{-1}}$, with a resolution of $0.1\,\mathrm{km\,s^{-1}}$ centred around the $C^{18}O$ 2–1 line. Figure 5.2 shows examples of zero moment maps of some of

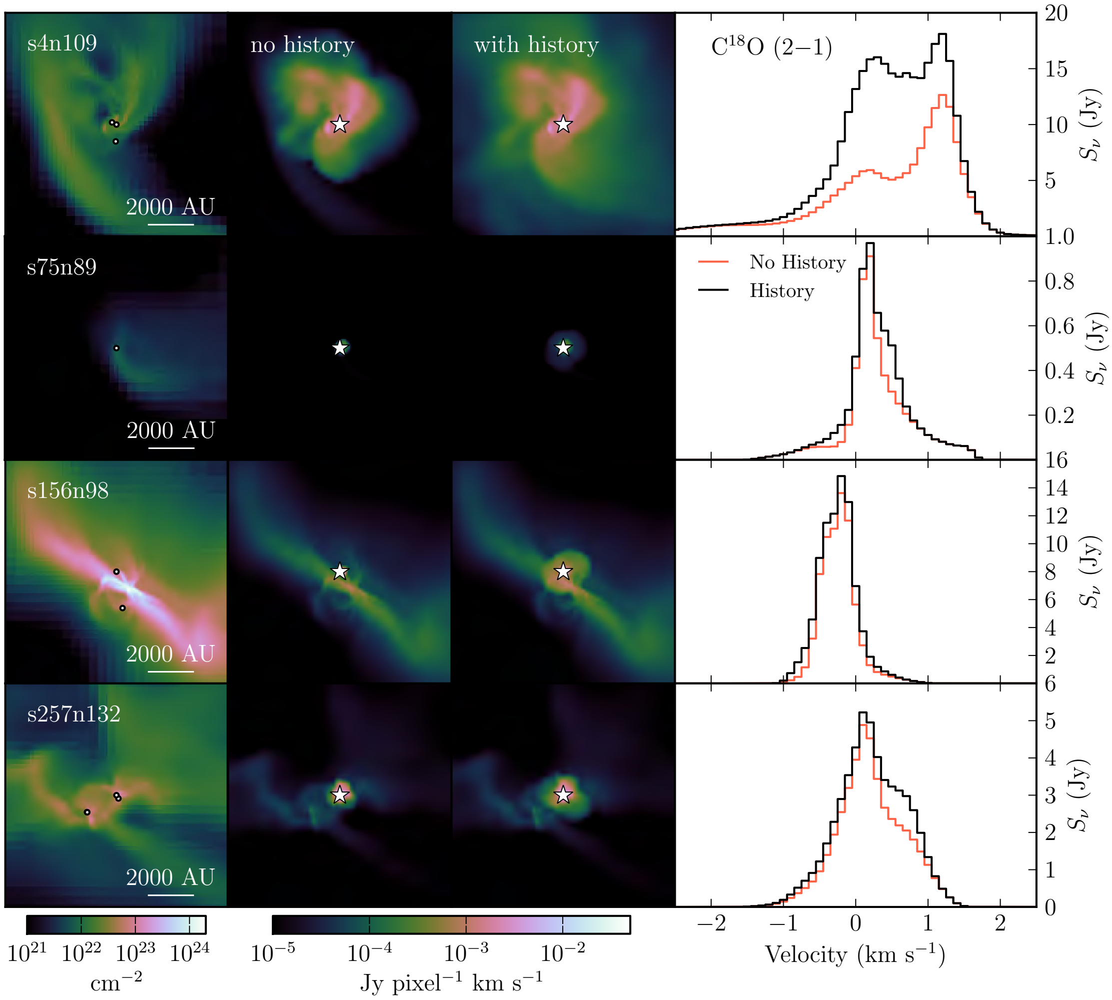

Figure 5.2: From raw simulation to synthetic observables for four different systems. From left to right: projected gas column density of the raw simulation, with dots indicating protostars; zero moment maps of the C^{18}O 2–1 line; line spectra of the two zero moment maps. In the column labelled "no history" the C^{18}O number densities have been calculated without taking the luminosity history of the central protostar into consideration, while, in the column labelled "history", the luminosity history has been included. The line spectra have been calculated by integrating over the entire field of view as seen in the moment maps.

the synthetic line cubes along with spectra of the $C^{18}O$ 2–1 line and column density maps of the raw simulation. The column labelled "no history" shows zero moment maps calculated from `RADMC-3D` models, where the gas-phase abundance of CO only depends on the current luminosity; in the column labelled "history", the luminosity history of the protostar has been taken into account. All results and figures presented in this paper are derived assuming a source distance of 235 pc.

5.3 SYNTHETIC OBSERVATIONS

The synthetic observations analysed in this paper are compared to the observations presented by Jørgensen et al. (2015). To create a context for the later comparison, these observations are described briefly here. The authors use the SMA to observe the $C^{18}O$ $J=2\text{–}1$ line towards 16 deeply embedded Class 0 and I sources in a number of the nearby star-forming regions. The observations utilise SMA's compact configuration, which gives a spatial resolution of roughly 2″, corresponding to a baseline radius of approximately 50 kλ. Resolved zero moment maps, of the $C^{18}O$ emission, show centrally concentrated emission with evidence of some low surface brightness extended emission for a few objects. The authors measure the deconvolved extent of CO emission by fitting one-dimensional Gaussians to the (u, v)-data and find, after allowing for various observational uncertainties, that approximately half of the protostars in the sample have CO distributed over a larger area, than can be explained by the current protostellar luminosity, indicating that the luminosity has been larger sometime in the past.

5.3.1 *Target selection*

Over the course of its running time, the simulation forms a total of 635 protostars and stores 119 snapshots, yielding a total of 30 340 `RADMC-3D` models (this number is not equal to the total number of protostars times the number of snapshots because not all protostars are present in all snapshots). It is impractical to calculate molecular line cubes for such a large number of models, both in terms of computing time and space needed to store the cubes. Additionally, the purpose of this study is to compare the synthetic cubes with the 16 deeply embedded protostars observed by Jørgensen et al. (2015), hence only objects that match the observed sample should be included. For these reasons a number of selection criteria are applied to the full sample of `RADMC-3D` models, with the goal of reducing the sample to only include the objects of interest. These selection criteria are discussed below, but the end result is that the sample of `RADMC-3D` models is reduced from 30 340 to 1952. In addition to this, for each `RADMC-3D`

Table 5.1: Example object parameters. The first column is the protostellar mass, followed by its age and luminosity. T_{bol} is the bolometric temperature as defined by Myers & Ladd (1993). $M_{10\,000\,AU}$ is the gas mass within a radius of 10 000 AU from the protostar. Finally, n_0 and p are the fitted parameters for the power law, $\rho(r) = n_0(r/100\,AU)^{-p}$.

	$M_\star$ ($M_\odot$)	Age (kyr)	L_{bol} ($L_\odot$)	T_{bol} (K)	$M_{10\,000\,AU}$ [a] ($M_\odot$)	n_0 (cm^{-3})	p
s4n109	5.1	1037	70.4	259	0.5	1.6×10^6	1.5
s75n89	0.2	248	0.9	330	0.1	5.5×10^5	1.3
s156n98	0.1	16	1.4	54	2.4	8.4×10^6	1.3
s257n132	0.3	175	5.6	84	1.0	5.2×10^6	1.4

Notes. [a] Gas mass inside a radius of 10 000 AU.

model in the sample, three synthetic line cubes are calculated for three orthogonal viewing angles, effectively increasing the sample size with a factor of three.

The first selection criterion removes all sources with a luminosity outside the range 0.5 $L_\odot$–200 $L_\odot$. The motivation for this criterion is to only include sources where CO is expected to be in the gas-phase on the spatial scales which can be probed by the interferometer. The second selection criterion seek to avoid binary stars by requiring that the distance to the nearest protostar is >400 AU. The remaining selection criteria all seek to pick out the deeply embedded objects. The first of these is based on the SEDs of the protostars. Using the same method as in Frimann et al. (2016a) we calculate the bolometric temperature (Myers & Ladd, 1993) for all objects in the simulation and choose only objects with $T_{bol} < 650$ K, corresponding to Class 0 and I protostars (Chen et al., 1995). To select only objects with a strong central concentration of density, power law functions, of the form $\rho(r) = n_0(r/100\,AU)^{-p}$, are fitted to the protostellar envelopes. To include the protostar in the sample, we require the fitted values, n_0 and p to be $> 10^5$ cm^{-3} and > 1.3 respectively. Finally, it is required that the total gas mass within a radius of 10 000 AU from the protostar is larger than 0.1 $M_\odot$. In this way we seek to match the sample of deeply embedded protostars observed by Jørgensen et al. (2015).

Figure 5.2 shows the projected gas density, zero moment maps and $C^{18}O$ line spectra of four of the objects in the reduced sample. These objects are chosen so that they span the full range of luminosities in the sample and so that each object has had a larger luminosity in the past, making a visible difference on the moment maps whether or not the luminosity history is taken into consideration. Additional information about the four objects can be found in Table 5.1.

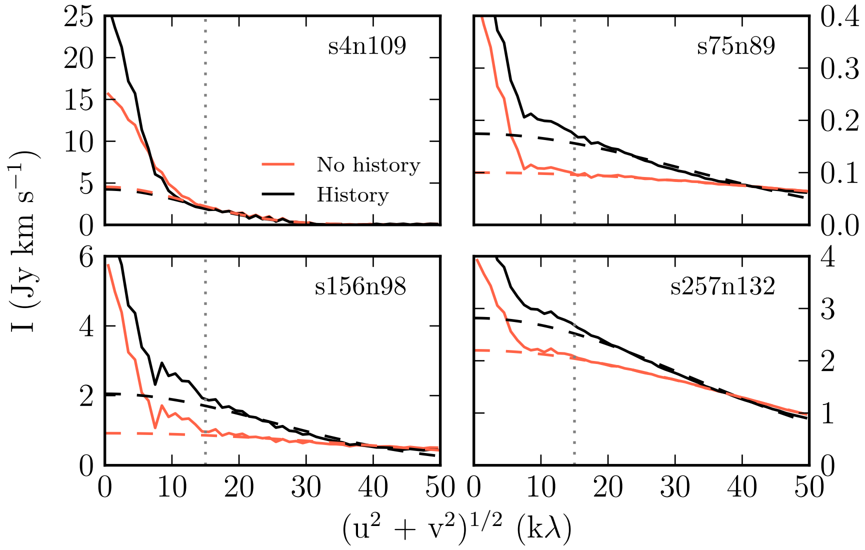

Figure 5.3: (u, v)-amplitude plots of the four objects shown in Fig. 5.2. As before, the black line shows the situation including luminosity history and the red line the situation without. The dashed lines show the fitted Gaussians for each situation. The dotted line show the 15 kλ lower limit imposed on the fit. The upper limit on the fit is 50 kλ.

5.3.2 *Analysis*

To measure the spatial extent of $C^{18}O$ emission around the protostars in the sample, the synthetic line cubes are first multiplied with a primary beam and Fourier transformed so that the images are sampled in the (u, v)-plane for better comparison with interferometric observations. The (u, v)-data are subsequently fitted with a Gaussian to measure the deconvolved extent of $C^{18}O$ emission (see Fig. 5.3 for some examples). Jørgensen et al. (2015) did not use baselines $< 15\,\mathrm{k}\lambda$ to avoid emission from the ambient medium, for example caused by external heating from the Interstellar Radiation Field (ISRF). We do not include an interstellar radiation field, or similar, in our models, but retain the 15 kλ limit for consistency with the observations. Likewise, baselines >50 kλ are disregarded to emulate the baseline coverage of the SMA.

One of the features of Fourier transforms is that the Fourier transform of a Gaussian is itself a Gaussian. This means that, after fitting the Gaussian and finding the Full Width at Half Maximum (FWHM) of the emission in the (u, v)-plane, the expected FWHM of the emission in the image plane can be found immediately by using the transformation

$$\mathrm{FWHM(arcsec)} = \frac{182}{\mathrm{FWHM(k\lambda)}}.$$

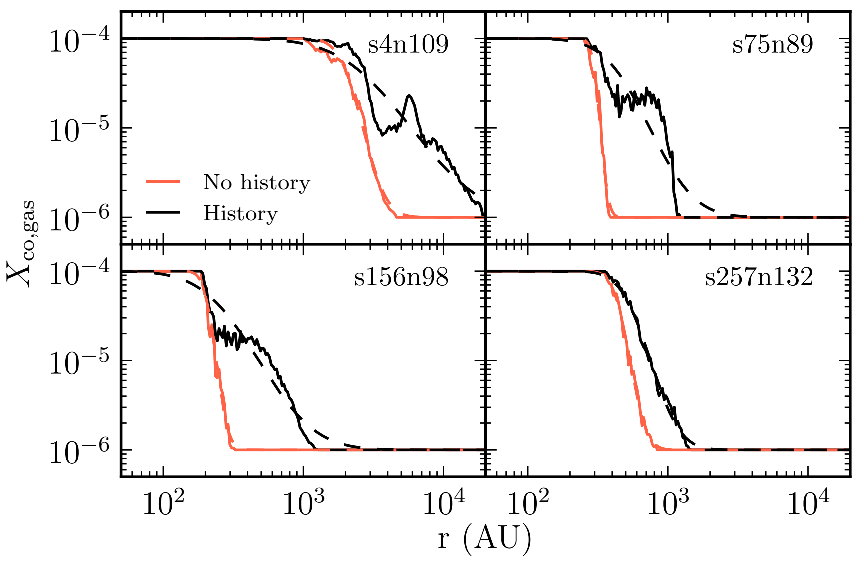

Figure 5.4: Abundance profiles of the four example objects. The profiles are fitted with cumulative Gaussian functions in loglog-space, shown as dashed lines.

This expression can also be used to estimate the limits on the size-scales that can be probed with the interferometer, given the baseline limits of 50 kλ and 15 kλ. A FWHM in the (u, v)-plane of 100 kλ ($2 \times$ 50 kλ) correspond to a FWHM in the image plane of 1.8″, while a FWHM of 30 kλ (2×15 kλ) correspond to 6.1″.

The fitted Gaussians are one-dimensional, which is expected to work well if the emission is roughly axisymmetric. To test if this is the case we also fitted two-dimensional Gaussians to the objects in the sample. On average, the minor and major axes of the two-dimensional Gaussians are within 20 % of each other, with higher luminosities, where the emission is spread out over a larger area, having a higher probability of being asymmetric. Comparing the geometric mean of the minor and major axes of the two-dimensional Gaussians to the FWHM of the one-dimensional Gaussians reveals that, for 90 % of the objects, they agree within 1 %. This shows that, even in cases where the emission may be somewhat asymmetric, the one-dimensional fit will converge towards a reasonable value.

In addition to fitting Gaussians in the (u, v)-plane we also calculate abundance profiles of all objects by averaging $X_{co,gas}$ over concentric shells around the protostar (see Fig. 5.4 for some examples). The abundance profiles make it possible to measure the spatial extent of the gas-phase CO independently of the fitted Gaussians. Specifically, the spatial scale of gas-phase CO is measured from the abundance profile by fitting a cumulative Gaussian function (an error function) in loglog-space to get the mean. The extents measured by the two methods differ by a roughly constant scale factor, which we measure to be 2.0 ± 0.2 (one-sigma uncertainty). The measurement has been limited to luminosities between $4\,L_\odot$ and $10\,L_\odot$ to avoid uncertainties due to the baseline limits. The results from the two methods can be compared directly, either by applying the scale factor or by comparing ratios between measurements.

Table 5.2 records the extents of the four example objects, measured from both the fitted Gaussians and abundance profiles. The table also records the predicted extents calculated using the expression

$$R_{CO} = 90\,\mathrm{AU}\left(\frac{L}{1\,L_\odot}\right)^{0.52}. \tag{5.4}$$

This expression is calculated by fitting Gaussians in the (u, v)-plane of a simple one-dimensional envelope model with a power law density profile, $\rho \propto r^{-p}$ with $p = 1.5$, and a total mass of $1\,M_\odot$. The quantity R_{CO} is the Half Width Half Maximum of the fitted Gaussian (FWHM/2) and is reported in physical rather than angular units to make comparison with the abundance profiles easier. Table 5.2 also gives the time interval since the peak luminosity as well as the peak luminosity itself.

For some objects it is not possible to measure the extent of $C^{18}O$ accurately because most of the emission fall outside of the $15\,k\lambda$–$50\,k\lambda$ baseline range used for fitting the Gaussians. An example of this is the object s4n109, whose luminosity is so high that most of the emission is at baselines $<15\,k\lambda$. The high luminosity also means that even if such an object has undergone a luminosity burst in the past it will not be detected since the extended emission will be on even smaller baselines. The situation is similar for the objects s75n89 and s156n98, whose luminosities are so low that the half intensity point of the emission is at baselines significantly larger than $50\,k\lambda$. The difference relative to high-luminosity protostars is that, for low-luminosity protostars, bursts are easier to detect because the extended emission will be at shorter baselines covered by the interferometer.

For one of the objects, s75n89, the time interval since its peak luminosity is 143 kyr, yet CO is still distributed over an extended area. This is a result of the density in the inner regions of the envelope being rather low ($\sim 10^5\,\mathrm{cm}^{-3}$ corresponding to a freeze-out timescale of $\sim$100 kyr). It is not clear that such a situation would be observed in nature since, at such long timescales, the dynamics of the system also becomes important. For the case at hand, the free-fall time for a particle sitting at a distance of 700 AU from the protostar is $\sim$10 kyr – a factor of ten shorter than the time interval since the peak luminosity – indicating that, after 143 kyr, much of the gas-phase CO would have fallen towards the centre of the system.

Contamination from the ambient medium is an issue at the smallest baselines, as shown in Fig. 5.3 where the emission is seen to increase sharply at small baselines for three out of four systems (for the fourth

Table 5.2: Measured extents.

	R_{CO} (AU)			Ratio[a]	Abund. radius (AU)		Ratio[a]	Δt_{peak} (kyr)[b]	L_{peak} ($L_\odot$)[b]
	Predict	No hist.	Hist.		No hist.	Hist.			
s4n109	820	730	720	1.0	2660	5900	2.2	…[c]	…[c]
s75n89	90	170	290	1.7	330	740	2.3	143	5.8
s156n98	110	220	360	1.6	240	480	2.0	8	13.6
s257n132	220	240	280	1.2	540	750	1.4	4	8.8

Notes. [a] The ratios are calculated between the measured extents with luminosity history, relative to no history. [b] Time since peak luminosity and the luminosity of the peak. [c] The luminosity of this object is highly variable and it is not possible to determine one single luminosity peak in the past that is responsible for the extended abundance profile. The luminosity of the object topped at 900 $L_\odot$ 650 kyr prior to the time of the snapshot.

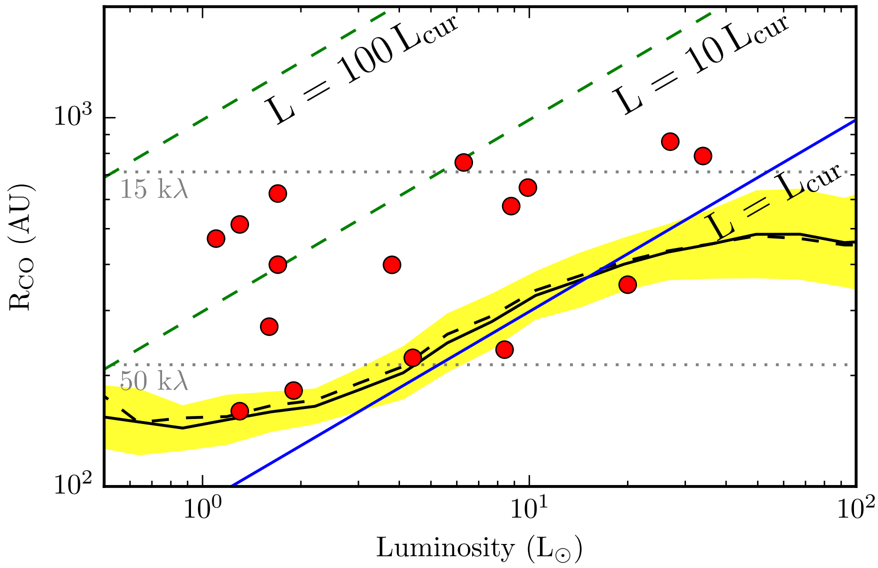

Figure 5.5: R_{CO} vs. luminosity. The black line is the measured extent from the simulation without any history, with the shaded area giving the one-sigma uncertainty. The black dashed line is the measured extent including luminosity history. The red points are the observations from Jørgensen et al. (2015). The blue line is the predicted extent given by Eq. (5.4). The dotted lines show the 15 kλ and 50 kλ baseline limits, assuming a source distance of 235 pc.

system the luminosity is so high that most of the envelope emission is already at the small baselines). In nature, the situation is further aggravated by the presence of external heating through the ISRF and by low-density "pre-depletion" regions where CO has not yet frozen out, which may also increase the emission at the shortest baselines. This is an important consideration to take into account, when choosing how small baselines to include in the measurements.

5.3.3 *Comparison with observations*

Figure 5.5 shows R_{CO} as function of luminosity for the systems in the simulation. The black line in the figure is the binned median of R_{CO}, measured for the protostars in the simulation, without including the luminosity history. The shaded area is the one-sigma standard deviation of R_{CO}. At intermediate luminosities R_{CO} is seen to follow the blue line, which is the predicted extent given the current luminosity (see Eq. 5.4). At both low and high luminosities the black curve flattens due to the 15 and 50 kλ baseline cut-offs. The measured extents do a little better than predicted for the low luminosities/small extents while for high luminosities/large extents they do a little worse. This is connected to the fact that the fitted Gaussians are very sensitive to the amplitude of the emission. For high luminosities, where most of

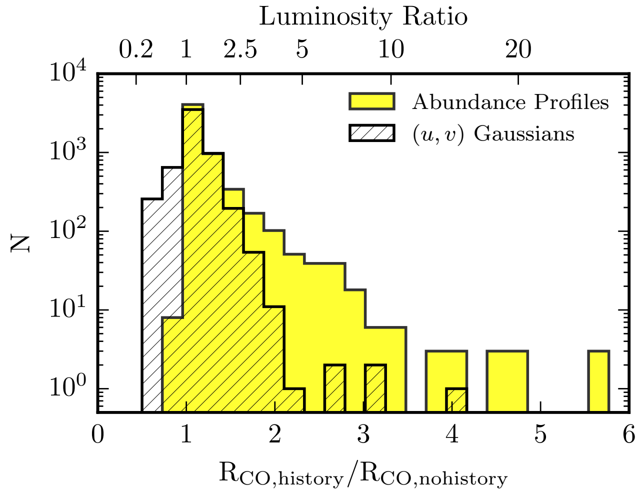

Figure 5.6: Ratios of extents measured from the (u, v)-plane and from the abundance profiles. The lower axis show the measured ratios and the upper axis the corresponding luminosity ratio calculated using Eq. (5.4). $R_{CO,no\,history}$ has been calculated using a wider (u, v)-coverage spanning from 5 kλ to 200 kλ, to get a good reference value. $R_{CO,history}$ has been calculated using the standard (u, v)-coverage.

the emission is at the short baselines, this often leads to an underestimation of the amplitude and consequently an underestimation of R_{CO}. Conversely, for small extents, where it is easier to fit the amplitude, R_{CO} can be measured reliably even if it lies at baselines that are somewhat larger than those probed by the interferometer.

The red points in Fig. 5.5 are the protostars observed by Jørgensen et al. (2015), many of which have measured extents that are larger than can be explained by their current luminosity. Given that these are real observations there is an uncertainty associated with the measurements, originating from sources such as calibration, distance, and luminosity uncertainties. Jørgensen et al. (2015) estimated that they could reliably detect extents corresponding to the luminosity being ~5 times brighter than the current luminosity, which is the case for approximately half of the observed objects.

The black dashed line in Fig. 5.5 is the binned median of R_{CO} including luminosity history. The curve shows a marginally larger median value of R_{CO} relative to the situation with no history, however the increase is so slight that it is evident that only a small minority of systems are affected by the inclusion of luminosity history. Using Eq. (5.4) as a reference ~1 % of the systems in the sample have a measured extent consistent with the protostar having been at least a factor of five brighter in the past.

Another way of illustrating the effects (or lack thereof) of including luminosity history is to calculate the ratio between the measured extents with and without luminosity history. A histogram of this is shown in Fig. 5.6, which also shows the same ratio calculated from the abundance profiles. Both histograms peak at a ratio of 1, with a tail towards higher ratios. The tail is significantly larger for the histogram of the abundance profiles, where 2 % have a ratio consistent with the luminosity having been at least a factor of five brighter in the past. For the ratios measured by fitting Gaussians in the (u,v)-plane this is only true for six out of a total of more than 5800 cubes. There are several reasons why the ratios calculated from the abundance profiles have a larger tail towards high ratios – the abundance profiles are, for example, not affected by baseline limits – but the most important reason is that the radius measured for the abundance profile remain sensitive to an increased gas-phase abundance of CO for longer than the synthetic observables.

While differences in the physical structure of the envelopes are automatically accounted for in the measured extents potential variations of the sublimation temperature, T_{sub}, are not automatically taken into account. Pure CO ice has a binding energy, E_b/k_B, in the range 855 K–960 K (Sandford & Allamandola, 1993; Bisschop et al., 2006) corresponding to a sublimation temperature, $T_{sub} \approx 20$ K. For CO mixed with H_2O the binding energy is increased to ≈1200 K–1300 K (Collings et al., 2003; Noble et al., 2012), corresponding to $T_{sub} \approx 28$ K. A lower sublimation temperature would increase the predicted extent of CO at all luminosities, but would struggle to explain the compact emission measured towards some of the observed objects. A number of spatially unresolved observational studies have found CO to sublimate at 25 K–40 K by coupling line observations of CO to simple parametric models of the envelopes with step functions describing the CO abundance (Jørgensen, 2004; Jørgensen et al., 2005b; Yıldız et al., 2013). Despite the small samples and large uncertainties associated with these studies, they do suggest that the sublimation temperature of CO in cores is higher than that of pure CO ice, but also indicate that source-to-source variations may be important. The latter point especially may have important consequences for the interpretation of the observational results and underline the importance of both high quality laboratory measurements and large observational surveys dedicated to the study of the location of the CO ice lines.

5.3.4 *Baseline effects*

The availability of baselines restrict the extents that can be measured with the interferometer. Baseline limits of 15 kλ and 50 kλ suggest that spatial extents between 1.8″ and 6.1″ can be measured. A glance at the black line in Fig. 5.5 suggests that the actual limits are closer to 1.3″ and 4.0″. It is possible that the fully automatic fitting procedure

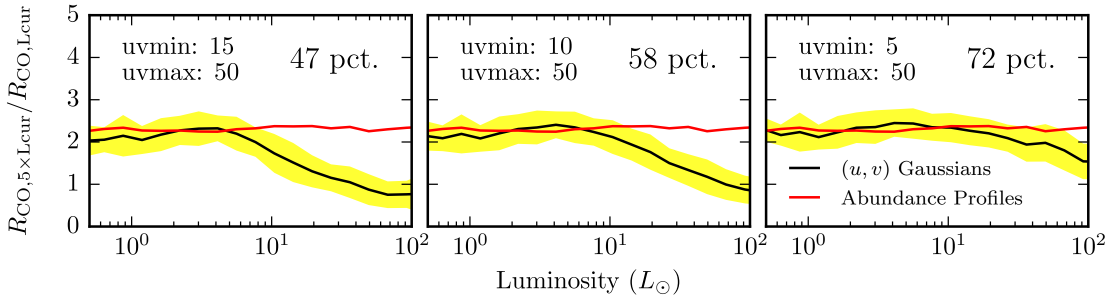

Figure 5.7: Ratios between measured extents as function of luminosity. The shaded area is the one-sigma uncertainty of the ratio measured from the (u, v)-plane. The (u, v)-range used for calculating the extent of $R_{\text{CO,5×Lcur}}$ is shown in the upper left of each panel. The number in the upper right corner of each panel indicate how large a fraction of the ratios measured from the (u, v)-plane are within 20 % of the ratios measured from the abundance profiles.

applied here aggravate the situation somewhat and that better fits can be made for some of the sources by providing better starting guesses.

To get a better grasp of the influence of the baseline limits on the results, we calculate a sample of synthetic line cubes where the luminosity of the central protostar has been enhanced by a factor of five, relative to the standard situation. The CO extents are measured in the cubes with enhanced luminosities for different baseline coverages and divided by the measured extents for the cubes with the non-enhanced luminosities to get the ratio. As in Fig. 5.6 the extents of the reference cubes have been measured using a wide (u, v)-coverage spanning from 5 kλ to 200 kλ, to provide a good reference value. A ratio is also calculated for the extents measured from the abundance profiles between the enhanced and non-enhanced luminosities.

Figure 5.7 shows the measured ratios as functions of luminosity. For a luminosity enhancement by a factor of five Eq. (5.4) predicts a ratio of 2.3, which is matched perfectly by the abundance profiles in the figure. The ratios calculated from the (u, v)-fits start declining at high luminosities because the emission is being spread out over larger spatial scales. Including smaller baselines in the fit is seen to delay the decline, making it possible to measure bursts at higher luminosities than normally possible. Access to longer baselines improve the measurements for small luminosities, but is not as crucial for the detection of bursts.

In general, one should be careful with including small baselines in the fits, however our results indicate that for luminosities $\gtrsim 5$ it may be necessary in order to catch bursting sources. As seen in Fig. 5.4 the emission from the ambient medium typically only becomes important for baselines <10 kλ, as does the ISRF (Jørgensen et al. 2015, Fig. 3).

We therefore recommend 10 kλ as a lower boundary when trying to measure large extents.

5.4 DISCUSSION

The spatial resolution of the simulation is 50 AU, which is not enough to form circumstellar disks. The accretion rates onto the protostars in the simulation are therefore primarily modulated by variations in the infall of material from the large scales of the molecular cloud. Such variations, along with a gradual decrease in the mean accretion rate, are sufficient to reproduce the observed PLF (Padoan et al., 2014; Frimann et al., 2016a), but, as the results of this paper demonstrate, they are not enough to reproduce the observed spread of $C^{18}O$ extents seen in observations.

To get a firm idea of how many systems with extended emission one can expect to find in the sample of protostars from the simulation, we analyse the luminosity time series of all the objects in the sample to see how large a fraction of the systems have had their luminosity enhanced by some factor in the past (black solid line in Fig. 5.8; the red solid line shows the distribution of the real observations). We find that 2 % of the systems have had their luminosity increased by at least a factor of five within the past 10 kyr and 1 % of the systems by at least a factor of 10. This is similar to the enhancements measured for the abundance profiles in Fig. 5.6 and indicate that the discrepancy between the real and synthetic observations are due to the luminosity bursts in the simulation not being numerous or intensive enough.

It is possible that the selection criteria employed in Sect. 5.3.1 exclude important families of bursting protostars. Binary stars, for example, may be subject to increased variability since their accretion histories also depend on interactions with their companion. Redoing the analysis described above for the same sample of objects, but including binaries, reveal virtually no difference between the distributions (dotted line in Fig. 5.8). We remark that, due to the relatively low spatial resolution in the simulation and the fact that protostars cannot form closer than 400 AU to one another, the direct formation of close binaries is not modelled – though close binaries resulting from dynamical interactions do occur – and the analysis therefore does not rule out binarity as an important source of accretion variability.

Similarly, low-luminosity protostars may be subject to large fractional luminosity enhancements due to the low reference luminosity. Redoing the analysis yet again for the standard sample of protostars, but this time including objects with luminosities down to 0.05 $L_\odot$, shows that the fraction of object at high luminosity ratios does increase significantly (dashed line in Fig. 5.8), but still not enough to match the observed distribution.

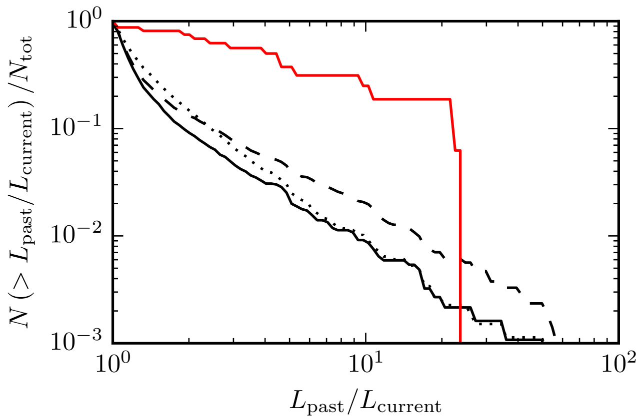

Figure 5.8: Cumulative distribution of systems in the simulation that have had their luminosity increased by at least some factor, given by the horizontal axis, in the past. The black solid line is the distribution of the sample presented in Sect. 5.3.1, while the red solid line is the distribution of the Jørgensen et al. (2015) observations shown in Fig. 5.5. The dotted line is for the same sample, but including binaries, while the dashed line include protostellar luminosities down to 0.05 $L_\odot$. The lookback time is 10 kyr.

The traditional view of FU Orionis type objects are that they are evolved objects, possibly with some remaining envelope material, with periodic luminosity outbursts driven by various types of disk instabilities (Bell & Lin, 1994; Armitage et al., 2001; Vorobyov & Basu, 2005; Zhu et al., 2009; Martin & Lubow, 2011). This view is supported by SED fitting of disk models to individual objects, such as FU Orionis itself (Zhu et al., 2007). There is increasing evidence for the presence of disks, even around deeply embedded objects, both from an observational perspective (Jørgensen et al., 2009; Tobin et al., 2012; Murillo et al., 2013; Lindberg et al., 2014; Tobin et al., 2015b), as well as from numerical simulations (Walch et al., 2010, 2012; Seifried et al., 2013; Nordlund et al., 2014; Frimann et al., 2016a), indicating that disk formation is ubiquitous at all stages of star formation. The lack of bursting sources in the simulation can be taken as indirect support both for the necessity of disks to mediate accretion, and of the existence of disks around the most deeply embedded protostars.

5.5 SUMMARY

This paper has presented an analysis of synthetic maps of the $C^{18}O$ $J = 2-1$ line, targeting deeply embedded Class 0 and I protostars, in a large MHD simulation of a molecular cloud. The primary goal of the paper has been to establish whether measurements of the spatial distribution of gas-phase $C^{18}O$ around a sample of deeply embedded protostars, observed by Jørgensen et al. (2015), can be reproduced by the simulation. The main results of the paper are summarised as follows:

1. One-dimensional Gaussian functions are fitted to the (u, v)-data to measure the spatial extent of $C^{18}O$. Fitting two-dimensional Gaussians reveals that, on average, the minor and major axes are within 20 % of each other, indicating that the emission is mostly symmetric and in agreement with the real observations.

2. CO abundance profiles are also analysed to measure the spatial extent of gas-phase CO independently of the fitted Gaussians. The two methods agree up to a roughly constant scale factor of 2.0 ± 0.2. This shows that the (u, v)-fitting method is capable of reliably measuring the CO extents.

3. Given the adopted baseline limits of 15 kλ and 50 kλ, we find that the spatial scales between which the extent of $C^{18}O$ can be reliably measured are $1.3''$ and $4.0''$. This means that it is difficult to detect past luminosity bursts for high-luminosity sources because most emission will be at small baselines not included when measuring the extent. The adopted baseline limit of 15 kλ was chosen to avoid issues with emission from the ambient medium; however, our analysis indicates that these issues only become important at baselines <10 kλ and we therefore recommend using this as a limit when attempting to measure large extents.

4. Approximately 2 % of the systems in the simulation have $C^{18}O$ distributed over an area that is extended enough to be consistent with the central protostar having been at least a factor of five brighter at some time in the past. For the systems observed by Jørgensen et al. (2015) this fraction is approximately 50 %. Because no disks are formed in the simulation, the protostellar luminosities wary owing to variations in the infall from large scales. Our results indicate that the presence of circumstellar disks, even in the embedded stages, is a necessary component to explain the wide distribution of extents seen in the observations.

5. Even if the frequency and magnitude of episodic outbursts in the simulation are too small to explain the $C^{18}O$ observations, it still reproduces the median and scatter of the PLF. This shows that the main physical attribute in setting up the PLF is not the presence of large and frequent accretion bursts, but rather the gradual decrease in accretion rate with time.

The biggest uncertainty to the conclusions is whether the sublimation temperature of CO is subject to large source-to-source variations, which, if they are substantial, may explain most of the variations in the CO extents measured in the observations. This problem has to be investigated observationally, for example by observing the ice lines of other molecular species to see if they vary in phase with the CO ice lines. Even though the inclusion of disk physics is crucial for capturing the episodic accretion events, we note that it is equally important to ensure that the infall of material from large scales is realistic, otherwise the frequency and magnitude of the accretion bursts will not be correctly reproduced. Tentative results from high-resolution zoom-in simulations of individual protostars that include the larger scales indicate that the frequency of bursts increases once the circumstellar disk starts to become resolved (Nordlund et al., 2014). Further high-resolution numerical follow-up studies, possibly including tracer particles to be able to follow the dynamical evolution of the systems, will help in deepening our understanding of the processes at play. This paper, which explores the influence of large-scale infall on the accretion histories of protostars, is an important step towards that goal.

5.6 ACKNOWLEDGEMENTS

We are grateful to the anonymous referee for the good comments, which improved the clarity of the paper. This research was supported by a Lundbeck Foundation Group Leader Fellowship to JKJ as well as the European Research Council (ERC) under the European Union's Horizon 2020 research and innovation programme (grant agreement No 646908) through ERC Consolidator Grant "S4F". PP acknowledges support by the Spanish MINECO under project AYA2014-57134-P. TH is supported by a Sapere Aude Starting Grant from the Danish Council for Independent Research. Research at Centre for Star and Planet Formation is funded by the Danish National Research Foundation and the University of Copenhagen's programme of excellence. We acknowledge PRACE for awarding us access to the computing resource CURIE based in France at CEA for carrying out part of the simulation. Archival storage and computing nodes at the University of Copenhagen HPC centre, funded with a research grant (VKR023406) from Villum Fonden, were used for carrying out part of the simulation and the post-processing.

6

PAPER III: PROTOSTELLAR ACCRETION TRACED WITH CHEMISTRY. HIGH RESOLUTION $C^{18}O$ AND CONTINUUM OBSERVATIONS TOWARDS DEEPLY EMBEDDED PROTOSTAR IN PERSEUS

Søren Frimann[1], Jes K. Jørgensen[1], Michael M. Dunham[2], and other members of the MASSES project

[1] Centre for Star and Planet Formation, Niels Bohr Institute and Natural History Museum of Denmark, University of Copenhagen, Øster Voldgade 5-7, DK-1350 Copenhagen K, Denmark
[2] Harvard-Smithsonian Center for Astrophysics, 60 Garden Street, MS 78, Cambridge, MA 02138, USA

In preparation.

Abstract

Context. Understanding how mass is accreted onto protostars is a key question of star formation. Specifically, are the accretion rates of protostars characterised by sudden bursts and what is the influence of circumstellar disks?

Aims. The goal of the paper is to use molecule sublimation to trace the accretion history young protostars by measuring the spatial extent of gas-phase $C^{18}O$ towards a sample of deeply embedded protostars; and to find out whether a link between accretion variability and the presence of circumstellar disks can be established.

Methods. A sample of 20 embedded protostars from the Perseus molecular cloud are observed with the Submillimeter Array (SMA). The spatial extent of $C^{18}O$ emission is measured towards each object, and the current luminosity of that object is used to determine if that extent is enhanced. The SMA observations also include 1.3 mm continuum data, which we use to detect the presence of excess compact emission towards individual sources, which may indicate the presence of a circumstellar disk.

Results. We find clear evidence that several of the observed sources have enhanced $C^{18}O$ extents. We also find a clear trend that the spatial extents of the low-luminosity objects are more enhanced than their high-luminosity counterparts. The objects with enhanced $C^{18}O$ extents also have a larger probability of having an excess of compact continuum emission, indicating the presence of a circumstellar disk.

Conclusions. We interpret the enhanced $C^{18}O$ extents around the low-luminosity objects as systems that are in an intermittent stage, between accretion bursts. The high-luminosity objects in the sample may be those objects that are currently undergoing

a burst. The fact that the low-luminosity objects still show evidence of containing disks, indicates that a typical accretion burst is not sufficient to deplete the disk entirely of material.

6.1 INTRODUCTION

One of the outstanding questions of star formation is how young embedded protostars gain their mass. Specifically, are the accretion rates characterised by a smooth decline from early to late stages, or are they better characterised by intermittent bursts of high accretion? Evidence of episodic accretion in Young Stellar Objects (YSOs) include the FU Orionis objects, which are pre-main-sequence stars showing optical luminosity bursts (Herbig 1966, 1977; see Audard et al. 2014 for a recent review). Theoretically, such large outbursts can be tied to accretion instabilities in the circumstellar disk around the YSO (e.g. Bell & Lin 1994; Armitage et al. 2001; Vorobyov & Basu 2005; Zhu et al. 2009), leading to a lot of material being dumped onto the central object over a short time interval. It is not known whether deeply embedded protostars undergo sudden accretion bursts to the same degree as their older more evolved counterparts, since such searches are most easily carried out at optical and near-infrared wavelengths where the deeply embedded objects are not detected. So far, the only direct detection of a bursting deeply embedded protostar is HOPS 383, which increased its 24 μm flux by a factor of 35 between 2004 and 2008 (Safron et al., 2015).

Because of the challenges associated with the direct detection of accretion bursts in deeply embedded protostars indirect methods, capable of tracing evidence of variable accretion in the past, have to be employed. An example of this are the "knots" or "bullets" observed in the outflows of some protostars. Such knots are thought to trace dense regions of the outflow and can be traced back to variations in the accretion rate. Measurements of knot velocities as well as the distance between individual knots indicate that the time-scales between episodic outbursts range from approximately 100 yr to 1000 yr (e.g. Bachiller et al. 1990, 1991; Lee et al. 2009; Arce et al. 2013; Plunkett et al. 2015).

Another option is to use chemistry to trace the protostellar accretion histories. Various molecules, normally frozen-out onto dust grains at low temperatures, will move into the gas-phase during an accretion burst because of the increased heating from the central protostar. Following the end of the accretion burst these molecules may remain in the gas-phase for several thousand years, depending on the density of the envelope (Rodgers & Charnley, 2003), before they are freeze back out onto the dust grains. Observations of this out-of-equilibrium situation may be used as a method to detect past luminosity bursts (e.g. Visser & Bergin 2012; Vorobyov et al. 2013; Visser et al. 2015). It is also possible to get an idea of the accretion history of a dust grain by observing absorption bands of pure CO_2 ice, which would indicate significant thermal processing (e.g. Kim et al. 2012; Poteet et al. 2013). It is, however, not generally possible to determine if the thermal processing occurred before or after the onset of the core-collapse phase.

One of the best examples to date of using chemical tracers to detect evidence for a past accretion burst is the case of the deeply embedded protostar IRAS 15398–3359, which was observed with the Atacama Large Millimeter Array by Jørgensen et al. (2013), and was found to have HCO^+ distributed in a ring-like structure around the peak of the continuum emission. The authors conclude that the best explanation for the lack of HCO^+ at small scales is for it to have been destroyed by gas-phase H_2O, which will only be possible if the protostar has had its luminosity increased by roughly two orders of magnitude within the past 100 yr to 1000 yr. This would indicate that the H_2O ice, which sublimated from the dust grains during the accretion burst, will still be in the process of refreezing.

An alternative method is to use spatially resolved observations of individual protostars and measure the spatial extent of CO or some other molecule in the envelope. If the molecule is detected over larger spatial scales than can be explained by the current protostellar luminosity, then this may indicate that the luminosity of the protostar has been larger in the past, and that the molecule is still in the process of refreezing. Such an approach was adopted by Jørgensen et al. (2015), who measured the spatial extent of $C^{18}O$ in a sample of 16 deeply embedded protostars, and found ≈50 % to have $C^{18}O$ distributed over a larger area than could be explained by the current luminosity. Using a rerun of the numerical simulation presented by Padoan et al. (2014), Frimann et al. (2016b) calculated synthetic $C^{18}O$ maps of a large sample of simulated protostars to measure the spatial extents of $C^{18}O$ in the same fashion as was done by Jørgensen et al. (2015). They found the method to be capable of accurately measuring the physical extent of gas-phase CO surrounding the protostar, but also found that the measured $C^{18}O$ extents of the synthetic maps could not reproduce the spread of $C^{18}O$ extents measured in the real observations. The protostars in the Padoan et al. (2014) simulation have variable accretion rates owing to variations in the infall of material from large scales and is notably capable of reproducing the median and spread of the observed distribution of protostellar luminosities. The simulation does not, however, have sufficient resolution to include disk physics, which indicate that disks are necessary to reproduce episodic accretion bursts and to reproduce the spread of $C^{18}O$ extents reported by Jørgensen et al. (2015).

This paper presents maps of $C^{18}O$ and continuum emission observed towards 20 embedded objects in the Perseus molecular cloud (d = 235 pc), with the goal of finding evidence for past accretion bursts and establishing a possible link to the presence of disks around these objects. The key advantages of this sample relative to the one presented in Jørgensen et al. (2015) is that all the protostars are from Perseus meaning that distance uncertainties do not play as big a role, and that the observations are all from the same program, giving a more uniform sample. The observations are from the large survey "Mass Assembly of Stellar Systems and their Evolution with the SMA" (MASSES; Principal Investigator: Michael M. Dunham) undertaken with the Submillimeter Array (SMA). This survey targets all known embedded protostars in Perseus, including the 66 sources identified by the Spitzer Space Telescope (Enoch et al., 2009) and seven candidate first hydrostatic cores. The main science goals of the MASSES survey include obtaining a better understanding of the link between cores and their fragmentation into multiple systems, the role of disks in transferring mass from the cores and onto the protostars, and the role of molecular outflows in regulating the accretion processes. First results from MASSES, studying the connection between multiplicity and core kinematics of the multiple system L1448 N, were presented by Lee et al. (2015).

6.2 OBSERVATIONS

The observations presented here were carried out with the SMA (Ho et al., 2004), which is a submillimetre and millimetre interferometer consisting of eight 6 m antennae situated on the summit of Mauna Kea, Hawaii, at an altitude of 4100 m. The data were taken at a frequency of 230 GHz (1.3 mm) and include observations of the $C^{18}O$ J = 2–1 transition and dust continuum. All of the data were taken at the subcompact configuration, which typically gives a baseline range of roughly 5 kλ to 50 kλ. For a few targets we also have $C^{18}O$ observations from the extended configuration (typical baseline coverage of 20 kλ to 150 kλ). The extended data are concatenated with the subcompact data whenever available. Table 6.1 lists the objects in the observed sample along with Spitzer positions, luminosities, and bolometric temperatures (Myers & Ladd, 1993). The data were reduced and calibrated with the MIR package[1] using standard calibration procedures. Imaging and analysis was done using Miriad (Sault et al., 1995). As a complement to the interferometric continuum observations, we also include 850 μm single-dish continuum data for the sources in the sample, obtained from the James Clerk Maxwell Telescope Submillimetre-Common Bolometer Array (JCMT/SCUBA) legacy catalogue (Di Francesco et al., 2008).

Figure 6.1 shows $C^{18}O$ spectra of the observed sources. The spectra are extracted towards the peak of the $C^{18}O$ emission around each

1 https://www.cfa.harvard.edu/~cqi/mircook.html

Table 6.1: Sample of sources.

Source[a]		α_{J2000}[b]	δ_{J2000}[b]	L_{bol} ($L_\odot$)	T_{bol} (K)	Reference[c]	Configuration[d]
Per 1	HH 211	03h43m56.5s	32d00m52.9s	1.8 ± 0.1	27 ± 1	Sadavoy et al. (2014)	subc
Per 2	IRAS 03292	03h32m18.0s	30d49m47.6s	0.90 ± 0.07	27 ± 1	Sadavoy et al. (2014)	subc
Per 5	IRAS 03282	03h31m21.0s	30d45m30.2s	1.3 ± 0.1	32 ± 2	Sadavoy et al. (2014)	subc+ext
Per 11	IC348-MMS	03h43m56.9s	32d03m04.6s	1.5 ± 0.1	30 ± 2	Sadavoy et al. (2014)	subc
Per 12	IRAS 4A	03h29m10.5s	31d13m31.0s	7.0 ± 0.7	29 ± 2	Sadavoy et al. (2014)	subc
Per 13	IRAS 4B	03h29m12.0s	31d13m01.5s	4.0 ± 0.3	28 ± 1	Sadavoy et al. (2014)	subc+ext
Per 14	IRAS 4C	03h29m13.5s	31d13m58.0s	0.70 ± 0.08	31 ± 2	Sadavoy et al. (2014)	subc
Per 16		03h43m51.0s	32d03m24.8s	0.40 ± 0.04	39 ± 2	Sadavoy et al. (2014)	subc
Per 18		03h29m11.3s	31d18m31.3s	3.6 ± 0.5	46 ± 3	Sadavoy et al. (2014)	subc
Per 19		03h29m23.5s	31d33m29.5s	0.36 ± 0.05	60 ± 3	Enoch et al. (2009)	subc
Per 21		03h29m10.7s	31d18m20.5s	3.6 ± 0.5	46 ± 3	Sadavoy et al. (2014)	subc
Per 22	L1448 IRS2	03h25m22.3s	30d45m14.0s	3.6 ± 0.5	43 ± 2	Sadavoy et al. (2014)	subc+ext
Per 26	L1448 C	03h25m38.8s	30d44m06.3s	9.2 ± 1.3	47 ± 2	Sadavoy et al. (2014)	subc
Per 27	IRAS 2A	03h28m55.6s	31d14m36.6s	19.0 ± 0.4	69 ± 1	Enoch et al. (2009)	subc+ext
Per 28		03h43m51.0s	32d03m07.9s	0.70 ± 0.08	45 ± 2	Sadavoy et al. (2014)	subc
Per 29	B1-c	03h33m17.9s	31d09m32.0s	3.7 ± 0.4	48 ± 1	Sadavoy et al. (2014)	subc
Per 33	L1448 N	03h25m36.5s	30d45m22.3s	8.3 ± 0.8	57 ± 3	Sadavoy et al. (2014)	subc
Per 35	IRAS 1	03h28m37.1s	31d13m30.7s	9.1 ± 0.3	103 ± 26	Enoch et al. (2009)	subc
Per 53	B5 IRS1	03h47m41.6s	32d51m43.9s	4.7 ± 0.9	287 ± 8	Enoch et al. (2009)	subc
Per 61		03h44m21.3s	31d59m32.6s	0.24 ± 0.16	371 ± 107	Enoch et al. (2009)	subc

Notes. [a] The first column gives the names of the observed targets following the naming scheme from Enoch et al. (2009). The second column gives some of the more well-known identifiers of the same objects. [b] Spitzer positions from the c2d survey (Evans et al., 2009). [c] Luminosity and T_{bol} reference. [d] Array configuration. Subc = subcompact; ext = extended.

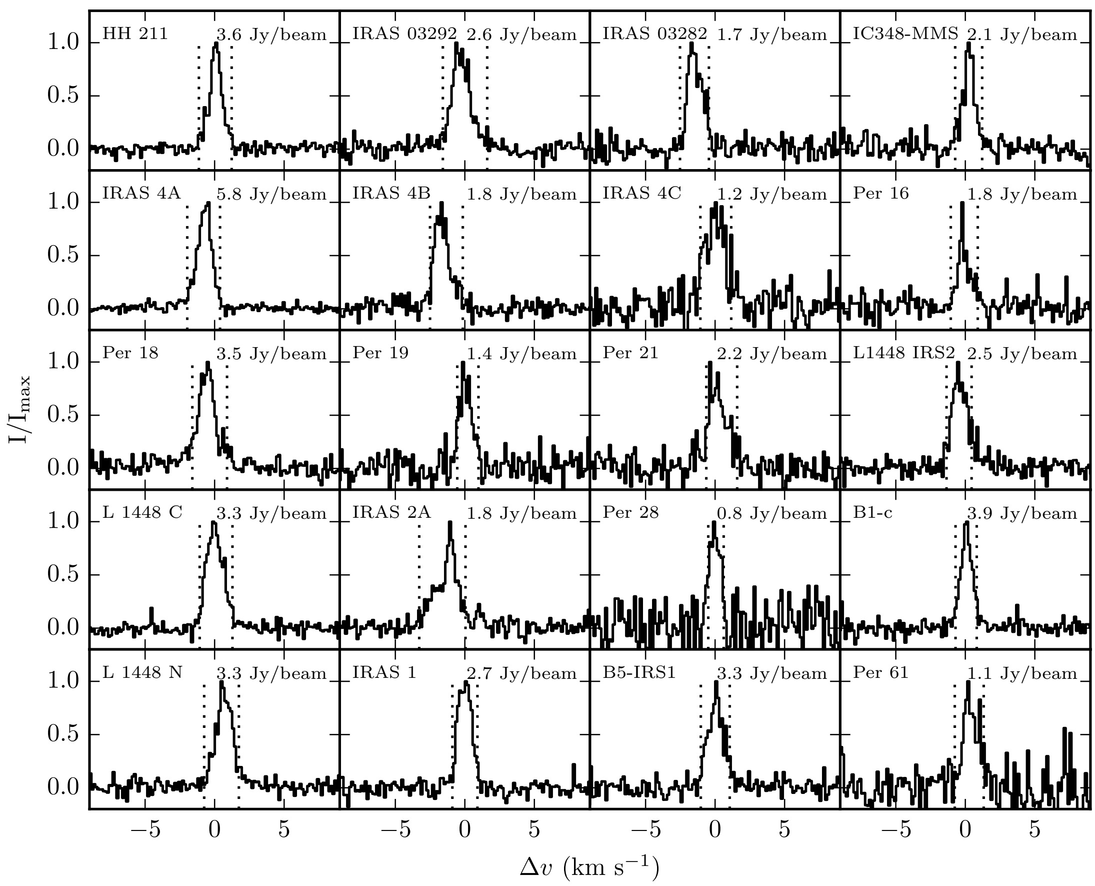

Figure 6.1: $C^{18}O$ J = 2–1 spectra towards the peak of its integrated emission for each of the sources in the sample. The dotted lines indicate the integration interval for calculating the zero moment maps shown in Fig. 6.2. The value in the top right corner of each panel is the peak emission, I_{max}, of the line.

source, and the dotted lines in the figures indicate the interval over which the emission is integrated to produce the zero moment maps shown in Fig. 6.2. Figure 6.2 also shows continuum maps of the observed sources. Generally, the emission is observed to be relatively compact towards the individual sources, with some evidence of low surface brightness extended emission toward some sources.

The red crosses in Fig. 6.2 indicate the Spitzer position of the sources, as identified by the Cores to Disks (c2d) survey (Evans et al., 2009). In most cases these match the peak positions of both $C^{18}O$ and continuum emission well, but for HH 211, IRAS 4B, and L1448 N there is a noticeable offset. For both HH 211 and IRAS 4B, the Spitzer position is in the direction of the outflow (Jørgensen et al., 2007a; Lee et al., 2009), indicating that these offsets may be due to shocked emission in the outflow being misidentified as the source emission. For L1448 N, which is also known as L1448 IRS3 by some authors, the confusion could be one of two things. L1448 N is known to be a multiple sys-

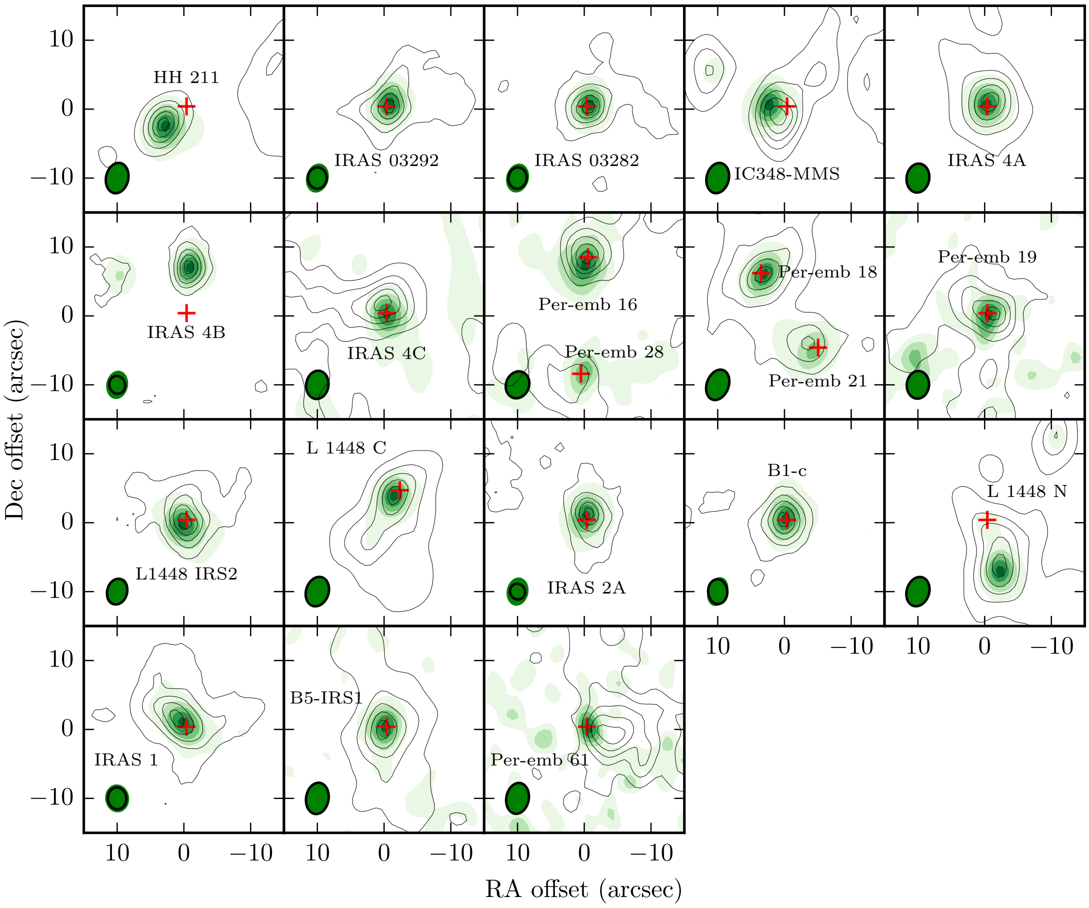

Figure 6.2: Maps of the $C^{18}O$ J = 2–1 line emission (black contours) and 1.3 mm continuum emission (green shaded contours). Contours are drawn at 10 %, 30 %, 50 %, 70 %, and 90 % of the peak emission. The red crosses indicate the location of the Spitzer identified source.

tems composed of three sources A, B, and NW (Lee et al., 2015). The emission in Fig. 6.2 primarily traces L1448 N-B, while the Spitzer position is close to L1448 N-A. The Spitzer position could, however, also trace the outflow of the A-source.

Looking at the maps in Fig. 6.2 it is clear that both L1448 C and L1448 N are associated with other sources, that are only marginally resolved in the $C^{18}O$ maps, and may therefore pose problems when measuring them later on. Additionally, several of the sources are also known to be associated with close companions not resolved in these observations, probably indicating proto-binary systems. This is true of HH 211 (Lee et al., 2009), although its companion is very faint; IRAS 4A (e.g. Jørgensen et al. 2007a); IRAS 2A (Tobin et al., 2015a); and L1448 N whose B-source, which is the one traced in this study, is known to be a proto binary system (Lee et al., 2015).

The addition of data from the extended configuration of SMA is not generally seen to alter the $C^{18}O$ maps. This is related to the fact that $C^{18}O$ is typically not seen at baselines $\gtrsim 50\,k\lambda$, indicating that $C^{18}O$ is typically spread out over spatial scales $\gtrsim 2''$. Although $C^{18}O$ is not typically detected on the longer baselines, the addition of extended data is still advantageous as it provides additional baselines at the intermediate ranges, thereby improving the signal.

6.3 RESULTS

6.3.1 *$C^{18}O$ observations*

To measure the spatial extent of gas-phase $C^{18}O$, two-dimensional Gaussians are fitted directly to the (u, v)-data using the `uvfit` routine in Miriad. We follow Jørgensen et al. (2015) and disregard baselines smaller than $15\,k\lambda$ (corresponding to spatial extents larger than $\approx 6''$) to avoid possible issues with external heating from the Interstellar Radiation Field (ISRF) or low-density pre-depletion regions where CO has not yet frozen out (Jørgensen et al., 2005b). The fits to the individual objects are shown in Fig. 6.3, and the results are listed in Table 6.2. Five out of 20 protostars in the sample do not have enough signal to measure a reliable spatial extent of CO, and are therefore excluded from Table 6.2.

The measured extents listed in Table 6.2 are the geometric means between the minor and major axes of the fitted Gaussians ($\theta_{avg} = \sqrt{\theta_{maj} \times \theta_{min}}$). We have also fitted one-dimensional Gaussian functions to all of the objects, and the results generally agree within the statistical uncertainties reported by `uvfit`. We fit two-dimensional Gaussians to get a feeling for the asymmetry of the CO emission, which we quantify in the table by the ratio between the major and minor axes of the fitted Gaussians. Most of the objects are consistent with symmetric emission, and only four of the objects have a value of $\theta_{maj}/\theta_{min}$ above 1.5.

Figure 6.4 shows the measured extents vs. protostellar luminosity for the protostars in our sample (blue crosses) along with the measurements for those protostars in the Jørgensen et al. (2015) sample that are also in Perseus (red dots). Six of the sources are present in both samples, and they have been joined by black lines in the figure for easy identification. There is some discrepancy between the measurements in the two samples, especially for L1448 IRS2 where the spatial extent measured by Jørgensen et al. differ from ours by $2.9''$. Two other sources present in both samples differ by roughly $1.5''$ (IRAS 4B and L1448 C), while the rest of the measurements agree within $1''$. While the disagreement for L1448 IRS2 is extreme, and has to be investigated further, for the rest we find that it is within accept-

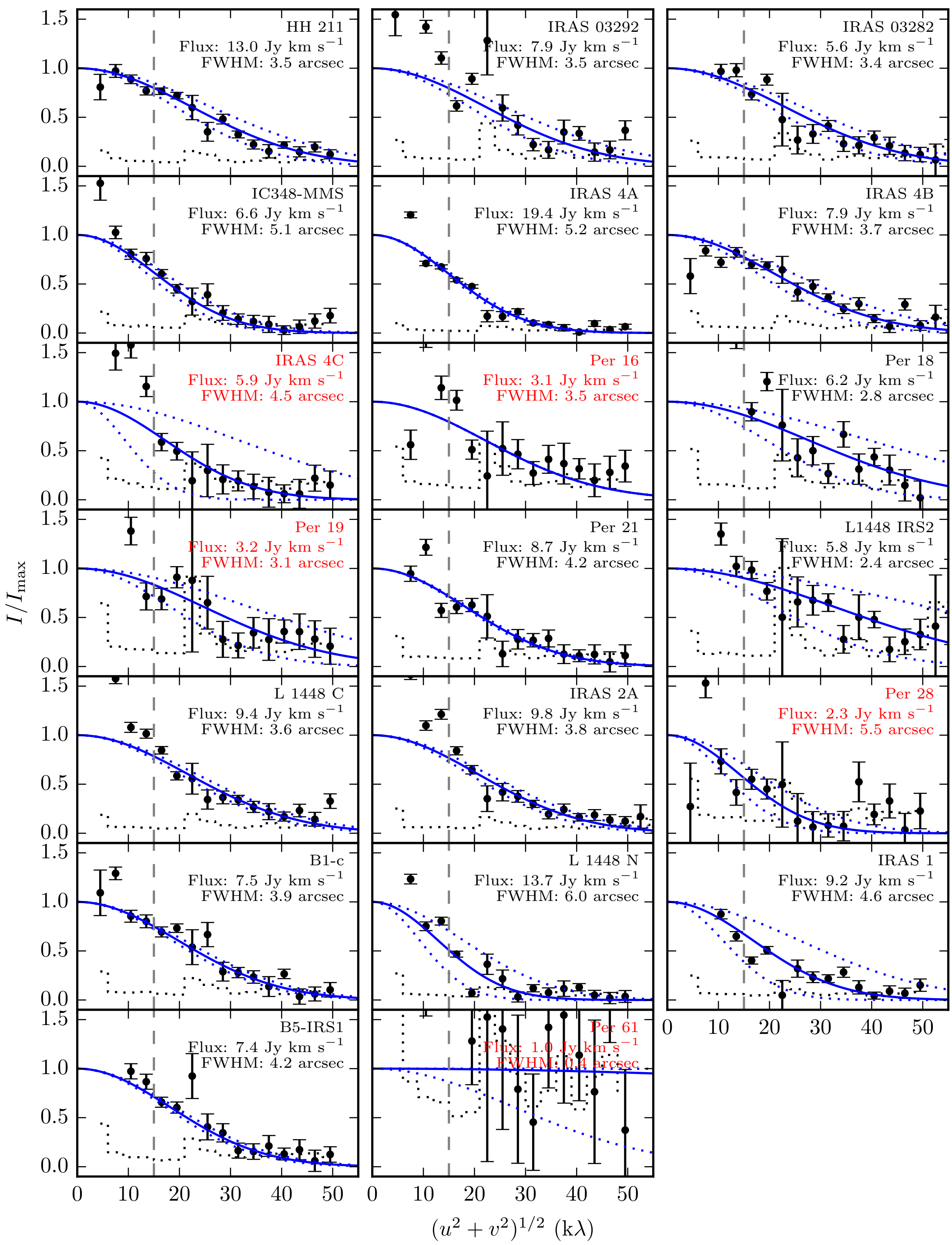

Figure 6.3: (u, v)-amplitude plots of the sources in the observed sample. The solid blue line is the result of the two-dimensional Gaussian fit with the average FWHM representing the extent. The blue dotted lines show the extent of the minor and major axes of the fit. The fluxes of the plots have been scaled to the peak flux of the Gaussian fit, whose value is printed in the upper right of each panel. The grey dashed line indicate the 15 kλ cut-off which indicates the lower-limit of the fit. Those fits that have been excluded are shown in red.

Table 6.2: Results. The ratio in the last column is between the compact flux, $F_{1.3\,mm}(50\,k\lambda)$, and the extended flux, $S_{1.3\,mm}(15'')$, where the extended flux has been rescaled from 850 μm to 1.3 mm (see text for details).

Source	L_{bol} ($L_\odot$)	Extent (arcsec)	L_{CO}/L_{cur}	$\theta_{major}/\theta_{minor}$	$F_{1.3\,mm}(50\,k\lambda)$ (mJy)	$S_{850-m}(15'')$ (Jy beam^{-1})	Ratio
HH 211	1.8 ± 0.1	3.5 ± 0.1	10.1 ± 0.7	1.4 ± 0.1	115	2.18	0.15
IRAS 03292	0.90 ± 0.07	3.5 ± 0.3	20.5 ± 2.9	1.4 ± 0.2	415	2.50	0.48
IRAS 03282	1.3 ± 0.1	3.4 ± 0.2	13.2 ± 1.5	1.3 ± 0.2	207	1.30	0.46
IC348-MMS	1.5 ± 0.1	5.1 ± 0.6	25.2 ± 4.7	1.3 ± 0.3	203	1.72	0.34
IRAS 4A	7.0 ± 0.7	5.2 ± 0.3	5.6 ± 0.6	1.1 ± 0.1	1690	11.45	0.43
IRAS 4B	4.0 ± 0.3	3.7 ± 0.2	5.2 ± 0.5	1.4 ± 0.1	725	5.46	0.38
IRAS 4C	0.70 ± 0.08	...	...	...	79	1.18	0.19
Per 16	0.40 ± 0.04	...	...	...	12	0.71	...
Per 18	3.6 ± 0.5	2.8 ± 0.4	3.3 ± 0.7	2.0 ± 0.5	117	1.85	...
Per 19	0.36 ± 0.05	...	...	...	10	0.46	0.07
Per 21	3.6 ± 0.5	4.2 ± 0.3	7.4 ± 1.1	1.1 ± 0.2	44	1.85	...
L1448 IRS2	3.6 ± 0.5	2.4 ± 0.5	2.4 ± 0.8	2.4 ± 1.0	75	1.41	0.15
L 1448 C	9.2 ± 1.3	3.6 ± 0.2	2.1 ± 0.3	1.2 ± 0.1	169	2.23	0.22
IRAS 2A	19.0 ± 0.4	3.8 ± 0.2	1.1 ± 0.1	1.2 ± 0.1	245	3.53	0.20
Per 28	0.70 ± 0.08	...	...	...	8	0.71	...
B1-c	3.7 ± 0.4	3.9 ± 0.2	6.2 ± 0.8	1.1 ± 0.1	132	2.60	0.15
L 1448 N	8.3 ± 0.8	6.0 ± 0.4	6.3 ± 0.7	1.9 ± 0.2	513	5.46	0.27
IRAS 1	9.1 ± 0.3	4.6 ± 0.4	3.4 ± 0.4	2.4 ± 0.4	36	0.86	0.12
B5-IRS1	4.7 ± 0.9	4.2 ± 0.3	5.7 ± 1.1	1.1 ± 0.2	25	0.61	0.12
Per 61	0.24 ± 0.16	...	...	...	10	0.21	0.13

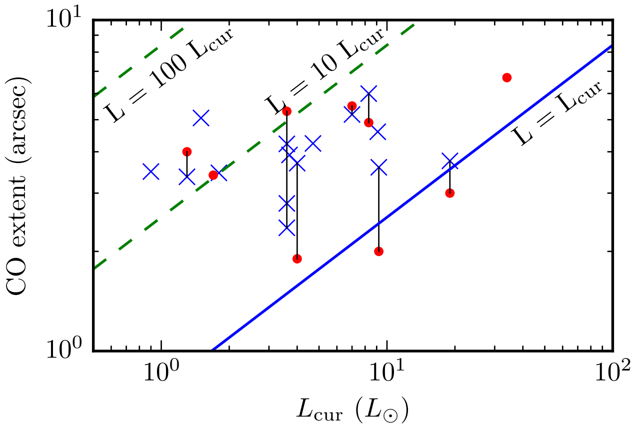

Figure 6.4: Measured spatial extent of $C^{18}O$ vs. current luminosity for the sources observed in this study (blue crosses), and for the Perseus sources measured by Jørgensen et al. (2015) (red dots). Sources that are in both samples are joined by a black line. The blue solid line represents the predicted CO extent calculated from Eq. (6.1).

able limits. It does however indicate that the typical $0.5''$ statistical uncertainty reported by `uvfit` is too small.

In the absence of any accretion variability we would expect the measurements in Fig. 6.4 to roughly follow the blue line, which is the expected extent for a spherically symmetric one solar-mass envelope with a power law density profile, $\rho \propto r^{-p}$, with $p = 1.5$ (Jørgensen et al., 2015; Frimann et al., 2016b). This line also assumes that the sublimation temperature of CO is 30 K (Noble et al., 2012). The line is described by the equation

$$\text{Extent} = 180\,\text{AU}\left(\frac{d}{1\,\text{pc}}\right)^{-1}\left(\frac{L}{1\,L_\odot}\right)^{0.52}\ \text{(arcsec)}, \tag{6.1}$$

where d is the distance to the source. Looking at the measurements in the figure it is clear that the measurements do not, in general, follow the line with the lowest extents measured in the sample having a value of roughly $2.5''$. It is natural to suspect that this could be an indication of an instrumental bias of the interferometer, which, because of the lack of long baselines, might not be able to measure spatial extents shorter than $\approx 3''$. Looking at the individual fits in Fig. 6.3 it is not possible reconcile the measurements with spatial extents significantly below what is already measured. Also, tests run on synthetic data by Frimann et al. (2016b) indicate that, for a baseline coverage up to 50 kλ, it should be possible to measure spatial extents down to roughly $1.3''$. Finally, the four sources in the sample with luminosities $< 2\,L_\odot$ (HH 211, IRAS 03292, IRAS 03282, and IC348-MMS), that are simultaneously some of the sources with the largest enhancements, are all relatively isolated objects, with no other sources nearby enough that the emission can be confused, and the spatial extents ar-

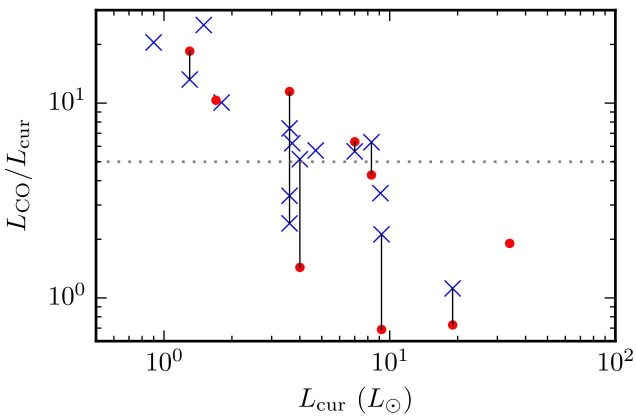

Figure 6.5: L_{CO}/L_{cur} vs. luminosity. As in Fig. 6.4 blue crosses indicate measurements of the sources analysed in this study, while red dots are the measurements of Jørgensen et al. (2015). The grey dotted line indicate $L_{CO}/L_{cur} = 5$ above which the measured extent is judged to be enhanced relative to the current luminosity.

bitrarily enhanced. We therefore conclude that the measurements of the spatial extents are real, and not an instrumental effect.

Using Eq. (6.1) as a reference it is possible to estimate the luminosity, L_{CO}, needed to produce the measured extent of CO. By taking the ratio, L_{CO}/L_{cur}, the magnitude of the luminosity burst can therefore be estimated. Figure 6.5 shows this ratio as function of luminosity. There is a clear downward trend of L_{CO}/L_{cur} with luminosity, indicating that the higher luminosity sources show less evidence of enhanced accretion in the past relative to the lower luminosity sources. Allowing for uncertainties due to measurements and calibrations we do not consider ratios <5 to be extended. Using this as a boundary ten out of 15 sources show evidence for enhanced accretion in the past. This is somewhat more than the approximately 50 % reported by Jørgensen et al. (2015), however, several of the sources in the sample have measured ratios that are only just above 5. Added together with the low-number statistics we therefore conclude that these results are in consistent with those of Jørgensen et al..

6.3.2 *Continuum observations*

Given the resolution of the data it is not possible to unambiguously detect circumstellar disks, as this requires the detection of Keplerian rotation. Instead we can use the continuum observations to determine if there is a presence of excess compact emission towards the individual sources, which might indicate the presence of a disk (Looney et al., 2000; Harvey et al., 2003; Jørgensen et al., 2005a, 2009; Enoch et al., 2011). To measure the compact flux we fitted point sources to the SMA continuum data at baseline lengths of 50 kλ. The resulting

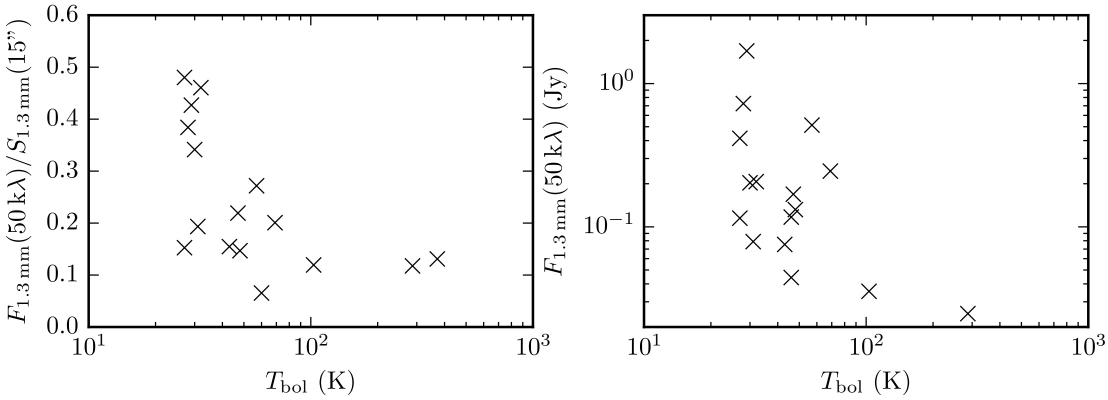

Figure 6.6: Left: Flux ratio between the compact interferometric flux and the single-dish extended flux vs. T_bol. The single-dish flux has been rescaled from 850 µm to 1.3 mm using $F_\nu \propto \nu^\alpha$ with $\alpha = 2.5$. Right: Interferometric compact flux vs. T_bol.

fluxes from these fits are listed in Table 6.2 and plotted in the right panel of Fig. 6.6. The figure shows a large spread in the measured fluxes, which is consistent with the results of the continuum survey of Jørgensen et al. (2009).

The objects are embedded in massive envelopes, which will also affect the compact fluxes. We use large-scale 850 µm single-dish observations from the JCMT/SCUBA legacy catalogue by Di Francesco et al. (2008) to get an estimate of the envelope emission. The relative importance of the compact emission can therefore be determined by calculating the ratio between the compact and extended fluxes. This is shown in the left panel of Fig. 6.6, where the SCUBA 850 µm flux has been rescaled to 1.3 mm by using $F_\nu \propto \nu^\alpha$ where we have used a value of 2.5 for α (Jørgensen et al., 2007a). Per 16 & Per 28 and Per 18 & Per 21 are so close together that they cannot be distinguished in the single-dish maps, and they are therefore omitted when calculating the flux ratios. Both L1448 C and L1448 N are also clearly part of multiple systems, but are kept in the because we only detect compact continuum emission from one source in each case. Emission from the envelope is only expected to influence the fluxes measured at 50 kλ of the order of a few percent (e.g. Jørgensen et al. 2009), because the large-scale emission is filtered out by the interferometer. Therefore, the higher the ratio between the compact flux measured at 50 kλ and the extended single-dish flux the more likely it is that the system contains some compact component, which may be a disk. This picture is supported by Frimann et al. (2016a), who analysed synthetic observations of a large-scale simulation of a molecular cloud, and found that disks may be present at all flux ratios, but that they have a larger probability of being found at high flux ratios.

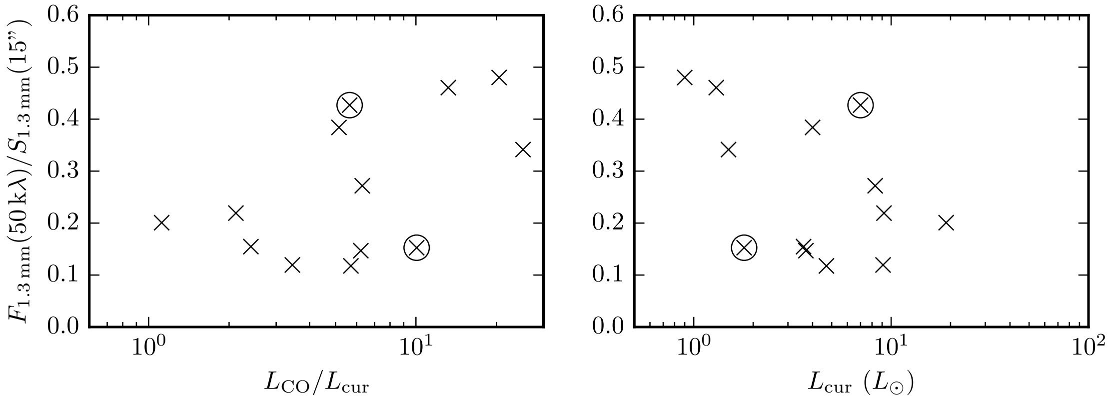

Figure 6.7: Top row of panels: Flux ratio vs. L_{CO}/L_{cur} and L_{cur}. Middle row of panels: Same as top row, but compact flux, $F_{1.3\,mm}(50\,k\lambda)$, in place of flux ratio. Bottom row of panels: Same but with the extended flux, $S_{850—m}(15'')$. The two circles in each panel mark the objects HH 211 and IRAS 4A.

6.4 DISCUSSION AND CONCLUSIONS

Figure 6.5 summarises the main finding of the paper, namely that the low-luminosity objects are more likely to have their CO distributed over a large scale relative to their current luminosity, than the higher luminosity objects. An explanation for this could be that the low-luminosity objects are more likely to be in an intermittent stage between bursts, while the higher luminosity objects are more likely to be those that are currently themselves undergoing a luminosity burst. We have already shown in Sect. 6.3.1 that the relatively large extents measured towards the low-luminosity objects are real and not a baseline bias. Similarly, one could argue that extended $C^{18}O$ emission of the high-luminosity sources may not be detectable because of the lower baseline limit of 15 kλ imposed on the fits. While it is true that it is not possible to measure extents larger than $\approx 6''$ with this baseline limit, as long as there is still significant emission at baselines longer than 15 kλ, we do not expect these measurements to be far from reality. For systems that have a measured extent close to the theoretical limit of $6''$ it may however indicate that the measurements of those systems are lower limits.

The top row of panels in Fig. 6.7 shows the ratio between compact and extended fluxes vs. L_{CO}/L_{cur} and L_{cur}. There appears to be a weak positive correlation between flux ratio and L_{CO}/L_{cur}. In particular, all objects with $L_{CO}/L_{cur} < 5$ are seen to have a flux ratio $\lesssim 0.2$, while all objects with $L_{CO}/L_{cur} > 10$ have a flux ratio > 0.3; in-between the picture is more muddled. Similarly, there appears to be a weak negative correlation between the flux ratio and the luminosity, especially if the two objects marked with circles, HH 211 and IRAS 4A, are disregarded (these are the same objects in both panels). IRAS 4A is known to be double system consisting of a NW and SE component. Using higher resolution observations than those presented here Jørgensen et al. (2007a) found that the $C^{18}O$ emission is centred around the NW component. Jørgensen et al. (2007a) also measured the 1.3 mm continuum flux of the two components, which sums up to 1690 mJy – identical with the value reported in Table 6.2. The continuum flux of the NW component alone is 590 mJy; substituting this value for the compact flux gives a new flux ratio of 0.15, almost a factor of three lower than the 0.43 value reported in Table 6.2, which brings the point closer to the others in both top panels of Fig. 6.7. HH 211 is known to contain a flattened structure seen edge-on, possibly tracing a Keplerian disk (Lee et al., 2009). Due to shielding in the mid-plane this means that the reported luminosity of $1.8\,L_\odot$ is most probably underestimated. Analysing synthetic SEDs from a large simulation of a molecular cloud Frimann et al. (2016a) found that the luminosity of an object increases, on average, by a factor of 2.5 when going from and edge-on to a face-on viewing angle towards circumstellar disks. Increasing the luminosity would simultaneously decrease L_{CO}/L_{cur}.

The systems showing the highest values of L_{CO}/L_{cur} are simultaneously the systems with the highest flux ratios. If we assume for a moment that a high flux ratio indicates the presence of a circumstellar disk, then this suggests that these objects contain massive disks. Superficially, this would appear to be inconsistent with the idea that these objects are in-between bursts. However, we do not expect all the disk material to be accreted onto the protostar in a single episodic outburst because that would contradict the evidence from outflows, which indicate that a protostar may undergo several bursts within time intervals of a few hundred years. Indeed, several of the objects in this sample are examples of objects with clumpy outflows (L1448 N Bachiller et al. 1990; IRAS 03282 (Bachiller et al., 1991); and HH 211 Lee et al. 2009). One counter-example of this is the embedded protostar IRAS 15398–3359, which shows evidence of having recently gone through an accretion burst that increased its luminosity by two orders of magnitude, but which simultaneously does not show any evidence of a disk or any other compact component (Jørgensen et al., 2013). However, this might be reconciled by the fact that an accretion burst of ~100 is much larger than any of the bursts measured here, which increases the likelihood that the burst was massive enough to deplete all or most of the circumstellar disk.

6.5 ACKNOWLEDGEMENTS

This research was supported by a Lundbeck Foundation Group Leader Fellowship to JKJ as well as the European Research Council (ERC) under the European Union's Horizon 2020 research and innovation programme (grant agreement No 646908) through ERC Consolidator

Grant "S4F". Research at Centre for Star and Planet Formation is funded by the Danish National Research Foundation and the University of Copenhagen's programme of excellence.

BIBLIOGRAPHY

Adams, F. C., Lada, C. J., & Shu, F. H. 1987, ApJ, 312, 788

Aikawa, Y., Umebayashi, T., Nakano, T., & Miyama, S. M. 1997, ApJ, 486, L51

Allen, A., Li, Z.-Y., & Shu, F. H. 2003, ApJ, 599, 363

ALMA Partnership, Brogan, C. L., Pérez, L. M., et al. 2015, ApJ, 808, L3

André, P., Di Francesco, J., Ward-Thompson, D., et al. 2014, in Protostars and Planets VI, ed. H. Beuther, R. S. Klessen, C. P. Dullemond, & T. Henning (Tuscon: University of Arizona Press), 27–51

André, P., Men'shchikov, A., Bontemps, S., et al. 2010, A&A, 518, L102

André, P., Ward-Thompson, D., & Barsony, M. 1993, ApJ, 406, 122

Arce, H. G., Mardones, D., Corder, S. A., et al. 2013, ApJ, 774, 39

Armitage, P. J. 2011, ARA&A, 49

Armitage, P. J., Livio, M., & Pringle, J. E. 2001, MNRAS, 324, 705

Audard, M., Ábrahám, P., Dunham, M. M., et al. 2014, in Protostars and Planets VI, ed. H. Beuther, R. S. Klessen, C. P. Dullemond, & T. Henning (Tuscon: University of Arizona Press), 387–410

Bachiller, R., Martin-Pintado, J., & Planesas, P. 1991, A&A, 251, 639

Bachiller, R., Martin-Pintado, J., Tafalla, M., Cernicharo, J., & Lazareff, B. 1990, A&A, 231, 174

Bate, M. R. 2012, MNRAS, 419, 3115

Bate, M. R., Bonnell, I. A., & Price, N. M. 1995, MNRAS, 277, 362

Bell, K. R. & Lin, D. N. C. 1994, ApJ, 427, 987

Belloche, A. 2013, in Role and Mechanisms of Angular Momentum Transport During the Formation and Early Evolution of Stars, 62, 25

Bertoldi, F. & McKee, C. F. 1992, ApJ, 395, 140

Bisschop, S. E., Fraser, H. J., Oberg, K. I., van Dishoeck, E. F., & Schlemmer, S. 2006, Astronomy and Astrophysics, 449, 1297

Bjorkman, J. E. & Wood, K. 2001, ApJ, 554, 615

Black, J. H. 1994, in The First Symposium on the Infrared Cirrus and Diffuse Interstellar Clouds. ASP Conference Series, 58, 355

Blandford, R. D. & Payne, D. G. 1982, MNRAS, 199, 883

Bohlin, R. C., Savage, B. D., & Drake, J. F. 1978, ApJ, 224, 132

Brinch, C., Crapsi, A., Hogerheijde, M. R., & Jørgensen, J. K. 2007a, A&A, 461, 1037

Brinch, C., Crapsi, A., Jørgensen, J. K., Hogerheijde, M. R., & Hill, T. 2007b, A&A, 475, 915

Brinch, C. & Hogerheijde, M. R. 2010, A&A, 523, 25

Brinch, C., Hogerheijde, M. R., & Richling, S. 2008, A&A, 489, 607

Chabrier, G. 2003, PASP, 115, 763

Chen, H., Myers, P. C., Ladd, E. F., & Wood, D. O. S. 1995, ApJ, 445, 377

Chiang, H.-F., Looney, L. W., Tassis, K., Mundy, L. G., & Mouschovias, T. C. 2008, ApJ, 680, 474

Collings, M. P., Dever, J. W., Fraser, H. J., McCoustra, M. R. S., & Williams, D. A. 2003, ApJ, 583, 1058

Commerçon, B., Launhardt, R., Dullemond, C. P., & Henning, T. 2012a, A&A, 545, A98

Commerçon, B., Levrier, F., Maury, A. J., Henning, T., & Launhardt, R. 2012b, A&A, 548, 39

Costigan, G., Scholz, A., Stelzer, B., et al. 2012, MNRAS, 427, 1344

Costigan, G., Vink, J. S., Scholz, A., Ray, T., & Testi, L. 2014, MNRAS, 440, 3444

D'Antona, F. & Mazzitelli, I. 1997, Mem. Soc. Astron. Italiana, 68, 807

de Geus, E. J., de Zeeuw, P. T., & Lub, J. 1989, A&A, 216, 44

Di Francesco, J., Johnstone, D., Kirk, H., MacKenzie, T., & Ledwosinska, E. 2008, ApJS, 175, 277

Dullemond, C. P. 2012, Radiative Transfer in Astrophysics Theory, Numerical Methods and Applications

Dullemond, C. P. & Dominik, C. 2004, A&A, 417, 159

Dunham, M. M., Arce, H. G., Allen, L. E., et al. 2013, AJ, 145, 94

Dunham, M. M., Evans, N. J., Terebey, S., Dullemond, C. P., & Young, C. H. 2010, ApJ, 710, 470

Dunham, M. M., Stutz, A. M., Allen, L. E., et al. 2014, in Protostars and Planets VI, ed. H. Beuther, R. S. Klessen, C. P. Dullemond, & T. Henning (Tuscon: University of Arizona Press), 195–218

Dunham, M. M. & Vorobyov, E. I. 2012, ApJ, 747, 52

Dzib, S., Loinard, L., Mioduszewski, A. J., et al. 2010, ApJ, 718, 610

Eisner, J. A., Hillenbrand, L. A., Carpenter, J. M., & Wolf, S. 2005, ApJ, 635, 396

Enoch, M. L., Corder, S., Duchêne, G., et al. 2011, ApJS, 195, 21

Enoch, M. L., Evans, N. J., Sargent, A. I., & Glenn, J. 2009, ApJ, 692, 973

Enoch, M. L., Evans, N. J., Sargent, A. I., et al. 2008, ApJ, 684, 1240

Enoch, M. L., Glenn, J., Evans, N. J., et al. 2007, ApJ, 666, 982

Enoch, M. L., Young, K. E., Glenn, J., et al. 2006, ApJ, 638, 293

Evans, N. J., Dunham, M. M., Jørgensen, J. K., et al. 2009, ApJS, 181, 321

Federrath, C., Banerjee, R., Clark, P. C., & Klessen, R. S. 2010, ApJ, 713, 269

Federrath, C., Chabrier, G., Schober, J., et al. 2011, Phys. Rev. Lett., 107, 114504

Federrath, C. & Klessen, R. S. 2012, ApJ, 761, 156

Fischer, W. J., Megeath, S. T., Stutz, A. M., et al. 2013, Astron. Nachr., 334, 53

Foster, P. N. & Chevalier, R. A. 1993, ApJ, 416, 303

Frank, A., Ray, T. P., Cabrit, S., et al. 2014, in Protostars and Planets VI, ed. H. Beuther, R. S. Klessen, C. P. Dullemond, & T. Henning (Tuscon: University of Arizona Press), 451–474

Frimann, S., Jørgensen, J. K., & Haugbølle, T. 2016a, A&A, 587, A59

Frimann, S., Jørgensen, J. K., Padoan, P., & Haugbølle, T. 2016b, A&A, 587, A60

Fromang, S., Hennebelle, P., & Teyssier, R. 2006, A&A, 457, 371

Galli, D., Lizano, S., Shu, F. H., & Allen, A. 2006, ApJ, 647, 374

Galli, D. & Shu, F. H. 1993a, ApJ, 417, 220

Galli, D. & Shu, F. H. 1993b, ApJ, 417, 243

Gong, H. & Ostriker, E. C. 2013, ApJS, 204, 8

Gray, D. F. 2008, The Observation and Analysis of Stellar Photospheres (Cambridge University Press)

Harsono, D., Jørgensen, J. K., van Dishoeck, E. F., et al. 2014, A&A, 562, 77

Hartmann, L. 2002, ApJ, 578, 914

Hartmann, L. 2008, Accretion Processes in Star Formation (Cambridge Astrophysics) (Cambridge University Press)

Hartmann, L., Calvet, N., Gullbring, E., & D'Alessio, P. 1998, ApJ, 495, 385

Harvey, D. W. A., Wilner, D. J., Myers, P. C., & Tafalla, M. 2003, ApJ, 596, 383

Herbig, G. H. 1962, Adv. Astr. Astrophys., 1, 47

Herbig, G. H. 1966, Vistas Astron., 8, 109

Herbig, G. H. 1977, ApJ, 217, 693

Herbig, G. H. 1989, in European Southern Observatory Conference and Workshop Proceedings, Vol. 33, European Southern Observatory Conference and Workshop Proceedings, ed. B. Reipurth, 233–246

Hernandez, J., Hartmann, L., Megeath, T., et al. 2007, ApJ, 662, 1067

Ho, P. T. P., Moran, J. M., & Lo, K. Y. 2004, ApJ, 616, L1

Högbom, J. A. 1974, A&AS, 15, 417

Hogerheijde, M. R. & van der Tak, F. F. S. 2000, A&A, 362, 697

Johnstone, D., Di Francesco, J., & Kirk, H. 2004, ApJ, 611, L45

Johnstone, D., Hendricks, B., Herczeg, G. J., & Bruderer, S. 2013, ApJ, 765, 133

Joos, M., Hennebelle, P., & Ciardi, A. 2012, A&A, 543, A128

Jørgensen, J. K. 2004, A&A, 424, 589

Jørgensen, J. K., Bourke, T. L., Myers, P. C., et al. 2007a, ApJ, 659, 479

Jørgensen, J. K., Bourke, T. L., Myers, P. C., et al. 2005a, ApJ, 632, 973

Jørgensen, J. K., Johnstone, D., Kirk, H., & Myers, P. C. 2007b, ApJ, 656, 293

Jørgensen, J. K., Johnstone, D., Kirk, H., et al. 2008, ApJ, 683, 822

Jørgensen, J. K., Schöier, F. L., & van Dishoeck, E. F. 2002, A&A, 389, 908

Jørgensen, J. K., Schöier, F. L., & van Dishoeck, E. F. 2005b, A&A, 435, 177

Jørgensen, J. K., van Dishoeck, E. F., Visser, R., et al. 2009, A&A, 507, 861

Jørgensen, J. K., Visser, R., Sakai, N., et al. 2013, ApJ, 779, L22

Jørgensen, J. K., Visser, R., Williams, J. P., & Bergin, E. A. 2015, A&A, 579, A23

Kenyon, S. J., Hartmann, L. W., Strom, K. M., & Strom, S. E. 1990, AJ, 99, 869

Kessler, M. F., Steinz, J. A., Anderegg, M. E., et al. 1996, A&A, 315, L27

Kim, H. J., Evans, N. J., Dunham, M. M., Lee, J.-E., & Pontoppidan, K. M. 2012, ApJ, 758, 38

Kirk, H., Johnstone, D., & Di Francesco, J. 2006, ApJ, 646, 1009

Konyves, V., André, P., Schneider, N., et al. 2013, Astron. Nachr., 334, 908

Krumholz, M. R., McKee, C. F., & Klein, R. I. 2004, ApJ, 611, 399

Kryukova, E., Megeath, S. T., Gutermuth, R. A., et al. 2012, AJ, 144, 31

Lada, C. J. 1987, in IAU Symposium, Vol. 115, Star Forming Regions, ed. M. Peimbert & J. Jugaku, 1–17

Lada, C. J. & Wilking, B. A. 1984, ApJ, 287, 610

Larson, R. B. 1969, MNRAS, 145, 271

Larson, R. B. 1981, MNRAS, 194, 809

Larson, R. B. 1985, MNRAS, 214, 379

Lee, C.-F., Hirano, N., Palau, A., et al. 2009, ApJ, 699, 1584

Lee, K. I., Dunham, M. M., Myers, P. C., et al. 2015, ApJ, 814, 114

Li, Z.-Y., Krasnopolsky, R., & Shang, H. 2013, ApJ, 774, 82

Lindberg, J. E. 2013, PhD thesis

Lindberg, J. E., Jørgensen, J. K., Brinch, C., et al. 2014, A&A, 566, 74

Lomax, O., Whitworth, A. P., Hubber, D. A., Stamatellos, D., & Walch, S. 2014, MNRAS, 439, 3039

Lommen, D. J. P., Jørgensen, J. K., van Dishoeck, E. F., & Crapsi, A. 2008, A&A, 481, 141

Looney, L. W., Mundy, L. G., & Welch, W. J. 2000, ApJ, 529, 477

Looney, L. W., Mundy, L. G., & Welch, W. J. 2003, ApJ, 592, 255

Lucy, L. B. 1999, A&A, 344, 282

Mairs, S., Johnstone, D., Offner, S. S. R., & Schnee, S. 2014, ApJ, 783, 60

Manara, C. F., Robberto, M., Da Rio, N., et al. 2012, ApJ, 755, 154

Manoj, P., Watson, D. M., Neufeld, D. A., et al. 2013, ApJ, 763, 83

Martin, R. G. & Lubow, S. H. 2011, ApJ, 740, L6

McKee, C. F. 1989, ApJ, 345, 782

Men'shchikov, A., André, P., Didelon, P., et al. 2010, A&A, 518, L103

Murillo, N. M. & Lai, S.-P. 2013, ApJ, 764, L15

Murillo, N. M., Lai, S.-P., Bruderer, S., Harsono, D., & van Dishoeck, E. F. 2013, A&A, 560, 103

Muzerolle, J., Hillenbrand, L., Calvet, N., Briceño, C., & Hartmann, L. 2003, ApJ, 592, 266

Myers, A. T., McKee, C. F., Cunningham, A. J., Klein, R. I., & Krumholz, M. R. 2013, ApJ, 766, 97

Myers, P. C. 2012, ApJ, 752, 9

Myers, P. C. & Ladd, E. F. 1993, ApJ, 413, L47

Neugebauer, G., Habing, H. J., van Duinen, R., et al. 1984, ApJ, 278, L1

Noble, J. A., Congiu, E., Dulieu, F., & Fraser, H. J. 2012, MNRAS, 421, 768

Nordlund, Å., Haugbølle, T., Küffmeier, M., Padoan, P., & Vasileiades, A. 2014, in IAU Symposium, Vol. 299, IAU Symposium, ed. M. Booth, B. C. Matthews, & J. R. Graham, 131–135

Offner, S. S. R., Klein, R. I., McKee, C. F., & Krumholz, M. R. 2009, ApJ, 703, 131

Offner, S. S. R. & McKee, C. F. 2011, ApJ, 736, 53

Ossenkopf, V. & Henning, T. 1994, A&A, 291, 943

Padoan, P., Haugbølle, T., & Nordlund, Å. 2012, ApJ, 759, L27

Padoan, P., Haugbølle, T., & Nordlund, Å. 2014, ApJ, 797, 32

Padoan, P., Juvela, M., Bally, J., & Nordlund, Å. 1998, ApJ, 504, 300

Padoan, P., Juvela, M., Goodman, A. A., & Nordlund, Å. 2001, ApJ, 553, 227

Persson, M. 2013, PhD thesis

Pilbratt, G. L., Riedinger, J. R., Passvogel, T., et al. 2010, A&A, 518, L1

Plunkett, A. L., Arce, H. G., Mardones, D., et al. 2015, Nature, 527, 70

Poteet, C. A., Pontoppidan, K. M., Megeath, S. T., et al. 2013, ApJ, 766, 117

Pringle, J. E. 1981, ARA&A, 19, 137

Robitaille, T. P., Whitney, B. A., Indebetouw, R., Wood, K., & Denzmore, P. 2006, ApJS, 167, 256

Rodgers, S. D. & Charnley, S. B. 2003, ApJ, 585, 355

Rybicki, G. B. & Lightman, A. P. 1979, Radiative processes in astrophysics (Harvard-Smithsonian Center for Astrophysics, Cambridge, Mass.: New York)

Sadavoy, S. I., Di Francesco, J., André, P., et al. 2014, ApJ, 787, L18

Safron, E. J., Fischer, W. J., Megeath, S. T., et al. 2015, ApJ, 800, L5

Sandford, S. A. & Allamandola, L. J. 1993, ApJ, 417, 815

Santos-Lima, R., de Gouveia Dal Pino, E. M., & Lazarian, A. 2012, ApJ, 747, 21

Santos-Lima, R., de Gouveia Dal Pino, E. M., & Lazarian, A. 2013, MNRAS, 429, 3371

Sault, R. J., Teuben, P. J., & Wright, M. C. H. 1995, Astronomical Data Analysis Software and Systems IV, 77, 433

Seifried, D., Banerjee, R., Pudritz, R. E., & Klessen, R. S. 2012, MNRAS, 423, L40

Seifried, D., Banerjee, R., Pudritz, R. E., & Klessen, R. S. 2013, MNRAS, 432, 3320

Shirley, Y. L., Evans, N. J., & Rawlings, J. M. C. 2002, ApJ, 575, 337

Shirley, Y. L., Huard, T. L., Pontoppidan, K. M., et al. 2011, ApJ, 728, 143

Shu, F., Najita, J., Ostriker, E., et al. 1994, ApJ, 429, 781

Shu, F. H. 1977, ApJ, 214, 488

Soderblom, D. R., Hillenbrand, L. A., Jeffries, R. D., Mamajek, E. E., & Naylor, T. 2014, in Protostars and Planets VI, ed. H. Beuther, R. S. Klessen, C. P. Dullemond, & T. Henning (Tuscon: University of Arizona Press), 219–241

Spezzi, L., Alcalá, J. M., Covino, E., et al. 2008, ApJ, 680, 1295

Stutz, A. M., Tobin, J. J., Stanke, T., et al. 2013, ApJ, 767, 36

Tassis, K. & Mouschovias, T. C. 2005, ApJ, 618, 783

Terebey, S., Shu, F. H., & Cassen, P. 1984, ApJ, 286, 529

Teyssier, R. 2002, A&A, 385, 337

Teyssier, R., Fromang, S., & Dormy, E. 2006, J. Comput. Phys., 218, 44

Tobin, J. J., Dunham, M. M., Looney, L. W., et al. 2015a, ApJ, 798, 61

Tobin, J. J., Hartmann, L., Chiang, H.-F., et al. 2012, Nature, 492, 83

Tobin, J. J., Looney, L. W., Wilner, D. J., et al. 2015b, ApJ, 805, 125

van Cittert, P. H. 1934, Physica, 1, 201

van der Tak, F. F. S., van Dishoeck, E. F., Evans, N. J., Bakker, E. J., & Blake, G. A. 1999, ApJ, 522, 991

Visser, R. & Bergin, E. A. 2012, ApJ, 754, L18

Visser, R., Bergin, E. A., & Jørgensen, J. K. 2015, A&A, 577, A102

Vorobyov, E. I., Baraffe, I., Harries, T., & Chabrier, G. 2013, A&A, 557, A35

Vorobyov, E. I. & Basu, S. 2005, ApJ, 633, L137

Walch, S., Naab, T., Whitworth, A., Burkert, A., & Gritschneder, M. 2010, MNRAS, 402, 2253

Walch, S., Whitworth, A. P., & Girichidis, P. 2012, MNRAS, 419, 760

Weingartner, J. C. & Draine, B. T. 2001, ApJ, 548, 296

Werner, M. W., Roellig, T. L., Low, F. J., et al. 2004, ApJS, 154, 1

Williams, J. P., de Geus, E. J., & Blitz, L. 1994, ApJ, 428, 693

Wyatt, M. C. 2008, ARA&A, 46, 339

Young, C. H. & Evans, N. J. 2005, ApJ, 627, 293

Yıldız, U. A., Kristensen, L. E., van Dishoeck, E. F., et al. 2013, A&A, 556, A89

Zernike, F. 1938, Physica, 5, 785

Zhu, Z., Hartmann, L., Calvet, N., et al. 2007, ApJ, 669, 483

Zhu, Z., Hartmann, L., & Gammie, C. 2009, ApJ, 694, 1045